

Федеральное государственное автономное образовательное учреждение
высшего образования «Уральский федеральный университет
имени первого Президента России Б.Н. Ельцина»

Физико-технологический институт

Кафедра экспериментальной физики

Научно-исследовательская лаборатория «Физика функциональных материалов
углеродной микро- и оптоэлектроники»

На правах рукописи

Кубиси Мохамед Сайед Ибрагим

**ОПТИЧЕСКИ АКТИВНЫЕ ДЕФЕКТЫ В СТЕКЛООБРАЗНОМ
ДИОКСИДЕ КРЕМНИЯ, ИМПЛАНТИРОВАННОМ ИОНАМИ РЕНИЯ**

1.3.8 – Физика конденсированного состояния

Диссертация на соискание ученой степени кандидата
физико-математических наук

Научный руководитель

Кандидат технических наук, доцент,

Зацепин Анатолий Федорович

Екатеринбург – 2021

Federal State Autonomous Educational Institution of Higher Education «Ural
Federal University named after the first President of Russia B.N. Yeltsin»
Institute of Physics and Technology
Department of Experimental Physics
Research laboratory «Physics of functional materials of carbon micro- and optoelectronics»

As a manuscript

Mohamed Sayed Ibrahim Koubisy

**OPTICALLY ACTIVE DEFECTS IN GLASSY SILICON DIOXIDE
IMPLANTED WITH RHENIUM IONS**

1.3.8 – Condensed matter physics

Dissertation for the degree of candidate of
physical and mathematical sciences

Supervisor

Candidate of technical sciences,
Associate professor,

Zatsepin Anatoly Fedorovich

Yekaterinburg – 2021

TABLE OF CONTENTS

Introduction	6
CHAPTER 1. POINT DEFECTS OF NOMINALLY PURE AND DOPED SILICA GLASS	13
1.1 Structure of amorphous silicon dioxide	13
1.2 Silicon dioxide application.....	15
1.3 Silicon dioxide production methods	16
1.4 Types of silica glasses.....	18
1.5 Research methods of point defects related to SiO ₂ and its main dopants	18
1.6 Point defects in pure silica	20
1.6.1 Silicon dangling bond or the E' center	21
1.6.2 Two-coordinated Si or ODC(II).....	22
1.6.3 Oxygen monovacancy or ODC(I).....	24
1.6.4 Non-Bridging Oxygen Hole Centre and Peroxy Radical.....	25
1.7 Characteristics of rhenium	29
1.8 Applications of rhenium.....	30
1.9 Energy levels and electronic transitions of point defects	31
1.10 Absorption spectroscopy	35
1.11 Luminescence spectroscopy.....	40
1.12 Transient absorption spectroscopy.....	44
1.13 Conclusions	47
CHAPTER 2. SAMPLES AND EXPERIMENTAL TECHNIQUES	48

2.1 Ion implantation	48
2.1.1 Basics of ion implantation technology.....	48
2.1.2 Advantages and general features of ion implantation technology.....	50
2.2 Ion implantation of rhenium into silica glass.....	52
2.3 Optical absorption spectroscopy	53
2.4 UV-VIS luminescence spectroscopy	54
2.5 Absorption and luminescence spectroscopy in vacuum ultraviolet.....	55
2.6 Electron paramagnetic resonance spectroscopy (EPR)	57
2.7 Conclusions	57

CHAPTER 3. OPTICAL AND LUMINESCENCE PROPERTIES OF OXYGEN-DEFICIENT CENTERS IN KUVI GLASS IMPLANTED WITH 30 KEV RE IONS..... 59

3.1 Samples characterization by methods SRIM and X-ray photoelectron spectroscopy (XPS).....	59
3.2 Optical absorption spectra of silica glass with rhenium ions	61
3.3 Photoluminescence spectra upon excitation in the near ultraviolet.....	62
3.4 Vacuum ultraviolet photoluminescence of silica glass implanted with Re ions measured at different temperatures	66
3.5 Temperature dependences of vacuum ultraviolet photoluminescence of silica glass implanted with Re ions	71
3.6 Optical absorption edge of Re ion implanted silica glass.....	76
3.6.1 Urbach rule for Re ion implanted silica glass.....	76
3.6.2 Band gap of Re ion implanted silica glass	77
3.6.3 Structural Disordering Regulations.....	80
3.7 Conclusion.....	82

CHAPTER 4. OPTICAL AND LUMINESCENCE PROPERTIES OF OXYGEN-DEFICIENT CENTERS IN KI GLASS IMPLANTED WITH 80 KEV RE IONS

.....	84
4.1 SRIM simulation for 80 keV Re ions implanted SiO ₂	84
4.2 Optical absorption of silica glass implanted with Re-ions 80 keV.....	85
4.3 Electron paramagnetic resonance (EPR) of E'-centers	90
4.4 Photoluminescence spectra upon excitation in the near ultraviolet.....	91
4.5 The decay of photoluminescence of ODC upon excitation in the near ultraviolet	95
4.6 Scheme of electronic transitions for silica glass with implanted Re ions	97
4.7 Luminescence at VUV-excitation of Re ions implanted silica glass.....	98
4.7.1 The photoluminescence Re-ODC(II) under excitation 6.97 eV ..	98
4.7.2 The photoluminescence Re-ODC(I) under excitation 7.75 eV..	100
4.7.3 The photoluminescence excitation at emission 4.1 eV	101
4.8 Conclusions	103
CHAPTER 5. OPTICAL PROPERTIES OF SILICA GLASSES IRRADIATED WITH DIFFERENT TYPES OF HEAVY IONS.....	105
5.1 Influence of the type of silica glass matrix on structural disordering during ion implantation	105
5.2. Ion-modified centers of the type oxygen monovacancy or ODC(I)....	108
5.3. Ion-modified centers of the two-coordinated silicon or ODC(II).....	111
5.4. New defect centers related with Re, Bi and Gd Ions.	114
5.5 Conclusion.....	116
CONCLUSION.....	118
LIST OF REFERENCES	120

INTRODUCTION

Relevance of the topic: The relevance of research on ion-doped oxides is determined by the logic of the development of modern condensed matter physics and the ever-growing need for the creation of new functional materials for photonics and optoelectronics.

Silicon dioxide in crystalline and glassy forms plays a fundamental role in most modern technologies [1, 2]. The most common form of crystalline SiO_2 is α -quartz, which is considered a key material for high-precision oscillators and frequency standards. Among the non-crystalline modifications of SiO_2 , an important place is occupied by optical Silica glass, various grades of which have the widest areas of practical application. Glassy SiO_2 is used, in particular, as a material for low-loss optical fibers, in transmission and integrated optics systems, in optoelectronics and nanophotonics [1, 2]. The functional properties of this material can be significantly improved, and the area of practical applications is significantly expanded through the use of special ion-beam treatment.

Ion implantation is an effective way of modifying the structure and electron-optical properties and functional materials based on SiO_2 [3, 4]. The action of an ion beam on the structure of glassy SiO_2 leads to the creation of radiation defects and impurity centers, initiates their clustering under high-dose irradiation [5, 6]. In this case, the arising structural defects and optically active centers introduce new "defect" states into the electronic energy spectrum of the initial Silica glass matrix. The nature of the alloying elements also plays an important role, making it possible to control the characteristics of the band energy structure and, accordingly, the complex of electron-optical properties of the material [7-10].

Impurity ions and point defects form complex complexes, creating new selective and non-selective optical absorption (OA) and photoluminescence (PL) bands. In turn, this leads to a change in the refractive index, the appearance of additional centers of

localization of charge carriers, and, ultimately, to a modification of the optical properties of the material [11, 12].

In this case, rhenium is a very promising alloying element for optoelectronic and photonic applications. Rhenium belongs to the transitional 5d-elements of the sixth row of the VII group with a wide range of oxidation states (+2, +3, +4, +5, +6, +7). In silicon dioxide implanted with rhenium, a wide variety of defect states can be expected due to its polyvalence, which indicates additional possibilities for controlling the properties of SiO₂.

The main problem for the practical use of rhenium as a modifying element in the technology of optical materials science and instrumentation is the limited or complete absence of the necessary data on the local structure, electronic states, and optical properties of point defects and elementary excitations in amorphous modifications of SiO₂ doped with rhenium ions. This situation is typical both for materials obtained by methods of traditional technologies, and, to the greatest extent, for Silica glasses after ion-beam exposure.

Thus, the relevance of obtaining detailed and reliable information on the properties of optically active defects in glassy silicon dioxide implanted with rhenium ions was the determining factor for the formulation of aim and tasks of this work.

The degree of development of the research topic

Currently, there are many works devoted to the peculiarities of the atomic and energy structure of SiO₂, the role of defects in the formation of electron-optical properties [7-12]. Much attention is paid to oxygen-deficient centers (Si-ODC (I), Si-ODC (II), Si-E ') [7-9], including centers formed by additives (Ge-ODC, Sn- ODC) [9, 13]. At the same time, in the overwhelming majority of studies, glass doping is carried out at the stage of glass production by introducing additives through the melt, while studies devoted to ion implantation of Silica glasses are presented to a much lesser extent.

There are a number of leading research centers in Russia and abroad that carry out spectroscopic studies of Silica glasses implanted with various ions. The influence of ions C, Si, Pb, Sn, Li, Na, K, Co [3-6, 8-12] and other elements is investigated.

However, the works devoted to the effects of accelerated Re ions on SiO₂ are very limited and belong mainly to a team of researchers from the Ural Federal University [5, 13].

The results of published fundamental and applied research on spectral-luminescence's properties of crystalline, amorphous, and glassy modifications of SiO₂ with various additives indicate a still unrealized potential for the creation of new efficient devices for the transfer and conversion of energy, laser and LED radiation sources, screens, optical sensors, sensors and solar cells. [14].

However, despite the available publications, many regularities of the influence of the local atomic structure, elemental composition, synthesis conditions, and the degree of disordering of the silicon dioxide matrix implanted with Re ions on the functional properties of the material and the mechanisms of the processes occurring in it have yet to be studied. Including the transfer of energy, as well as the relationship between the local atomic structure and the optical properties of ion-modified defect centers.

In general, the currently available information does not allow optimization of many characteristics of materials that are important in a practical sense. In this regard, there is a need for a systematic study and analysis of the energy structure, nature, and electronic-optical properties of elementary excitations in Silica glasses implanted with rhenium, with control of the defectiveness, concentration of implanted ions and the stability of their spectral-luminescence characteristics.

Therefore, this work is aimed at studying the nature and properties of optically active point defects created in glassy silicon dioxide as a result of the implantation of rhenium ions and their interaction with the matrix.

Purpose and objectives of the work:

The aim of the dissertation is to comprehensively study the optical properties of point defects in glassy silicon dioxide implanted with rhenium ions, and their spectral-luminescence parameters, which change under post-implantation effects.

To achieve the goal of the work, the following tasks were solved:

1. To analysis the literature data on silica glasses of different types and emerging in their intrinsic and extrinsic defects.
2. Perform certification of silica glass samples implanted with Re ions with energies of 30 and 80 keV using X-ray photoelectron spectroscopy and SRIM-modeling.
3. To investigate the properties of silica glasses implanted with Re ions by the method of optical spectroscopy, to establish the peculiarities of changes in the structure of glass under the influence of ion fluxes.
4. Based on experimental data (optical absorption, photoluminescence, electron paramagnetic resonance, X-ray photoelectron spectroscopy), obtain information on defects in the SiO₂ matrix that have arisen under ion-beam exposure before and after thermal annealing.
5. Comparison of the spectral-luminescence characteristics of Re-modified ODC centers and similar defects in SiO₂ glasses implanted with other heavy ions.

Scientific novelty:

1. For the first time in glassy SiO₂ implanted with Re, the values of the parameters of interband transitions, the values of the corresponding energy gaps have been determined.
2. First studied particular disordering SiO₂ glassy atomic structure upon implantation Re ions and their effect on the formation of the optical properties of the implanted samples.
3. For the first time, new modifications of oxygen-deficient optically active centers: Re-ODC (I) and Re-ODC (II) have been discovered in samples of glassy silicon dioxide implanted with rhenium ions. Data on the features of their energy structure have been obtained.
4. For the first time, a comparative analysis of the features of the spectral-luminescent characteristics of Re-modified ODC-centers and similar defects in SiO₂ glasses implanted with Bi and Gd ions has been performed.

Theoretical and practical significance of the work:

The results obtained extend the existing understanding of the physics of optical phenomena with the participation of intrinsic and modified defects of glassy SiO₂ arising under the action of ion fluxes with different energies and fluences.

The data obtained on the optical properties of Silica glass implanted with Re ions are of interest for the development of functional materials for highly integrated planar photonic structures and optoelectronic devices.

The approach to the study of kinetic, spectral-optical, and luminescence properties implemented in the course of this work can be adapted for further systematic study of structure-sensitive optical effects in silicon dioxide and its analogs implanted with ions of various types.

Thesis to defend:

1. Modification of silica glasses of various types by accelerated Re ions leads to an increase in the total structural disorder, the degree of which depends on the type of matrix, ion beam energy and manifests itself as a smearing of the band tails and a decrease in the energy gap.
2. Implantation with Re ions creates modified diamagnetic oxygen-deficient centers of the types Re-ODC (I) and Re-ODC (II) in the glassy SiO₂ matrix with altered spectral-kinetic parameters and energies of intracenter optical transitions.
3. Thermal annealing of SiO₂ samples implanted with Re ions causes the process of conversion of paramagnetic defects such as E'-centers, which leads to an additional increase in the concentration of modified diamagnetic Re-ODCs.
4. As a result of heavy ion implantation in glassy SiO₂, oxygen-deficient defects M-ODC (I) and M-ODC (II) mainly arise. The type of inserted ions (transition, rare-earth, and typical elements) predominantly determines the quantitative features of the energy structure of defects.

The degree of reliability of the work results was ensured through the use of certified samples, precise experimental equipment, modern and independent analytical

methods for processing experimental results, as well as compliance with known literature data.

Approbation of work, the main results of this work were reported and discussed at 7 International and 2 In-Russian conferences, congresses, seminar.

International: 12th International «Symposium on SiO₂, Advanced Dielectrics and Related Devices Location» (Bari, ITALY 2018), 5 th International School and Conference on «Optoelectronics, Photonics, Engineering and Nanostructures» (Saint Petersburg OPEN 2018), The VI International Young Researchers' Conference «Physics Technologies Innovation PTI 2019». (Yekaterinburg, Russia, 20-24, May 2019). VII International Youth Scientific Conference. «Physics Technology Innovation» (Yekaterinburg, Russia, 18-22, May 2020), Received certificate for the best poster in XXIII Ural International Winter School on the Physics of Semiconductors (UIWSPS-2020), Yekaterinburg -Alapayevsk, 2020, International Scientific Conference «New Materials and Solar Technologies» (Institute of Materials Science of the Academy of Sciences, Parkent Uzbekistan, May 20-21, 2021), VIII International Youth Scientific Conference «Physics. Technologies. Innovations» (Yekaterinburg, Russia, May 17-21, 2021).

In-Russian: VII Conference and School of Young Scientists and Specialists «Physical and Physicochemical Foundations of Ion Implantation (Nizhny Novgorod November 7-9, 2018), Russian Conference and School of Young «Scientists on Actual Problems of Raman Spectroscopy (Novosibirsk: May 28 - June 1 - 2018).

Personal contribution of the author, the purpose of the work was formulated by the scientific supervisor, the formulation of tasks was carried out by the supervisor with participation of the author.

The author performed a full range of spectroscopic measurements of optical absorption and photoluminescence, calculated the dynamics of relaxation processes, analyzed and interpreted the experimental results, and formulated conclusions. The author took an active part in the preparation of scientific publications and reports at conferences.

Experimental studies of luminescence and optical absorption of samples implanted with Re with an energy of 30 keV were carried out with the participation of Ph.D. D.Yu. Biryukov and Ph.D. Yu. Kuznetsova. Experimental studies by the XPS method were carried out by Ph.D. D. A. Zatsepin.

Publications, the author has published 18 papers directly related to the electron-optical properties of ion-implanted silica glasses, including 9 articles in peer-reviewed scientific journals, identified by the Higher Attestation Commission and the Attestation Council of the Ural Federal University and included in the international database Web of Science and Scopus; 9 abstracts presented at international and in-Russian conferences.

The structure and scope of the thesis. The dissertation consists of an introduction, 5 chapters, a conclusion and a list of references. The volume of the thesis is **141** pages, including **52** Figures, **15** Tables and a bibliography of **193** titles.

CHAPTER 1. POINT DEFECTS OF NOMINALLY PURE AND DOPED SILICA GLASS

1.1 Structure of amorphous silicon dioxide

The presence of defects in a crystalline or amorphous matrix may drastically modify the electrical and the optical properties of the host material. Indeed, these deformities exist in various confined electronic states that can cause optical exercises as retention and radiance with lower energies than the principal assimilation edge of the material. Regardless of whether these advances are limited at the point imperfection, the optical spectra will be impacted, to a more noteworthy or a lesser degree, by the way that they are implanted in a lattice. In a disconnected chromophore, the energy of the light quantum involved in a transition has to match exactly the difference between the electronic levels whose spread is limited only by the excited state lifetime. At change, for a chromophore inserted in a network, the vitality of the framework depends not just on the neighborhood electronic condition of the deformity, yet additionally on its coupling with the earth. Along these lines, in an optical change the moved vitality can be shared between a nearby electronic commitment and a wide assortment of phonon excitations of the vibrational methods of the framework. As a wide range of photon energies can be involved in the transition, the spectrum of absorption or luminescence consists of broad bands.

The structure of the crystalline forms of silicon dioxide, the most common being α -Silica, was extensively examined by X-ray and neutron diffraction studies. It was concluded that the basic structural unit of these crystalline solids, apart from Stishovite, is a SiO_4 tetrahedron, having at the center a silicon atom bonded to four oxygen atoms (See Figure 1.1) [1-2]. In α -Silica the bond length between silicon and oxygen can be 1.60° \AA or 1.62° \AA , each tetrahedron having two short-bonds and two long-bonds, and the O-Si-O bond angle takes the value 109.5° . Tetrahedra are connected by sharing an oxygen atom, forming an angle Si-O-Si = 144° [15]. Unlike the crystalline structures of silicon dioxide, that of amorphous SiO_2 , also called silica, is poorly understood. The most successful model in describing the

structure of silica is the Continuous Random Network (CRN), based on X– ray and neutron scattering results [16,17]

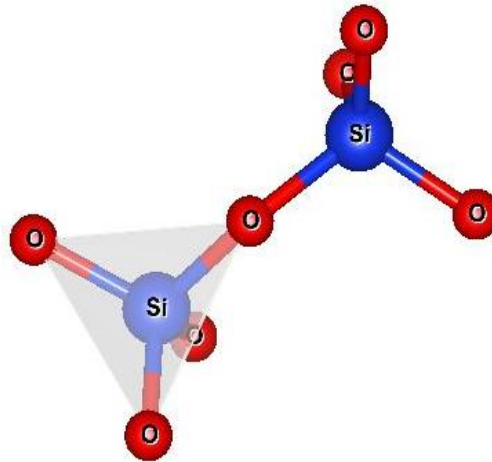


Figure 1.1 – Model structure of SiO_2 . Red and Blue circles represent oxygen and silicon atoms respectively

On the other hand, the fact that amorphous and crystalline forms of SiO_2 share the same short-range order accounts for the similarities between some of their properties. Some of the properties are listed in the Table below [18]

In fact, the characteristics made silica one of the most used materials in many fields of the modern technologies, as optoelectronics and microelectronics, as well as in the production of devices as optical fibers, photonic crystal fibers and nanowires [1, 2, 19]. Furthermore, silica is commonly used as a model system for studying the properties of amorphous materials due to its fairly basic chemical composition. For many years, these facts have attracted natural desire in a – SiO_2 . Because their existence, which is commonly connected with optical absorbance (OA) and photoluminescence (PL) activities, can undermine the material's defining features, researchers have long paid close attention to the attributes of point defects in silica.

Table 1.1 – Important Properties of silicon dioxide (SiO₂)

Properties	SiO ₂
Structure	Amorphous
Melting Point (°C)	Approximately 1600
Atomic weight (g/mol)	60.08
Density (gm/cm ³)	2.27 /2.18
Refractive index	1.46
Dielectric constant	3.9
Dielectric strength (V/cm)	10 ⁷
Infrared absorption band (μm)	9.3
Energy gap at 300 K(eV)	8.9
Linear coefficient of thermal expansion ΔL/L/ΔT (1/°C)	5×10 ⁻⁷
Thermal Conductivity at 300 K (W/cm degree K)	0.014
DC resistivity at 25 °C (Ω.cm)	10 ¹⁴ -10 ¹⁶
Young modules (N/m ²)	6.6×10 ¹⁰
Poisson's ratio	0.17

1.2 Silicon dioxide application

Following are some important applications of silicon dioxide:

1. Silica is used in the glass industry as a raw material for manufacturing glass.
2. Silica is used as a raw material for manufacturing concrete.
3. Silica is added to varnishes because of its hardness and resistance to scratch.
4. Amorphous silica is added as fillers to the rubber during the manufacturing of tires. This helps reduce the fuel consumption of the vehicle.
5. Silica is used in the production of silicon.

6. Silica is employed as a filler material in electronic circuits because it is an excellent insulator.

7. Silica is employed in transducers because of its piezoelectric characteristics.

8. It is used as a desiccant because of its propensity to absorb moisture.

Silicon Dioxide is used in semiconductor fabrication especially for metal-oxide-semiconductor (MOS) technology. In comparison to other materials that have one or more flaws, SiO_2 has a number of desirable qualities and benefits. The following are some of SiO_2 's significant functions:

1. Mask against implantation or diffusion of dopant into Silicon
2. Passivation of the surface
3. Isolation of the device
4. Component in MOS architectures (gate oxides)
5. Electrical isolation of multi-level metallization systems
6. Thermal conductivity is high.
7. No Cu or other ions diffuse into the dielectric
8. There is no leakage between the conductors.

1.3 Silicon dioxide production methods

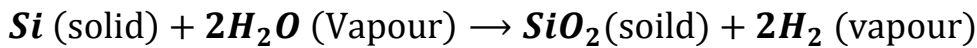
Temperature is the central ambient parameter used during silicon oxidation to monitor oxide growth. However, in the reaction chamber, it is also possible to adjust the hydrostatic pressure. The crystal orientation of the silicon wafer also has a role, whether the oxidation state is wet (H_2O) or dry (O_2) also plays a role in deciding the growth rate.

Dry oxidation is a technique of oxidation in which oxygen is utilized as the oxidant. When compared to wet oxidation, dry oxidation produces a more homogeneous and denser thermal oxide with even higher dielectric strength. The pace of growth is the most significant variation between wet and dry oxide growth. Wet oxide grows significantly more slowly than dry oxide. As a result, dry oxides have a maximum thickness of 1000 nm and are mostly utilized for thin gate and capacitor oxides that require great uniformity and dielectric strength.

The chemical reaction at consideration is as follows:



Wet Oxide method, the silicon wafer is put into the water vapor (H_2O) atmosphere during wet oxidation and the water vapor molecules react with the solid silicon atoms (Si) on the wafer's surface, resulting in a chemical reaction, with the release of hydrogen gas (H_2) as a by-product.



It is evident that wet oxidation operates at much higher oxidation rates, up to around 600 nm/h, than dry oxidation. The explanation is the ability of hydroxide (OH^-) to disperse much faster than O_2 through the already-grown oxide, effectively expanding the bottleneck rate of oxidation while growing thick oxides, which is the diffusion of species. Wet oxidation is commonly used where thick oxides are required, such as insulation and passivation layers, masking layers, and for blanket field oxides, because of the quick growth rate [20-22].

Pictures in the Figure 1.2 are the non-heat-treated sample, the dry sample, and the wet sample, respectively. The untreated sample's surface looked like frosted glass. The difference in the flattening of a dry and wet sample can be clearly seen after heat treatment at 1200 C for 48 h. In the dry sample, surface scattering undoubtedly decreased; however, the wet sample realized increased flattening as well as better surface luster [22].

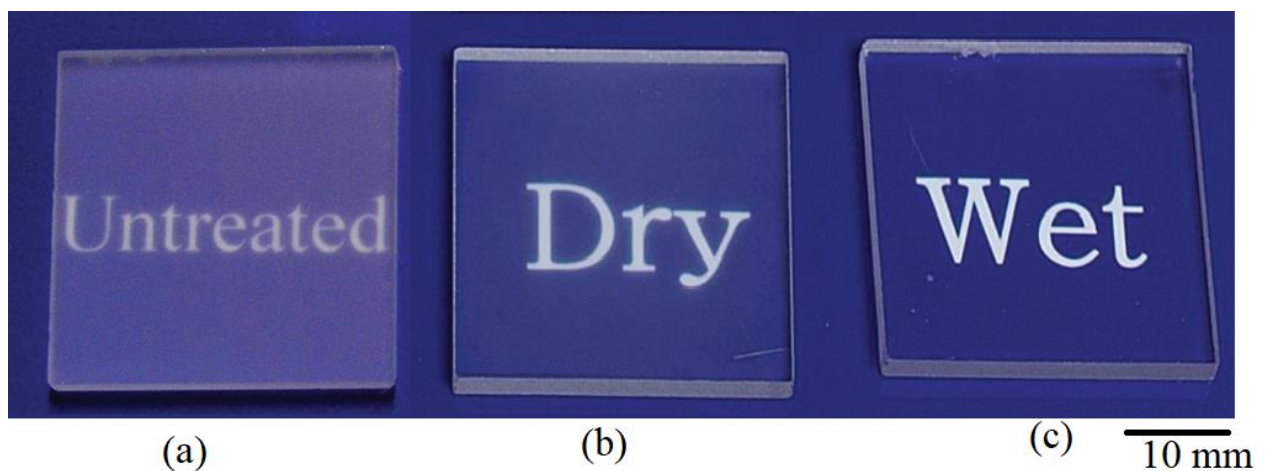


Figure 1.2 – Photographs of samples with sizes of $20 \times 20 \times 1 \text{ mm}^3$:

(a) untreated and after heat treatment for 48 h in (b) dry air and (c) wet air [22]

1.4 Types of silica glasses

With the increasing requirements and changing the parameters of silica glass properties over the past two decades an increasing effort has been made in the silica melt process. This growth is not over yet, but it is still advancing strongly in terms of properties and structure, and we have to differentiate between the different types of silica glass so far, there are about four types available commercially [23-25].

Type I (GE-105-USA), KI (Russia), Silica glasses are made by electrical fusion under a vacuum or an inert atmosphere from natural Silica. They contain almost no OH groups (about 5 ppm or less) but relatively high molecular impurities of 30-100 ppm Al and 4 ppm Na, respectively (all in weight fractions) [23-25].

Type II, GE-102(USA), KV (Russia), silica glasses are made from Silica crystal powder by flame fusion (Verneuille-process). The metallic impurities are less than in Type I silica glasses due to partial volatilization and the absence of any crucible material, but the atmosphere of the hydrogen-oxygen flame creates an OH content of about 150-400ppm. the optical transparency in the ultraviolet range silica glass produced by thermal treatment in oxygen atmosphere [23-25].

Type III, Corning 7940 (USA), KU (Russia), Silica glasses are synthetic vitreous silica formed when sprayed into an oxygen-hydrogen flame by SiCl_4 hydrolyzation. This substance is virtually free of metallic impurities, but contains a large quantity of OH in the order of 1000 ppm and a quantity in the order of 100 ppm of the starting material Cl. [23-25].

Type IV, Corning 7943(USA), KUVI (Russia), silica glasses are also synthetic vitreous silicas produced from SiCl_4 in a water vapour-free plasma flame. These silica glasses are similar to type III but contain only about 0.4 ppm OH and about 200 ppm Cl. [23-25].

1.5 Research methods of point defects related to SiO_2 and its main dopants

To generate the transition between trial-and a phenomenological and error-based development model and a guided rational design of solar cell and specialty fibers, a

deep knowledge on the atomic structure and related spectroscopic signature of point defects is a basic requirement. In addition, clear maps of their formation and conversion mechanisms have to be drawn. Experimentally, it is desirable to have access to preforms and solar cell that are manufactured ad hoc to have a sufficient knowledge and control on their chemical composition and manufacturing conditions. The main and standard characterization techniques comprise EPR, optical absorption (IR, visible and UV) and luminescence. In special cases, also Raman might provide with some insights [26-28] In order to identify centers together with their corresponding generation and conversion mechanisms, it is necessary to monitor, analyze and compare the behaviors of several fiber samples when exposed to different radiation sources (photons, electrons, protons, neutrons...) and doses at different conditions as, for example, temperature, or pressure.

Correlating some of the spectroscopic signatures and behavior to given center structures is, therefore, an expensive, formidable and cumbersome task which does not guarantee the construction of a meaningful model for the underlying atomic-scale mechanisms. In this context, atomic scale theoretical modeling might be a very useful complementary tool. Theoretically, electronic and optical properties of defects were historically (and sometimes still) addressed within the framework of Density Functional Theory (time dependent or not), (TD)-DFT, or Hartree-Fock and Configuration Interaction in very small cluster models or molecular analogs [29-31] or in bulks [32-37] After the precursory work of E. Chang et al.[38] that demonstrated the accuracy of solving the Bethe-Salpeter Equation (BSE) within the GW approximation for modeling optical properties, the combination of both has become a standard in the field, that has allowed for univocal assignments between measured experimental optical bands and atomic structure [38]. Indeed, the BSE accounts, in a computationally efficient way, for screening and electron-hole interactions from first-principles. The development of the GIPAW [39,40] formalism based on DFT has represented also a revolution in the field that has opened the way for a parameter-free calculation of the EPR parameters as Fermi contacts and g-tensors. The GIPAW

has successfully been applied to relate measured EPR parameters with the underlying atomic structure [41- 43]. Figure1.3 describes at a glance the standards in modeling and spectroscopic characterization tools.

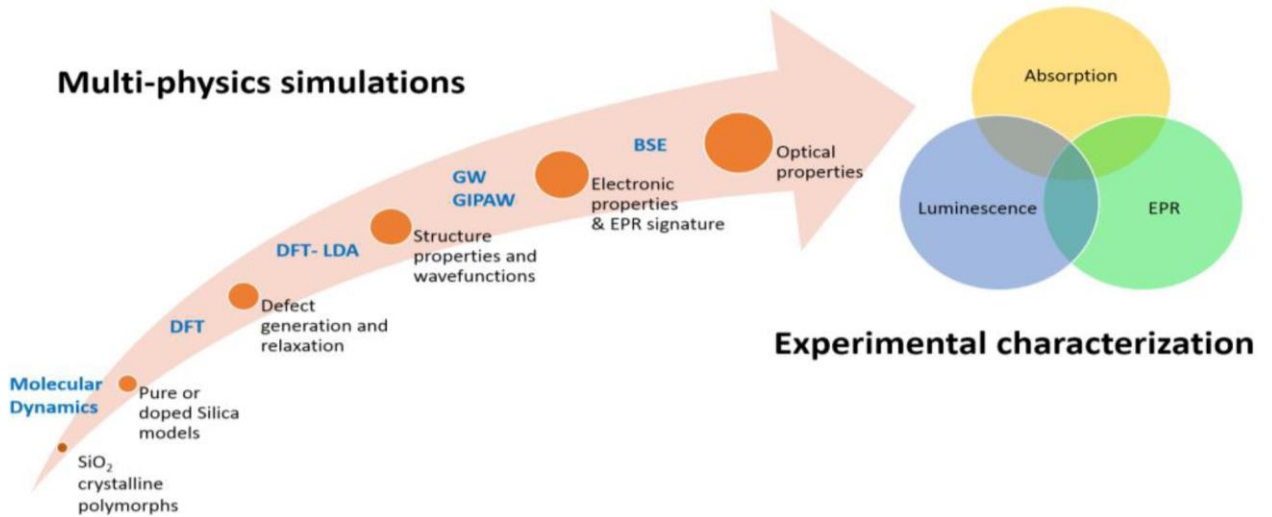


Figure1.3 – Illustration of the coupled experimental /simulation approach used to identify the structural and optical properties of radiation-induced point defects in silica. More details can be found in [44-46]

1.6 Point defects in pure silica

There are various articles today concerning the optical and spectroscopic properties of different silica defects [47-50]. First, only intrinsic defects that are commonly found in silica glass are considered.

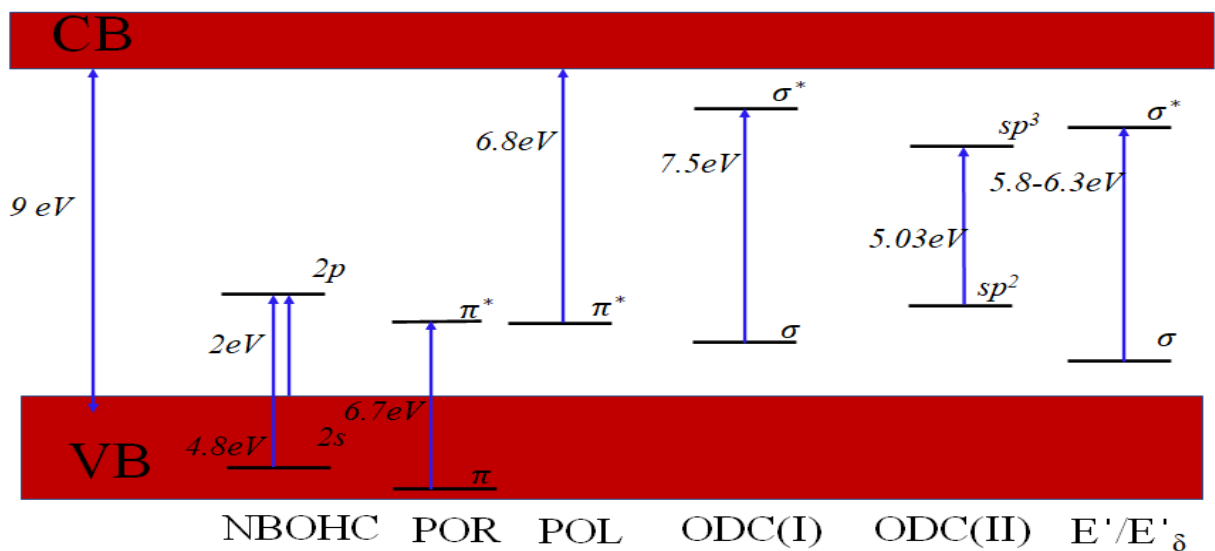
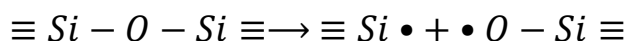


Figure 1.4 – Electronic states structure of intrinsic silica defects from Refs [51,52]

We will be dealing with relatively long-lived defects, so they can be identified even at room temperatures for a long time after the injury. Figure 1.4 summarizes their structures, electronic properties, optical absorption, and photoluminescence bands. The properties of intrinsic and extrinsic ODC's have been treated in a large number of experimental and theoretical works which evidenced some aspects concerning their optical (OA and PL bands) and magnetic (EPR structures) activities.

1.6.1 Silicon dangling bond or the E' center

The EPR signal of the E' center was first detected in neutron irradiated α -Silica by **Weeks** in 1956 [53]. The author attributed the observed EPR structure to a paramagnetic defect consisting in an electron trapped in an oxygen vacancy. **Silsbee** [54] observed an EPR doublet around the central resonance line of E' center on the basis of these observations, **Feigl, Fowler and Yip** [55] proposed the currently accepted theory for the basic structure of E' center in α -Silica. In their model, the E' center originates by an asymmetric relaxation of a positively charged oxygen vacancy, with the spin localized in a nonbonding sp^3 hybrid orbital on one Si atom and the opposite Si^+ ion relaxed in the plane of its three ligand oxygens. It can be presented as a Si dangling bond with a trapped electron generated in following reaction.



The name E' centres describes a class of radiation induced paramagnetic point defects, always present in irradiated silica. These different centres share the fundamental structural property of having an unpaired electron localized in a sp^3 hybrid orbital of a threefold coordinated silicon (See Figure 1.5)

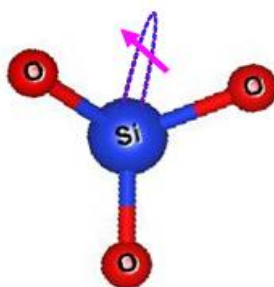


Figure 1.5 – Model of E'- center in SiO_2

The "E'– center" EPR signal [56,57] in glass is strongly related to the high absorption band at 5.8 eV (see refs. in [58]), which is clearly related to the "dangling bond" section of the center. Other forms of E'– centers have less precise optical absorption capabilities, although the peaks can be expected to be in the 5–6 eV region.

Until now, several papers have evidenced that an absorption band centered at ~5.8 eV and with a FWHM of ~0.8 eV is characteristic of irradiated silica. A linear correlation between the ESR signal of the E' centers and this OA band was originally found in 1963. For instance, **Guzzi et al.** [59] found in neutron irradiated samples that the growth of the intensity of 5.8 eV OA does not agree with that of the ESR signal of E' center. **Nishikawa et al** [60] measured a 5.8 eV OA in unirradiated sample containing no ESR detectable E' center. Those authors suggested that OA bands of different origin with respect to the E' center could exist in this spectral region. Another unclear aspect is the nature of the electronic transition at 5.8 eV.

1.6.2 Two-coordinated Si or ODC(II)

An OA band located in the UV range at ~5.0– 5.2 eV was originally observed both in neutron irradiated and in as grown natural silica by **Cohen** in 1957 [61]. Moreover, several luminescence bands were found by exciting in this spectral region. In particular, three emissions centered at ~4.2– 4.4 eV, ~3.1 eV and ~2.7 eV were easily detected both in as grown and in irradiated silica and were named α , β and γ bands, respectively [62].

At first, the OA band ODC(II) was tentatively and generically ascribed to an ODC in the silica network either intrinsic (neutron irradiation– induced) or extrinsic (impurity– related) [61, 63].

In 1973, **Arnold** [64] found that the intensity of the B2 band was enhanced in H⁺ ion– implanted pure silica. On the basis of that observation, the author attributed this OA band to an intrinsic oxygen vacancy produced by knock– on processes where the oxygen atom is displaced by the H⁺ ions. This assignment was supported by **Imai et al.** [65] who observed the decrease of both the OA at 5.0 eV and the PL at 4.3 eV

and the simultaneous increase of the ESR signal of E' center upon ArF laser irradiation ($h\nu=6.4$ eV). Those authors assigned these OA and PL bands to a neutral unreaxed oxygen vacancy indicated by $O\equiv Si-Si\equiv O$. This differs from the structure shown in fig. 1.6 (relaxed vacancy) because a Si atom is localized in the opposite side with respect to the plane of its three-ligand oxygen

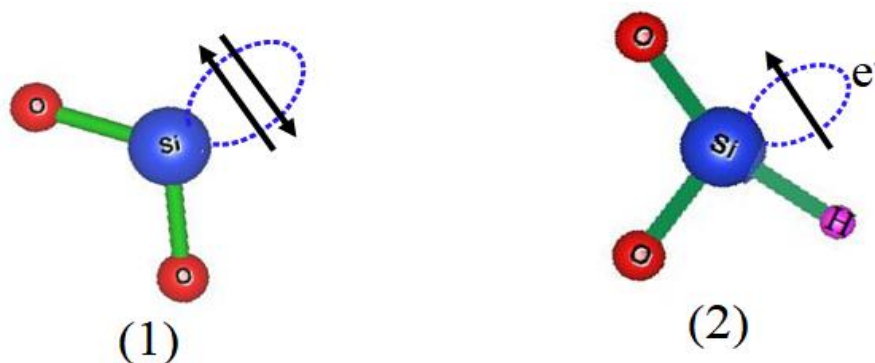


Figure 1.6 – Model structures of (1) the ODC(II) and (2) the H(I) centres. Red, Blue and Magenta circles represent oxygen, silicon and hydrogen atoms respectively [65].

Alternatively, Skuja *et al.* [51] proposed that the ODC(II) band centered at 5.03 eV originate from a twofold coordinated Si whose model is shown in Figure 1.6. (2). Moreover, they associated the two PL emissions at 4.3 eV and 2.7 eV to singlet–singlet and triplet–singlet transitions occurring in the same defect.

The spectral features of the ODC(II) band were better identified by observations that two different OA were accidentally overlapping at ~ 5 eV and two different emissions contributed to the PL band α at ~ 4.2 – 4.4 eV [66,67].

The distinction proposed by **Tohmon et al** [67] concerning the two activities A and B was successively questioned and debated in a large number of works. In 1990, **Pio et al.** [68] criticized the assignment of both the 4.4 eV and 2.7 eV emissions to a single– center (A– type) and the 4.2 eV and 3.1 eV emissions to a single– center (B– type), on the basis of differences detected in the excitation spectra of these PL bands. Successively, **Anedda et al.** [69] observed that the PL at 4.4 eV was enhanced by neutron irradiation, whereas the PL at 4.2 eV was destroyed. Those authors proposed that the emission at 4.4 eV comes from an intrinsic defect and named it α_1 band (I

stand for intrinsic). Moreover, they suggested that the PL at 4.2 eV probably originates from the same defect as is responsible for α_i , but perturbed by an unidentified impurity. The PL at 4.2 eV was called α_E (E stands for extrinsic).

1.6.3 Oxygen monovacancy or ODC(I)

This is a neutral vacancy for oxygen, with the formula ($\equiv\text{Si}-\text{Si}\equiv$). The EPR technique cannot be applied to them since they are diamagnetic centers, and most knowledge comes from optical studies.

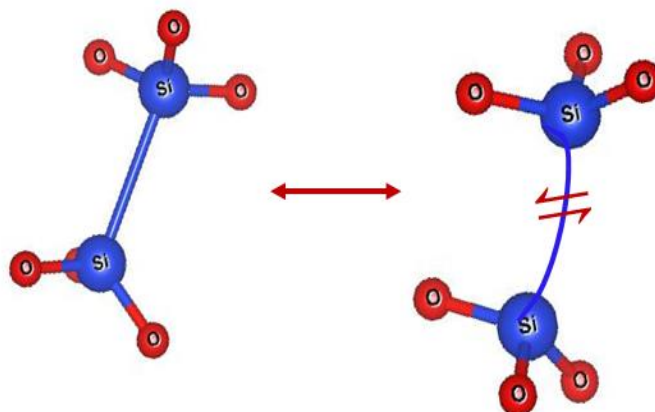


Figure 1.7 – Neutral oxygen vacancy or ODC(I) defects observed in SiO_2

An OA band centered at ~ 7.6 eV was originally observed in neutron irradiated SiO_2 in 1957 by **Mitchell and Paige** [70] seen Figure 1.7. This band was named by those authors "E– band" and tentatively assigned to an interstitial oxygen. Later, in 1979, a correlation of this OA with the peroxy radical ESR signal was observed in irradiated O_2 – containing glasses by **Friebele et al.** [71].

However, that correlation was not consistent with other reports [64,66] showing that an OA band at 7.6 eV could be observed also in silica samples where no ESR signal was detected, so indicating that the center responsible for the E band is diamagnetic. In 1983 **O'Reilly and Robertson** [72], by theoretical calculations on defect energy levels, reported that the OA at 7.6 eV was associated to the transition from the ground to the first excited state occurring in a neutral oxygen vacancy $\text{Si}-\text{Si}$. This assignment was successively supported by other authors. **Imai et al.** [65], on the basis of the similarity between the OA at 7.6 eV observed in synthetic silica and the

absorption peak in Si_2H_6 molecules [73]. **Tohmon et al.** [67], by **ab initio** calculations, showed that the 7.6 eV band was caused by a singlet–singlet transition occurring in an oxygen vacancy.

Besides the relaxed oxygen vacancy, alternative models have been also suggested as defect responsible for the OA band at 7.6 eV. **Rupta** [74] proposed a silicon vacancy, **Trukhin et al.** [75] a complex defect consisting of a twofold coordinated Si and a mobile impurity as H or Cl atom and **Khalilov et al.** [76] a positively charged three–fold coordinated silicon. Moreover, it has been evidenced that the emissions associated to the OA band B_2 can be also excited in the vacuum–UV region [69,77,78]. **Skuja** [78] reported that the emissions at 2.7 eV and 4.4 eV and at 3.1 eV and 4.2 eV are excited at 7.0 eV and 6.8 eV, respectively. In particular, the two excitation energies 7.0 eV and 6.8 eV were associated to the transitions occurring from the ground state S_0 to the second excited state S_2 in a twofold coordinated Si and Ge, respectively. Therefore, these transitions were not correlated with the OA band E at 7.6 eV. **Trukhin et al.** [75] observed the two emissions at 2.7 and 4.4 eV upon excitation at 7.6 eV and attributed this optical activity to a complex defect as above mentioned. **Anedda et al.** [64] showed that the PLE spectra of the PL emissions at 4.2 eV and 4.4 eV are both peaked at 7.6 eV as the OA band E, but no excitation mechanism under vacuum–UV light was hypothesized by those authors. Finally, **Nishikawa et al.** [79] reported that an emission at 4.4 eV is excited in vacuum–UV at two different energies, 6.9 eV and 7.6 eV. They proposed that this PL band originates from an ODC existing in two configurations, probably a relaxed and an unrelaxed oxygen vacancy as hypothesized in ref. [65]. So, to explain the emission at 4.4 eV excited within the E band, they suggested that a conversion of this ODC from one configuration to the other is effective upon excitation at 7.6 eV

1.6.4 Non-Bridging Oxygen Hole Centre and Peroxy Radical

Non-Bridging Oxygen Hole Centres (NBOHC) and Peroxy Radicals (POR) are, together with the E' centres, among the main radiation induced paramagnetic point

defects in silica. As well as the E' centre, they belong to the class of the dangling bonds defects [80].

NBOHC was established to be an oxygen dangling bond, and the peroxy radical a dangling bond on a peroxy group (See Figure 1.8).

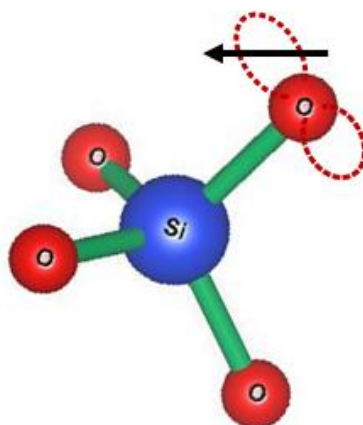


Figure 1.8 – Model structures of Non-Bridging Oxygen Hole Centre (NBOHC).

Red and Blue circles represent oxygen and silicon atoms respectively.

The NBOHC give important contributions to the OA of irradiated silica in the visible and ultraviolet spectral ranges. In fact, they are responsible for OA bands at 2.0 eV, 4.8 eV and 6.8eV [81, 82]. The assignment of the strong (oscillator strength $f = 0.2$) absorption band at 4.8eV to NBOHC was controversial for a long time, due to its overlap with a nearly identical 4.8 eV OA of interstitial ozone molecule [83], and also because a part of NBOHC is *EPR silent* [84, 85]. A PL band at 1.9eV can be excited inside these absorption bands [86, 87].

The spectral characterization of POR in bulk silica is instead more controversial (Figure1.9). Their OA band on silica surfaces is found at ~ 5.4 eV, with FWHM ~ 1.2 eV and oscillator strength $f \sim 0.06$ [88]. The spectral parameters of this band are very close to those of surface NBOHC (peak position ~ 4.9 eV, FWHM ~ 1.2 eV and $f \sim 0.05$). This fact, together with the existence of interconversion processes between these two defects, made the identification of the spectral features

of POR difficult. An OA band at 5.3eV with FWHM '1.3eV and f '0.05 is nowadays attributed to POR [68].

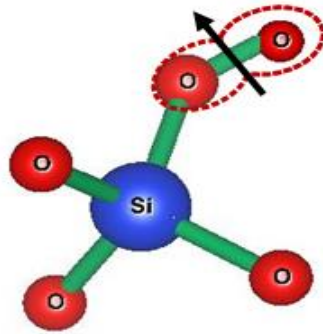
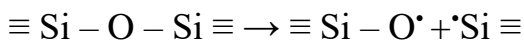
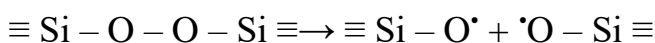


Figure 1.9 – Model structures of Peroxy Radical (POR). Red and Blue circles represent oxygen and silicon atoms respectively.

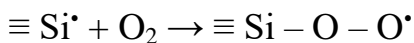
Differently from other ordinary defects in silica, as the E' centre, NBOHC and POR have not analogous in α -Silica. This is probably due to the lack of appropriate sites for these defects in the ordered structure of α -Silica. Several generation mechanisms have been proposed for both these defects, involving different precursors. NBOHC can be created by breaking strained Si–O bonds [89, 90]



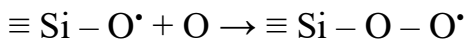
The peroxy linkage $\equiv \text{Si} - \text{O} - \text{O} - \text{Si} \equiv$ (POL) can be a precursor for NBOHC too.



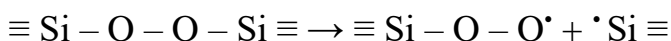
POR can be created by reaction of interstitial oxygen molecules with an E' centre [91]



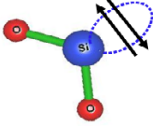
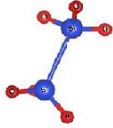

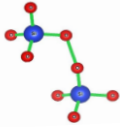
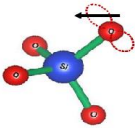
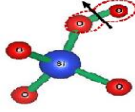
or through the reaction of atomic oxygen with a NBOHC [92]



They can also be generated through the breakage of a Si–O bond in a POL, with the simultaneous formation of an E' centre [93]



Toable1.2: Characteristics of point defects in silica

defect name(s)	Suggested structural model(s)	Peak positions of the optical absorption, PLE (eV)	FWHM (EV)	Peaks of PL bands (eV)	Oscillator strength f	PL decay constant (ms)	Refs
ODC(II)		6.8-7 4.95-5.05 3.15(ev)	0.4 0.3 0.32	4.4, 2.7 4.3-4.4,3.1 2.75-2.8	0.1-0.2 0.15 1.60×10^{-7}	4.nm,10.2ms 10.2ms	[72,79,] [94]
ODC(I)		7.6	0.62 0.5	4.4, 2.7-	0.1-0.2	4.1 2.1nm	[65,72,79,]
E' CENTER		5.7-5.8	0.8	-	0.1-0.2	Not observed	[57,58]
Peroxy Linkage (Pol)		1.3		-	1.3		[65]
Non-Bridging Oxygen Hole Centres (NBOHC)		4.8 2	1.05 0.18	1.85-1.95	0.2 4×10^{-4}	10-20 us	[81,82]
Peroxy Radical (POR)		1.97 4.8	0.175 0.8	-	5.7×10^{-4}	-	[86,87]

1.7 Characteristics of rhenium

The chemical element rhenium has the symbol Re and the atomic number 75. It's a heavy, silvery-gray sixth-row transition metal in the periodic table's group 7. Rhenium is a rare element found in the Earth's crust. At 5903 K [95], rhenium has the third highest melting point and the second highest boiling point of any stable element. Rhenium is a chemically similar metal to manganese and technetium, and it is mostly derived as a by-product of the extraction and refinement of molybdenum and copper ores. Rhenium has a wide range of oxidation states in its compounds, ranging from -1 to +7.

Rhenium has a high resistance to poisoning induced by sulfuric and hydrochloric acids as well as corrosion by hydrogen, nitrogen, sulfur, and phosphorus. Re coatings are applied in high-temperature rocket engines to reduce wear and arc erosion [96]

Only tungsten and carbon have higher melting points than rhenium, a silvery-white metal with one of the highest melting values of all elements. It also has one of the highest boiling points among stable elements, and one of the highest among all elements. It is also one of the densest metals, with only platinum, iridium, and osmium surpassing it. With lattice parameters of $a = 276.1$ pm and $c = 445.6$ pm, rhenium has a hexagonal close-packed crystal structure [97].

The most prevalent oxide is Re_2O_7 , which is a volatile yellow oxide. The perovskite-like structure of red rhenium trioxide ReO_3 , Re_2O_5 , ReO_2 , and Re_2O_3 are some of the other oxides. ReS_2 and Re_2S_7 are the sulfides. The action of ammonium hydrosulfide can convert perrhenate ions to tetrathioperrhenate.

1.8 Applications of rhenium

Rhenium is added to high-temperature superalloys used in jet engine parts, accounting for 70% of global rhenium output. Platinum–rhenium catalysts, which are principally utilized in the production of lead-free, high-octane gasoline, are another key application. [98]

Alloys

The inclusion of rhenium to nickel-based superalloys improved creep strength. Rhenium is usually found in alloys at a concentration of 3% to 6%. Second-generation alloys have a 3 percent rhenium content and were used in the engines of the F-15 and F-16, but the newer single-crystal third-generation alloys have a 6 percent rhenium content and were used in the engines of the F-15 and F-16. Rhenium can promote microstructural instability in superalloys, resulting in undesirable topologically tight packed (TCP) phases. To avoid this effect, ruthenium is employed in 4th and 5th generation superalloys. Tungsten's characteristics are improved by rhenium. At low temperatures, tungsten-rhenium alloys become more ductile, making them easier to process. The stability at high temperatures has also been increased. Because the effect rises with increasing rhenium concentration, tungsten alloys can contain up to 27% Re, which is the solubility limit. Tungsten-rhenium wire was first developed in an attempt to make a more ductile wire after recrystallization. This enables the wire to achieve specified performance goals, such as improved vibration resistance, ductility, and resistivity. X-ray sources are one application for tungsten-rhenium alloys. Both elements' high melting points, along with their high atomic masses, render them stable in the face of prolonged electron impact. Thermocouples made of rhenium tungsten alloys can measure temperatures up to 2200 degrees Celsius.

Rhenium is useful in self-cleaning electrical contacts because of its high temperature stability, low vapor pressure, superior wear resistance, and ability to survive arc corrosion. The discharge that happens during electrical switching, in particular, oxidizes

the contacts. However, because rhenium oxide Re_2O_7 is unstable (it sublimates at 360°C), it is eliminated during the discharge. Rhenium, like tantalum and tungsten, has a high melting point and low vapor pressure. As a result, rhenium filaments are more stable when operated in an oxygen-containing atmosphere rather than in vacuum. These filaments are commonly found in mass spectrometers, ion gauges, and photography photoflash lamps.

Catalysts

Catalytic reformation is a chemical process that converts low-octane petroleum refinery naphthas into high-octane liquid products. Rhenium, in the form of rhenium-platinum alloy, is employed as a catalyst. Rhenium is found in 30% of the catalysts used in this process all over the world [99]. The other reaction in which rhenium is used as a catalyst is the olefin metathesis. This procedure is usually carried out with Re_2O_7 on alumina. [100] Rhenium catalysts are utilized in certain types of hydrogenation reactions because they are resistant to chemical poisoning from nitrogen, sulfur, and phosphorus [101].

1.9 Energy levels and electronic transitions of point defects

Because a point defect interacts strongly with the matrix via covalent interactions and does not exist as a separate entity, it cannot be investigated in isolation. The system's electronic structure is actually highly influenced by its vibrational modes (*electron-phonon coupling*), and it is more appropriate to speak in terms of the defect-matrix complex and its optical features in this regard. A cluster of the matrix with a single flaw is treated as a molecular system in the theoretical method. This strategy is commonly used in all computational studies where a focus is placed on determining the correct cluster size. [102].

The calculation of eigenfunctions and the treatment of optical properties identified with an atomic framework is a many-body issue thus it can't be actually completed. For this purpose, the *Born-Oppenheimer or adiabatic approximation* [103,104] is commonly used, which assumes that the total eigenfunctions $\Psi(\mathbf{r}, \mathbf{R})$ of a molecular

system can be factorized into two terms: an electronic wave function $\chi(\mathbf{r}, \mathbf{R})$, which depends on both nuclear, \mathbf{R} , and electronic, \mathbf{r} , coordinates, and a wave function $\phi(\mathbf{R})$ associated with the nuclei and only their coordinates:

$$\Psi(\mathbf{r}, \mathbf{R}) = \chi(\mathbf{r}, \mathbf{R})\phi(\mathbf{R}) \quad (1 - 1)$$

It is worth to take note of that the electronic wave work $\chi(\mathbf{r}, \mathbf{R})$ contains likewise the electronic turn factors \mathbf{s} and must be antisymmetric as for the electronic direction's changes. Since in the accompanying of this area we won't manage the turn factors, we don't expressly show the turn states. In concurrence with the adiabatic guess, $\chi(\mathbf{r}, \mathbf{R})$ can be thought as the eigenfunction of the electronic subsystem with the cores fixed at the positions \mathbf{R} .

In the case of minor nuclear motions and assuming the system is in a stable configuration (harmonic approximation), we can express the cartesian directions \mathbf{R} as far as the ordinary vibrational modes \mathbf{Q} of the deformity grid complex and factorize the atomic wave work as a result of N single consonant oscillator eigenfunctions $\varphi_i(Q_i)$, portrayed by the harmony position Q_{0i} and vibrational vitality $E_i = h\nu_i$

$$\varphi(Q) = \prod_{i=1}^N \varphi_i(Q_i) \quad (1 - 2)$$

In this framework, the energy eigenvalue associated with a $\Psi(\mathbf{r}, \mathbf{R})$ is

$$E = E_0 + \sum_{i=1}^N E_i(0.5 + m_i) \quad m_i = 0, 1, 2, \dots \quad (1 - 3)$$

where E_0 is the energy of the system considering all the nuclei fixed in the equilibrium position, N is the number of the normal modes, and m_i is the occupation number of the i -th mode Q_i , respectively.

In the zero-th request estimate, the fundamental commitment to a radiative transition rises from the electric dipole minute between the included states, which are normally the ground electronic state g and the principal energized electronic state $u^{(1)}$. In the accompanying, we will show the two states with $\Psi_g(\mathbf{r}, \mathbf{Q}) = \chi_g(\mathbf{r}, \mathbf{Q})\varphi_u(\mathbf{Q})$ and $\Psi_u(\mathbf{r}, \mathbf{Q}) = \chi_u(\mathbf{r}, \mathbf{Q})\varphi_u(\mathbf{Q})$, separately, while the relating vitality eigenvalues are

$$E_g = E_{0g} + \sum_{i=1}^N E_{ig}(0.5 + n_i) \quad n_i = 0,1,2, \dots \quad (1-4)$$

$$E_u = E_{0u} + \sum_{i=1}^N E_{iu}(0.5 + m_i) \quad m_i = 0,1,2, \dots \quad (1-5)$$

A helpful method to envision the energy levels plan related with the conditions (4) and (5), and Figure 1.10. (1) shows the configurational outline of the linked optical improvements. The defect-matrix complex's energy in the ground and excited electronic states is reported as a function of nuclear displacements, which are represented by a single generalized normal coordinate, Q_i . Moreover, in concurrence with the consonant estimate, we created parabolic wells for both the ground and excited states. When a photon absorbs in the system, it excites it to the upper state, a few configurational unwinding happens, changing the harmony position and diminishing the aggregate electronic vitality. To demonstrate this method, the lower and upper wells in Figure 1.10 (1) have been shifted and centered at different equilibrium positions (Δ_i represents their relative shift), with dashed arrows pointing toward the new equilibrium position. Even if a system's relaxation entails a shift in the normal mode set, this impact is typically irrelevant and it is for the most part right to expect the same vibrational frequencies in the two states, for example $E_{ig}=E_{iu}$ (linear coupling approximation). Besides, Because the electronic wave work $\chi(\mathbf{r}, \mathbf{Q})$ is merely a weak function of the nuclear coordinates [103]. It is commonly right to assume, in zero-th request estimation, that it depends just on the harmony positions Q_0 of the cores in the related electronic state (Condon approximation).

Because an electronic transition takes 10^{-15} seconds and typical nuclear dynamics take $\sim 10^{-12}$ seconds, and because the electronic subsystem is much lighter than the nuclear subsystem, it is reasonable to assume that: I the nuclei do not move during the electronic transition (solid arrows in Figure 1.10 (1) must be vertical), and (2) no changes in their momenta must be considered (i.e. the slowest subsystem does not react).

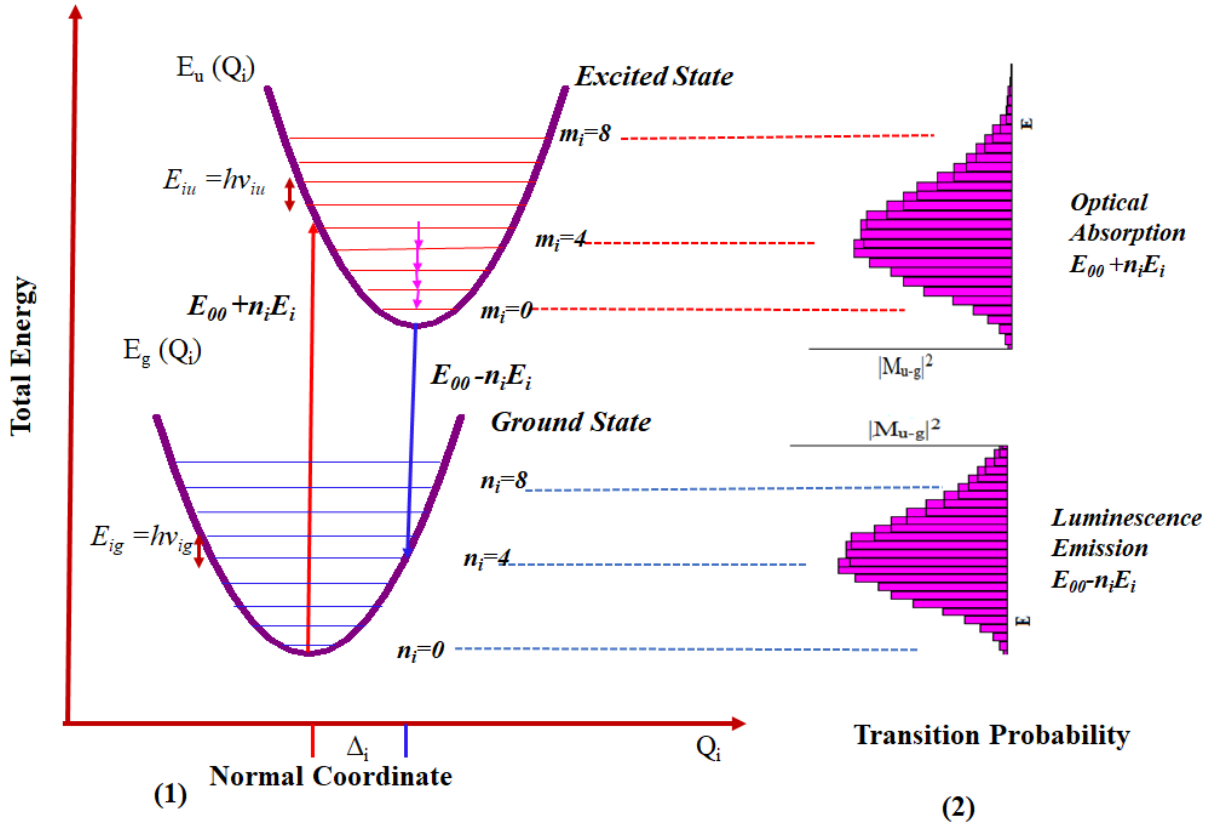


Figure 1.10 – (1) Configurational diagram of the possible energies of the ground (g) In harmonic approximation, and excited (u) states as a function of a generalized normal mode. (2) Energy dependency of the probabilities of change for absorption and emission. See text for details (Figure from [105]).

The simplest version of the Franck-Condon Principle is the assuming of both conditions, and in this context, the electric dipole matrix element $M_{g \rightarrow u}$ for 1 transition from the ground to the excited state is:

$$M_{g \rightarrow u} = M_e \int \varphi_{u\{m_i\}}^*(Q) \varphi_{g\{n_i\}}(Q) d\tau_N \quad (1-6)$$

where, accordingly to the Condon approximation,

$$M_e = e\vec{\varepsilon} \cdot \int \chi_u^*(r, Q_{0u}) \left(\sum_{i=1}^n \vec{r}_i \right) \chi_g(r, Q_{0g}) d\tau_e, \quad (1-7)$$

$\{n_i\}$ and $\{m_i\}$ are the occupation numbers of the ground vibrational excited and levels, respectively, e is the electron charge, $\vec{\varepsilon}$ is the electromagnetic field polarization vector and n is the number of electrons; The nuclear and electronic variables are

used to determine the integrals in equations (1-6) and (1-7). The nuclear coordinates of the excited state in equation (1-6) were set equal to those of the ground state in accordance with the Franck-Condon principle. Regarding the factor $M_{\{n_i\}\{m_i\}} = M_e \int \varphi_{u\{m_i\}}^*(Q) \varphi_{g\{n_i\}}(Q) d\tau_N$ it is Franck-Condon factor or Franck-Condon integral, it is determined by the ground state's initial vibrational levels $\{n_i\}$, and the excited state's arrival vibrational levels, $\{m_i\}$. Only the vibrational ground level ($\{n_i\} = \{0\}$) will be used as a starting point in the following calculations, assuming the system is at 0 K. With the Condon approximation, the electronic matrix element M_e is a constant factor that varies only on the involved electronic states.

1.10 Absorption spectroscopy

The quantity of photons that make the $g \rightarrow u$ optical transition by absorption radiation per unit time is

$$n_0 \cdot B_{g \rightarrow u} \cdot \rho(E) \cdot \delta(E - E_{ug}) \quad (1 - 8)$$

where, $\rho(E)$ is the energy density of the radiation field at the energy E , n_0 is the centers volume density in the g state $E_{ug} = E_u - E_g$, and $B_{g \rightarrow u}$ is the transition probability, for absorption, defined as [105].

$$B_{g \rightarrow u} = \frac{16\pi^4}{3h^2} \cdot \frac{1}{4\pi\epsilon_0} \cdot |M_{g \rightarrow u}|^2. \quad (1 - 9)$$

Since this energy lost by the field after each promotion is E , the light intensity $I(E)$ diminishes as the sample progresses, as predicted by the differential equation below.

$$-\frac{dI}{dl} = n_0 \cdot B_{g \rightarrow u} \cdot E \frac{I(E)}{c} \cdot \delta(E - E_{ug}) \quad (1 - 10)$$

where we replaced $\rho(E)$ with $\frac{I(E)}{c}$ and ignored stimulated emission term. By integration of the equation (1-10) over the sample thickness d , we acquire the notable Lambert-Beer law [106,107], It establishes an empirical link between the light intensity emitted by the sample and the incident light intensity, $I_0(E)$

$$I(E) = I_0(E) \cdot e^{-\alpha(E)d}, \quad (1 - 11)$$

where we put

$$\alpha(E) = n_0 \cdot B_{g \rightarrow u} \cdot \frac{E}{c} \cdot \delta(E - E_{ug}) , \quad (1 - 12)$$

which is termed absorption coefficient. The dimensional quantity experimentally measurable is the absorbance, $A(E) = \log_{10}(I_0(E)/I(E))$, and it is related to $\alpha(E)$ by the formula

$$\alpha(E) = 2.303 \cdot \frac{A(E)}{d} \quad (1 - 13)$$

To define the spectral form of $\alpha(E)$, we must first account for the homogeneous broadening that arises from the excited state's short duration by replacing the δ -function with a Lorentzian spectral distribution.

$$\alpha(E) = n_0 \cdot B_{g \rightarrow u} \cdot \frac{E}{c} \cdot \frac{\Gamma}{(E - E_{ug})^2 + \Gamma^2} , \quad (1 - 14) ,$$

where $2 \cdot \Gamma = h/\tau$. Others and more important contributions in vitreous systems are due to the Franck-Condon factor, which is incorporated in the Einstein coefficient $B_{g \rightarrow u}$, makes additional and more significant contributions in vitreous systems. We just present the final expression for $\alpha(E)$ because computing the relevant integral is not easy and outside the scope of this thesis:

$$\begin{aligned} & \alpha(E, T = 0) \\ &= \frac{4\pi^3}{3ch^2 \epsilon_0} \cdot n_0 \cdot E \cdot |M_e|^2 \cdot \sum_{[m_i]} \left[\left(\prod_{i=1}^N e^{-S_i} \frac{S_i^{m_i}}{m_i!} \right) \cdot \frac{\Gamma}{(E - E_{00} - \sum_{i=1}^M m_i E_i)^2 + \Gamma^2} \right] , \quad (1 \\ & - 15) \end{aligned}$$

where the main summation is applied to the entire N-dimensional set of occupancy numbers $\{m_i\}$ of the excited state's vibrational levels. E_{00} is the energy associated with the transition between the ground and excited states' lowest vibrational levels, and it is equal to $E_{00} = E_{0u} - E_{0g}$ (corresponding to the $n_i=0$ and $m_i=0$ levels in Figure 1.10 (1)), while the related transition is usually referred to as the zero phonon, or pure electronic, transition. The linear coupling or Huang-Rhys, parameters S_i is constants. [108] and can be defined as $S_i = 0.5 \cdot E_i \cdot \Delta_i^2$. The term

$$E_{00} = \sum_{i=1}^M m_i E_i, \quad (1 - 16)$$

The Lorentzian lines, which are related with the transition from the lowest level of the g state ($T = 0$ K) to the vibrational levels of the u state described by the numbers $\{m_i\}$, are focused at these energies. The warm reliance of the optical band's morphologies should be obtained when the temperature rises, considering the superposition of the Frank-Condon factors for the transition from the vibrational levels of the ground state ($\{n\}_i \neq \{0\}$) populated by the Boltzmann law. If all of the vibrational modes and their associated Huang-Rhys constants are unknown, as is the case most of the time, this methodology cannot be employed. The normal modes are divided into high and low frequency modes, which are characterized by the condition. This is a convenient technique to examine the effect of temperature. $E_i > k_B T_{\text{Max}}$ and $E_i \leq k_B T_{\text{Max}}$, respectively; where T_{Max} is the highest temperature reached during the measurements, and k_B is the Boltzmann factor. The latter are in charge of thermal effects, which are defined by a temperature-dependent thermal distribution of the population of vibrational levels in the ground state. On the other hand, because their population is constantly at the lowest vibrational levels, the contribution of high frequency modes to the band structure is unaffected by temperature. The Einstein model, which considers the coupling with these modes as due to a single mode characterized by a mean vibrational energy $\langle E_I \rangle$, a mean linear coupling constant S_I , and degeneration N_I , which equals the number of low frequency modes, is commonly assumed to treat the low frequency mode in a simplified manner. The absorption coefficient can be stated in this way in this context [109].

$$\alpha(E, T) = \alpha(E, T = 0) \otimes \frac{1}{W(T)} \cdot e^{\frac{-1}{2} \cdot \frac{E^2}{W(T)^2}}, \quad (1-17)$$

where the symbol \otimes indicates the convolution operator [109]

$$E_{00}(T) = E_{00}^* - 0.25 N_I \cdot (1 - R_I) \cdot \langle E_{II} \rangle \cdot \coth \left(\frac{\langle E_I \rangle}{2 k_B T} \right), \quad (1 - 18)$$

According to equation, the sole effect of temperature in the case of linear coupling ($E_{ig} = E_{iu}$) is a homogeneous broadening of the Lorentzian lines (1-18). Further heating impacts on the band shapes are envisaged if the linear coupling approximation is not fully satisfied. In particular, if the vibrational energies of the two states are marginally different, $0 < |E_{ug}^2 - E_{ig}^2| \ll E_{ig}^2$ (*quadratic coupling approximation*), The following equation predicts a shift in the zero-phonon energy, and consequently the absorption band, as temperature rises:

$$E_{00}(T) = E_{00}^* - 0.25N_I \cdot (1 - R_I) \cdot \langle E_{iI} \rangle \cdot \coth\left(\frac{\langle E_{iI} \rangle}{2k_B T}\right), \quad (1 - 19)$$

where, indicating with $R_i = \frac{E_{ig}^2}{E_{iu}^2}$ (quadratic coupling constant of the i-th mode), $R_I = \langle R_{iI} \rangle$ is the mean of low frequency modes constants. In equation (1-19), E_{00}^* indicates the zero-phonon energy in the case of linear coupling only (i.e. $R_i=1$).

So as to point out the effective role and the physical importance of the parameters in equation (1-17), we will consider in the accompanying the instance of the coupling with a single vibrational mode described by a vibrational energy E_h . With this suspicion eq (1-17) becomes:

$$\begin{aligned} \alpha(E, T = 0) \\ = \frac{4\pi^3}{3ch^2 \varepsilon_0} \cdot n_0 \cdot E \cdot |M_e|^2 \cdot \sum_m \left[e^{-S} \frac{S^m}{m!} \cdot \frac{\Gamma}{(E - E_{00} - \sum_{i=1}^M m_i E_i)^2 - \Gamma^2} \right], \quad (1 - 20) \end{aligned}$$

As a result, the absorption band is formed by a series of Lorentzian lines encircled by a Poisson function. The absorption band reaches its greatest at $E_A = E_{00} + S \cdot E_h$, indicating that the value of the Huang-Rhys constant S represents the vibrational level in the excited state with the highest transition probability.

For clarity, we shall represent the absorption coefficient (see equations (1-17) and (1-19)) separately from the contribution of the Franck-Condon factor in the following:

$$\alpha(E, T) = \alpha_0 \cdot E \cdot f(E - E_A, T) \quad (1 - 21)$$

where we put

$$\alpha_0 = \frac{4\pi^3}{3ch^2\varepsilon_0} \cdot n_0 \cdot |M_e|^2 \quad (1 - 22)$$

The function $f(E - E_A, T)$ is the square of the Franck-Condon factor for the mean absorption energy E_A , and it is a unitary area function, as previously described.

When the optical spectra don't have an obviously settled vibrational structure, which is the regular case in vitreous frameworks, the investigation of the test spectra as far as equations (1-18) and (1-20) don't give dependable outcomes, However, by analyzing the spectral first (M_1) and second (M_2) moments of the absorption band (moments method analysis [110], whose definitions are as follows), the vibrational dynamics of the system can be investigated.

$$M_1 = \int_0^{+\infty} E \cdot f(E - E_A, T) dE, \quad (1 - 23)$$

$$M_2 = \int_0^{+\infty} E^2 \cdot f(E - E_A, T) dE - M_1^2, \quad (1 - 24)$$

M_1 and M_2 are the mean value and variance of the function $f(E - E_A, T)$, respectively, according to these definitions. M_1 and M_2 are changed by temperature in the same way that the zero-phonon energy and homogeneous broadening are impacted by temperature (equations (1-18) and (1-19), respectively, in the same theoretical backdrop illustrated in this chapter [111]).

$$M_1(T) = M_1^0 - 0.25N_I \cdot (1 - R_I) \cdot \langle E_I \rangle \cdot \coth\left(\frac{\langle E_I \rangle}{2k_B T}\right), \quad (1 - 25)$$

$$M_2(T) = M_2^0 + N_I \cdot S_I \cdot \langle E_I \rangle^2 \cdot \coth\left(\frac{\langle E_I \rangle}{2k_B T}\right), \quad (1 - 26)$$

In these equations M_1^0 is a measure of the most likely electronic transition from the ground vibrational levels of the \mathbf{S}_0 state to the \mathbf{S}_1 state in the case of linear coupling only ($R = 1$); M_2^0 accounts for the homogeneous broadening due to the lifetime of excited states and the spectral distribution of high frequency normal modes, whose vibrational levels cannot be populated in the investigative model [109]. M_1^0 and M_2^0

account for inhomogeneous dispersion due to site-to-site non-equivalences among the point defects in the case of centers in a glassy matrix.

1.11 Luminescence spectroscopy

We'll look at the emission bands of a point defect in this section, which are defined by the energy level system shown in Figure 1.11. The system's vibrational normal modes are coupled with all of the electrical states. The system is promoted from S_0 to an excited vibrational state of S_1 ($S_{1\{mi\}}$) in a relatively short time ($10^{-15} \text{ sec}^{-1}$) due to the absorption of a photon. Then, by delivering energy to the host matrix, it relaxes toward the lowest vibrational level of ($S_{1\{0\}}$) at a typical rate of $10^{-12} \text{ sec}^{-1}$. Internal conversion, also known as vibrational relaxation, is a radiation-free process that competes with the $S_1 \rightarrow S_0$ emission rate k_S and the ISC rate k_{ISC} . When it comes to B-type activity, at room temperature, both rates are less than 10^{-9} sec^{-1} [111-114] so it is sensible to accept that the framework is totally loose to $S_{1\{0\}}$ before these emptying procedures could be viable. After the framework comes to the least vibrational level of S_1 , it can unwind or towards T_1 , by means of the ISC procedure with rate k_{ISC} , or towards S_0 by discharge of a photon with rate k_S , or by offering vitality to the host framework through non-radiative forms with rate k_{nr}^S . The framework which moves to T_1 experiences a vibrational unwinding down to the least vibrational level and afterward comes to S_0 , or radiatively with a rate k_T , or non-radiatively with a rate k_{nr}^T .

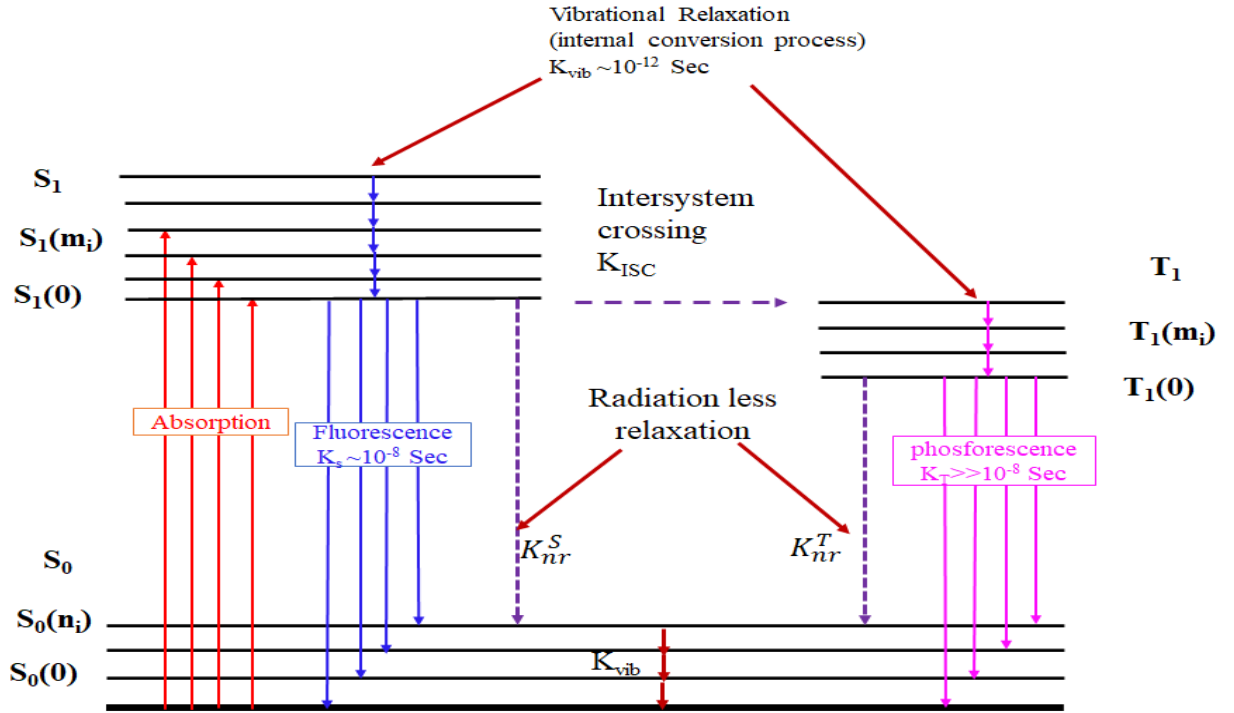


Figure 1.11 – The three energy levels scheme for a point defect. There are records of potential transitions and of the respective normal rates [115]

In concurrence with the highlights of the B-type action, in the accompanying we will accept k_{nr}^S and k_{nr}^T unimportant; accordingly, each energized focus will unwind to the ground state by emanating a photon. A framework with this component is said to be portrayed by a unitary emanation quantum yield (7). The quantity of produced photons comparing to the changes $S_1 \rightarrow S_0$ and $T_1 \rightarrow S_0$ are, in a similar request, $n_S \cdot k_S$ and $n_T \cdot k_T$, where n_S and n_T are the individual number of focuses in S_1 and T_1 . With the past presumption on k_{nr}^S and k_{nr}^T , the rate conditions related with the vitality level plan in Figure 1.11. Are

$$\begin{cases} \frac{dn_S}{dt} = p_{abs}(E_{ex}) - (k_S + K_{ISC}) \cdot n_S \\ \frac{dn_T}{dt} = k_{ISC} \cdot n_S - K_T \cdot n_T \end{cases} \quad (1-27)$$

where $p_{abs}(E_{ex})$ is the pumping rate, i.e. the number of centers excited to S_1 in the time unit, and it depends on the energy of the exciting photons E_{ex} being

$$p_{abs}(E_{ex}) = n_0 \cdot B_{g \rightarrow u} \cdot \frac{\Gamma}{(E_{ex} - E_{ug})^2 - \Gamma^2} \cdot \frac{I_0}{c} = I_0 \cdot \alpha_0 \cdot f(E_{ex} - E_A) \quad (1-28)$$

This equation is constructed using the same assumptions as the preceding section (see equations (1-17) and (1-26)), but with a uniform excitation spectrum for convenience.

In the case of steady state conditions ($dn_s/dt = dn_T/dt = 0$), we obtain

$$n_s = \frac{I_0 \cdot \alpha_0 \cdot f(E_{ex} - E_A)}{k_S + K_{ISC}}$$

$$n_T = \frac{K_{ISC}}{K_T} \cdot n_s = \frac{K_{ISC}}{k_S + K_{ISC}} \cdot \frac{I_0 \cdot \alpha_0 \cdot f(E_{ex} - E_A)}{k_T} \quad (1 - 29)$$

The same theoretical theory of absorption can be extended to luminescence in terms of spectral distribution of emitted photons, with the transition probability for emission determined by the relevant Franck-Condon factor (see Figure.1 (a) and (b))

$$M_{u \rightarrow S_0} = M_e^u \int \varphi_{S_{oni}}^*(Q) \varphi_{u_{mi}}(Q) d\tau_N \quad (u = S_1, T_1) \quad (1 - 30)$$

As a result of both the excited states life span and the electron-phonon interaction, the spectrum dependence of the S_1 and T_1 emissions is altered by homogeneous broadening.

$$S(E_{em}, E_{ex}) = k_S \cdot n_s = \frac{K_{ISC}}{k_S + K_{ISC}} \cdot I_0 \cdot \alpha_0 \cdot f(E_{ex} - E_A) \cdot g(E_{em} - E_S),$$

$$T(E_{em}, E_{ex}) = k_T \cdot n_T = \frac{K_{ISC}}{k_S + K_{ISC}} \cdot I_0 \cdot \alpha_0 \cdot f(E_{ex} - E_A) \cdot h(E_{em} - E_T), \quad (1 - 31)$$

where $T(E_{em}, E_{ex})$ and $S(E_{em}, E_{ex})$ are the distributions of the emitted photons due to the transitions $T_1 \rightarrow S_0$ and $S_1 \rightarrow S_0$, respectively. The functions $g(E_{em} - E_T)$ and $g(E_{em} - E_S)$ account for the respective line shapes and are equal to the square of the corresponding Franck-Condon integral in equation (1-30). As the function $f(E_{ex} - E_A)$, they are unitary area functions and centered in E_T and E_S , respectively. Another essential amount is the emanation intensity, those energy emitted in the unit time; it is identified with those ghastrly thickness from claiming emitted photons by the Emulating equations:

$$I_S(E_{em}, E_{ex}) = E_{em} \cdot S(E_{em}, E_{ex})$$

$$I_T(E_{em}, E_{ex}) = E_{em} \cdot T(E_{em}, E_{ex}) \quad (1-32)$$

It is worth to take note of that both the amounts characterized by equations (1-34) and (1-32) are tentatively quantifiable and, at a fixed excitation energy E_{ex} , we get elements of the emanation energy E_{em} which are by and large named photoluminescence (PL) groups. Since the trial set-up utilized for the estimations of this proposition straightforwardly gives the number of emitted photons instead of the emission intensity (see next part), we will allude in the accompanying as PL groups (or spectra) to the functions (1-31)

Since the vibrational wave functions of the excited and ground states are the same and displaced by the same amount Δ_i in the linear approximation, the amplitude of the Franck-Condon factors associated with the $\mathbf{S}_{1\{0\}} \rightarrow \mathbf{S}_{0\{ni\}}$ and the $\mathbf{S}_{0\{0\}} \rightarrow \mathbf{S}_{1\{mi\}}$ transitions, in the case of $\{ni\} = \{mi\}$, are the same.

This result reveals that the absorption and emission Franck-Condon factors obey a mirror symmetry law with respect to the pure electron transition $\mathbf{S}_{0\{0\}} \leftrightarrow \mathbf{S}_{1\{0\}}$ and the zero-phonon energy, which can thus be calculated as the mean value between the maxima of PL and OA bands. The PL band profile $g(E_{em} - E_S)$ is centered at $E_S = E_{00} - SE_h$ and, considering the respective result for the absorption, the Stokes shift is directly related to S in the case of coupling with a single vibrational mode (single effective vibrational mode approximation) with vibrational energy E_h and Huang-Rhys constant S .

$$\Delta E_{Stokes} = E_A - E_S = 2.S.E_h \quad (1 - 33)$$

Figure 1.10 (1) and (2) depicts all of these characteristics schematically.

It's worth noting that, in this homogeneous context, where all defects are supposed to be equal, changing the excitation energy simply affects the overall intensity of PL bands, not their form. In the event of a consistent spectral distribution of the light source intensity, the excitation photoluminescence (PLE) spectra obtained by altering E_{ex} at a fixed E_{em} should have the same form of $f(E_{ex} - E_A)$, the absorption coefficient divided by E_{ex} .

As talked about the absorption bands, since the optical spectra in vitreous frameworks have not an obviously settled vibrational structure, an increasingly solid investigation comprises in contemplating the unearthly minutes. The singlet (M_{0S}) and triplet (M_{0T}) zeroth minutes are

$$M_{0S}(E_{ex}) = \int_0^{\infty} S(E_{em}, E_{ex}) dE_{em} = \frac{K_S}{k_S + K_{ISC}} \cdot I_0 \cdot \alpha_0 \cdot f(E_{ex} - E_A),$$

$$M_{0T}(E_{ex}) = \int_0^{\infty} T(E_{em}, E_{ex}) dE_{em} = \frac{K_{ISC}}{k_S + K_{ISC}} \cdot I_0 \cdot \alpha_0 \cdot f(E_{ex} - E_A), \quad (1 - 34)$$

Both $f(E_{ex} - E_A)$ is solely dependent on the excitation energy, while their ratio ζ

$$\zeta = \frac{M_{0S}(E_{ex})}{M_{0T}(E_{ex})} = \frac{k_{ISC}}{K_S} \quad (1 - 35)$$

doesn't rely upon the excitation and it is a proportion of the ISC rate concerning the radiative $\mathbf{S}_1 \rightarrow \mathbf{S}_0$ emanation rate. We recently saw that the excitation energy only affects the amplitude but not the profile of the PL bands and the last two outcomes are an undeniable result. For a similar explanation, the singlet (M_{1S}) and triplet (M_{1T}) first moment are relied upon to be autonomous on E_{ex} . Considering the properties of the functions $g(E_{em} - E_S)$ and $h(E_{em} - E_T)$, we in fact get

$$M_{1S} = \frac{1}{M_{0S}(E_{ex})} \cdot \int_0^{\infty} S(E_{em}, E_{ex}) dE_{em} = E_S$$

$$M_{1T} = \frac{1}{M_{0T}(E_{ex})} \cdot \int_0^{\infty} T(E_{em}, E_{ex}) dE_{em} = E_T \quad (1 - 36)$$

The ISC rate k_{ISC} (see condition (1-16)) and the electron-phonon coupling with the coupled low recurrence vibrational techniques of the \mathbf{S}_1 state are both affected by temperature.

1.12 Transient absorption spectroscopy

As talked about in the past segment, when an inside is eager to \mathbf{S}_1 , it is acquired a non-balance position thus it unwinds toward the \mathbf{S}_1 harmony setup under the impacts of inner transformation. At that point, in concurrence with the B-type movement

conspire, the S_1 state will rot by radiative discharge in a nsec time scale. Concerning the unwinding elements, they happen in a sub-psec time space.

Higher excited states, in particular the second excited singlet and triplet states S_2 and T_2 , as shown in Figure 1.11 (1), must be included in a fuller framework of the electronic levels of point defects responsible for B-type activity.

An $S_1 \rightarrow S_2$ transition could be triggered before the S_1 decay if we consider the system's S_2 state. A transient absorption (TA) is a process of absorption between excited states, and the optimum experiment to quantify a TA has two steps: (i) an intense light pulse (referred to as the pump) excites a large number of centers from S_0 to S_1 in order to maintain a sufficient population in S_1 , the starting state; (ii) a second pulse (referred to as the probe) triggers the $S_1 \rightarrow S_2$ transition. A schematic diagram of a TA is shown in Figure 1.12 (2). The depletion of the probe intensity ΔI in comparison to the probe intensity I_0 without the pump pulse is the measured quantity. The theoretical treatment is identical to that of a typical absorption, but with the added precaution of working in a linear regime.

we can assume $I_{probe} = I_0 \cdot e^{-\alpha d}$ obtaining

$$\frac{\Delta I}{I_0} = \frac{I_0 - I_{probe}}{I_0} = 1 - e^{-\alpha d} \quad (1 - 37)$$

Where I_{probe} is the probe intensity coming out of the sample, d is the sample thickness, and α is the absorption coefficient for the $S_1 \rightarrow S_2$ transition. Furthermore, in the situation of low absorption, the equation (1-37) can be approximated by:

$$\frac{\Delta I}{I_0} \cong \alpha \cdot d \quad (1 - 38)$$

As a result, the experimentally measurable ratio $\Delta I/I_0$ provides a direct measure of the $S_1 \rightarrow S_2$ transition's absorption coefficient. It's worth noting that, in comparison to traditional absorption, time is introduced as a new parameter: the probe can be purposely delayed with respect to the pump in order to investigate the S_1 state at various times after excitation. If the $S_1 \rightarrow S_2$ transition occurs before or after total internal relaxation, we can distinguish two regimes (see Figure 2.3(2)). *In the first*

case, the atoms will not be in the S_1 equilibrium position, the $S_1 \rightarrow S_2$ absorption coefficient may be different in this configuration, and a temporal dependence of during relaxation is expected. *In the second case*, the absorption mechanism is similar to the $S_0 \rightarrow S_1$ transition already discussed. The main difference lies in the dependence of α on the S_1 population n_S (see equation (1-20)), which is time dependent, accordingly to a pure exponential time decay with decay rate $k_S + k_{ISC}$ (see equation (1-35) and related discussion). So, the probe depletion signal is expected to decrease with the same time constant of the luminescence signal.

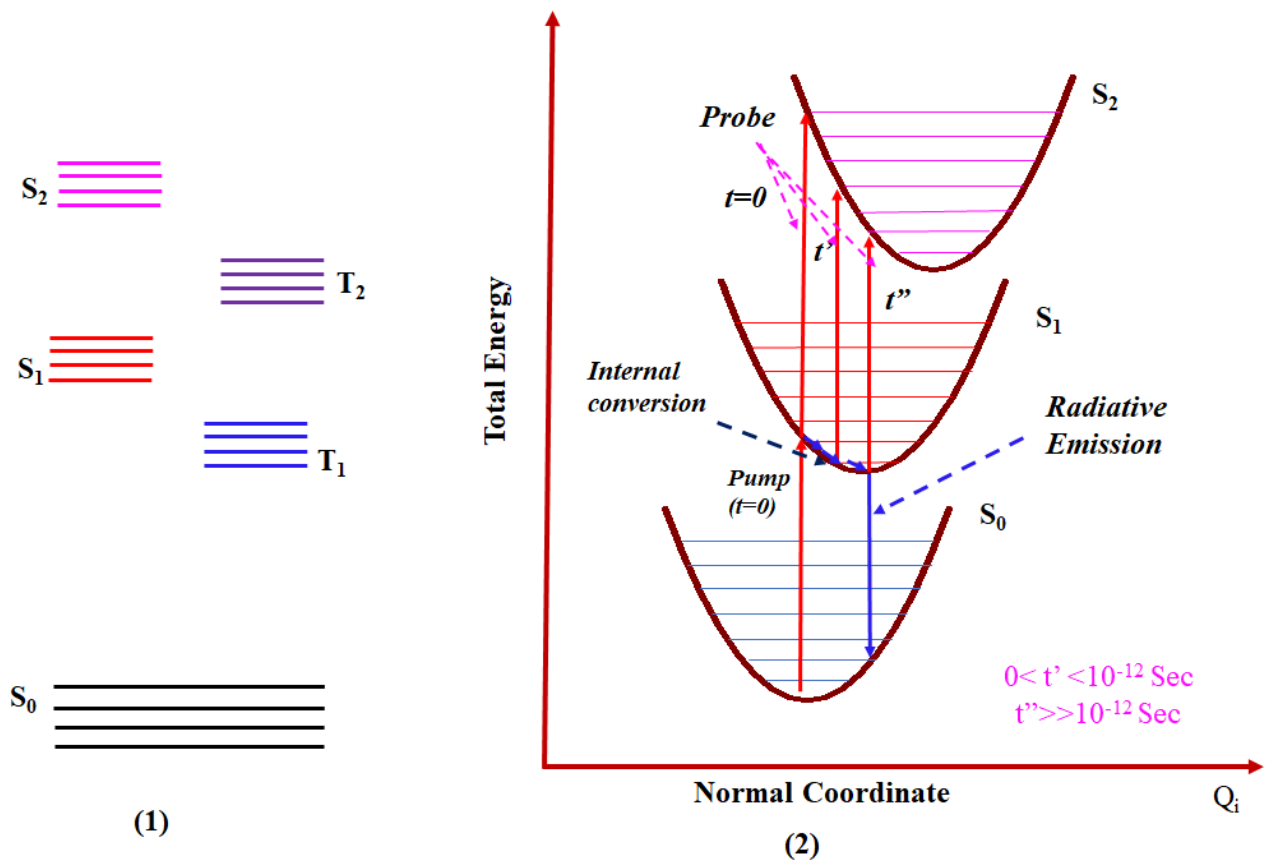


Figure 1.12. (1) S_2 and T_2 , the second excited singlet and triplet states, are included in the B-type energy levels system, respectively. (2) Schematic picture of a transient absorption from S_1 to S_2 (see text). The internal conversion and the $S_1 \rightarrow S_0$ emission are also shown. Three cases are depicted: the probe and the pump pulses are simultaneous ($t=0$); the probe induces the transition during the internal conversion (t'); the probe arrives after the thermalization to S_1 minimum (t'').

1.13 Conclusions

1. A review of the data on the electronic structure of Silica glass showed that the atomic structure of an ideal Silica glass network is determined by the short-range and average order, which affect the electronic-optical properties of the material.
2. The influence of dry and wet oxidation methods on the composition and optical characteristics of Silica glasses is considered. The dry oxidation method has been shown to yield cleaner samples with a wider optical slit.
3. A review of all varieties of intrinsic defects of point and continual origin in a real mesh of silica glass is performed. The main spectroscopic and luminescent characteristics of intrinsic defects and their influence on the electronic structure of the material are considered.
4. The performed review shows that point defects of pure silica glass have a decisive effect on the optical properties of the material, and therefore their modification can be used to control the functional properties of SiO_2 .
5. We outline gives an overview briefly the theoretical background on the optical properties of a generic point defect.

CHAPTER 2. SAMPLES AND EXPERIMENTAL TECHNIQUES

The properties of defects in silica are studied in parallel studies using various methods of sample processing and measurement. The usual experimental method consists in varying the concentration of defects, either during growth processes (synthesis, doping), or using external agents in the produced material (irradiation, heat treatment, drawing), as well as to search for interrelated changes in measurable properties. In particular, while diamagnetic defects are studied through their optical activity as optical absorption (OA) and photoluminescence (PL), paramagnetic defects can also be studied using electron spin resonance (EPR) spectroscopy, which is a powerful tool for determining defect structures at the atomic level.

2.1 Ion implantation

Solid-state image sensor technology has come a long way in the last four decades, and it has found success in the market. Because of the exponential expansion of the mobile phone market, picture sensor sales reached 4.2 billion pieces in 2015. Image sensor applications are popping up all over the place, not only on mobile phones. Various device and process technologies have been created during the history of image sensors. Ion implantation is one of the most essential process technologies for image sensors among them. Image sensors, on the other hand, are a critical application for the development of ion implantation technology. To begin, numerous ion implantation processes are used to manufacture particular structures, such as the PPD (pinned photodiode) [116-117], unique isolation structure [118], and transistor tuning at pixels [119]. High energy implantations with precise angle control, as well as high aspect ratio resist patterns, are necessary to achieve deep PD (photodiode).

2.1.1 Basics of ion implantation technology

W. Shockley, one of the creators of transistors, filed an ion implantation technology patent in 1949. In the early 1970s, it was used to a mass-production line. As a result, it might be considered a relatively novel process technology. Ion implantations were

originally utilized to adjust the threshold voltage of MOS (Metal Oxide Semiconductor) transistors. They've been customized for a variety of uses since then.

- a. Controlling the voltage at which a threshold is reached.
- b. Doping with a high density, such as source–drain formation.
- c. SIMOX (oxygen implantation for separation) [120]. To obtain SOI (silicon on insulator) wafers, silicon dioxide layer is generated via oxygen implantation.
- d. Delamination [121] is a kind of delamination. At temperatures exceeding 500°C, a delamination layer is formed by high-dose hydrogen implantation, and a thin silicon layer is split. A wafer–bonding approach is used to make SOI wafers using this phenomena.
- e. Proximity gettingtering [122]. To produce gettering sites near the front active layer, oxygen or carbon is implanted. The precision of ion implantation allows for repeatable gettering site formation, and proximity gettering is effective because the gettering sites are close to the front side active area.
- f. Termination of a dangling bond [123]. To end dangling bonds, fluorine is injected. The number of GR (generation recombination) centers in the interface state is reduced, and the leakage current is lowered. Also reduced is 1/f noise and random telegraph signal (RTS) noise.
- g. Amorphous formation [124] An amorphous layer is formed when a high dose of implantation is used. It prevents the channeling effect from occurring, which will be discussed later. It also aids in re-crystallization and electrical activation after ion implantation during the annealing process.
- h. Co–implantation [125] When dopant atoms are implanted with carbon, nitrogen, or fluorine atoms, impurity diffusion is reduced. Ion beam technology also includes focused ion beam (FIB) and secondary ion mass spectroscopy (SIMS).

Ion implantation offers the following distinguishing characteristics:

- (1) The doping amount is exact enough throughout a five-decade period, ranging from 10^{11} to 10^{16} ions/cm².
- (2) The ion energy determines the doping profile or depth.

- (3) Photo-resist patterns are used to select the doping area.
- (4) If the ion energy is chosen correctly, doping can be done via a thin dielectric layer on the surface.
- (5) Atoms, molecules, and clusters of various species can be implanted.
- (6) Sputtering occurs when ion beams are used. The advantages of ion implantation method are (1) to (5), while metal contamination, damage, and channeling are downsides for image sensors.

2.1.2 Advantages and general features of ion implantation technology

As a result of their use in semiconductor device manufacturing, ion beam accelerators are now widely available for most ion species with energies up to hundreds of keV. Ion beams may require more energy to penetrate deeper into targets for optical equipment, however there are various van de Graaff accelerators that are suited for gas ions. Surface change is only required on the scale of a few wavelengths for optical effects, therefore the implanted layers will be only a few microns thick at most. Semiconductor devices are noteworthy in that components can be densely packed onto a silicon slice using sub-micron beam defining masks. Similar lithography is required for optical applications, however bigger masks will be required in some circumstances for deep implantation.

The following are some of the obvious benefits of ion implantation doping. (i) Because the ion beam is measured as a current, accurate control of the number of ions implanted is straightforward. (ii) Because the ion energy controls the depth of the implant, a careful selection of energy and dose can produce any desirable impurity profile under the surface. (iii) In the case of 'troublesome' materials that disintegrate, an overlay may be used to create the implant. (iv) Conventional solubility rules do not limit the implant ion choice; any ion can be employed. (v) Different ions can be positioned at various depths. (vi) Because implants can be manufactured at any target temperature, impurity doping can be used in low-temperature crystal phases. (vii) Because ion accelerators produce isotopically pure beams, analysis methods like EPR and NMR, which rely on nuclear spin interactions, are made easier.

Thermal diffusion has been widely used to dope surface layers in semiconductor and metal technologies. The approach is limited by the requirement for high temperatures; the diffusion profile is peaked near the surface, and diffusion along dislocation lines can proceed at unmanageable rates. When diffusion is combined with a mask, the diffused material's lateral spread is comparable to the penetration normal to the surface. Many of these characteristics are avoided in ion beam doping procedures, but there is no reason why the two approaches should not be combined: ion beams supplying a highly regulated, isotopically pure diffusion source or secondary ion beam doping of extensively doped diffused layers.

Ion implantation has the apparent drawback of displacing many atoms in the target. Because this radiation damage is undesirable in semiconductors, complex thermal anneal cycles employing electron beams or lasers have been devised to remove the damage while preventing the implanted ions from spreading. However, the term "radiation damage" might be deceptive because in many applications, such as the production of optical waveguides, the fundamental goal of the implantation is lattice amorphization. To encompass both impurity doping and atomic displacements, it would seem preferable to use the less emotive phrase "ion beam alteration of materials." For academic color center investigations or the use of ion beams to produce new materials, cost issues may not be as relevant, and the ability to swiftly synthesize a wide variety of composition is critical for novel materials. However, after a new material has been chosen, production can resume using more traditional methods. If ion beams are to be used in a commercial process, they must provide a cost advantage, a quality control advantage, or something new. The rationale for semiconductors is evident, as all of these qualities assist chip manufacture, and the devices have a high inherent value per unit area.

2.2 Ion implantation of rhenium into silica glass

The description of the technology of synthesis of objects of research, measuring installations and experimental techniques is given.

SiO₂ samples were represented by three types of glasses of the KI, KUVI and Hongan brands (China, Hongan Silica Glass Store). The samples were irradiated with Re ions using MEVVA (Institute of Electro-physics, Ural Branch of the Russian Academy of Sciences, Yekaterinburg) and Raduga-3M (Physics and Technology Institute, State University, Nizhny Novgorod) in a repetitively pulsed regime.

1. Samples of KUVI glass (10 × 10 mm, thickness 1.5 mm) belonging to type IV were implanted with Re ions with an energy of 30 keV in a MEVVA-type device (Institute of Electro-physics, Ural Branch of the Russian Academy of Sciences, Yekaterinburg). The rhenium ion beam was generated in a pulse-periodic mode with a pulse duration of 0.4 ms and a repetition rate of 25 Hz. The used ions flux densities were 5×10^{15} , 10^{16} , 5×10^{16} , 10^{17} and 5×10^{17} cm⁻².
2. Glasses brand KI 10 × 10 mm² and 0.5 mm thick, was implanted with Re ions with an energy of 80 keV on an ion-plasma source "Raduga-3M" (Physics and Technology Institute, Lobachevsky National Research University, Nizhny Novgorod) in a pulse-periodic mode with a pulse duration of 0.2 ms and a pulse repetition rate 30 Hz. The used ions flux densities were 5×10^{16} , 10^{17} , and 2.5×10^{17} cm⁻². Thermal annealing of the implanted samples was carried out in air at 1000 °C for 1 h. X-ray photoelectron spectroscopy (XPS) was used to certify the obtained samples. The measurements were carried out on a Thermo Scientific™ K-Alpha +™ XPS spectrometer.

To assess the effect of the type of ions on the change in the properties of silica glasses of various brands, samples of Hongan glass made in China (Hongan Silica Glass Store), implanted with various fluences of bismuth ions with an energy of 30 keV, were additionally used.

2.3 Optical absorption spectroscopy

The optical absorption spectra at room temperature were recorded using a Perkin Elmer Lambda 35 spectrophotometer equipped with an integrating sphere (Figure 2.1). The measurements were carried out in the spectral range 200-1100 nm. The spectrophotometer is equipped with two automatically switching radiation sources - a deuterium lamp operating in the wavelength range of 200-340 nm and a halogen incandescent lamp operating in the wavelength range of 340-1100 nm. The spectral width of the slit during measurements was 0.5 nm. The resolution was not less than 0.3 nm.

Spectra were recorded by automatic wavelength scanning in 1 nm increments. Tools are controlled, data is obtained and processed using a personal computer and software origin lab

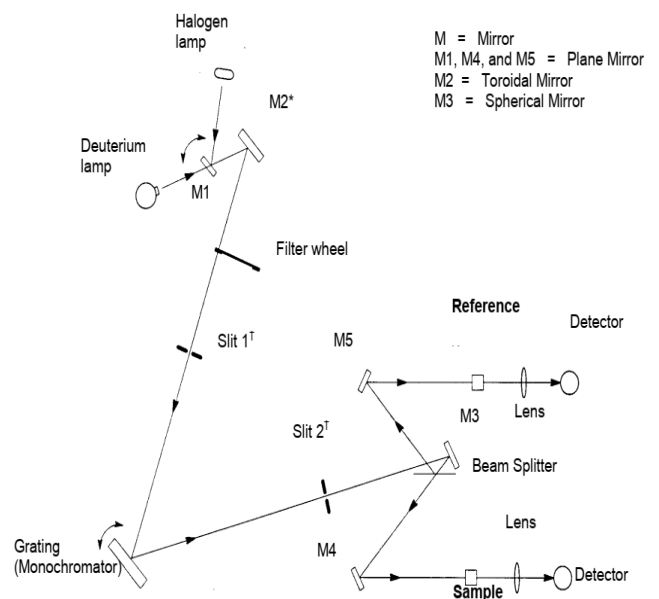


Figure 2.1 – Perkin Elmer Lambda 35 UV/Visible Spectrophotometer(left), Optical circuit diagram in a spectrophotometer Perkin Elmer Lambda 35 (right)

2.4 UV-VIS luminescence spectroscopy

The photoluminescence and excitation spectra at room temperature were recorded using a Perkin Elmer LS 55 spectrometer. An excitation source was a 150 W xenon lamp operating in a pulsed mode with a frequency of 50 Hz. The spectrometer is equipped with two monochromators of the Monk-Gillison scheme, providing a working wavelength range of 200-900 nm. The accuracy of setting the wavelength is ± 1 nm. The spectral width of the slit of the input and output monochromators was set at 2.5 nm. A high-precision R-928 photomultiplier was used as a detector, providing a signal-to-noise ratio better than 750/1. The resolution was not less than 0.5 nm. The luminescence decay curves were recorded in a dynamic mode with a stepwise change in the delay time ($\Delta t = 20 \mu\text{s}$). The device was controlled using a personal computer and FL WinLab software (Figure 2.2)

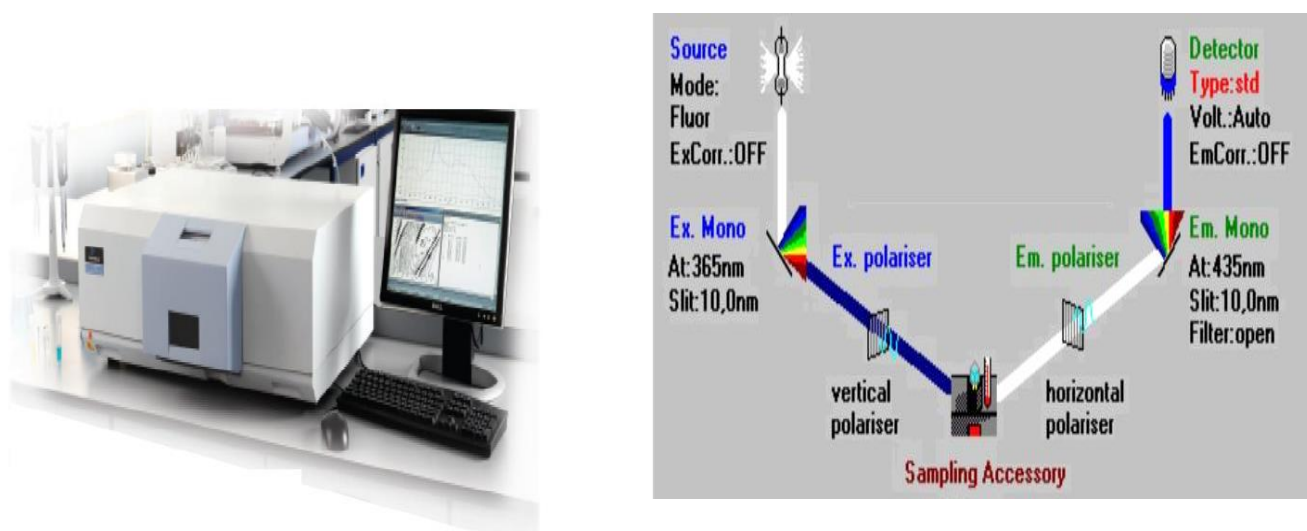


Figure 2.2 – Luminescence spectrometer Perkin Elmer LS 55 (left), Scheme of photoluminescence measurements on Spectrometer Perkin Elmer LS 55 (right)

2.5 Absorption and luminescence spectroscopy in vacuum ultraviolet

The temperature dependences of the absorption and luminescence spectra in vacuum ultraviolet were obtained using the McPherson VuVAS 1000 PL spectroscopic complex (Figure 2.3).

The unit is equipped with The Model 225 high-performance vacuum monochromators, a focused deuterium light source, a sample chamber with the possible fixation of several objects a set of detectors and a system of turbomolecular pumps, providing a vacuum at a level of 10^{-4} Pa. Measurements were carried out at low temperatures using a helium cryostat Janis CCS-450. The temperature of the samples varied in the range of 8-300 K and was monitored using a resistance thermometer.

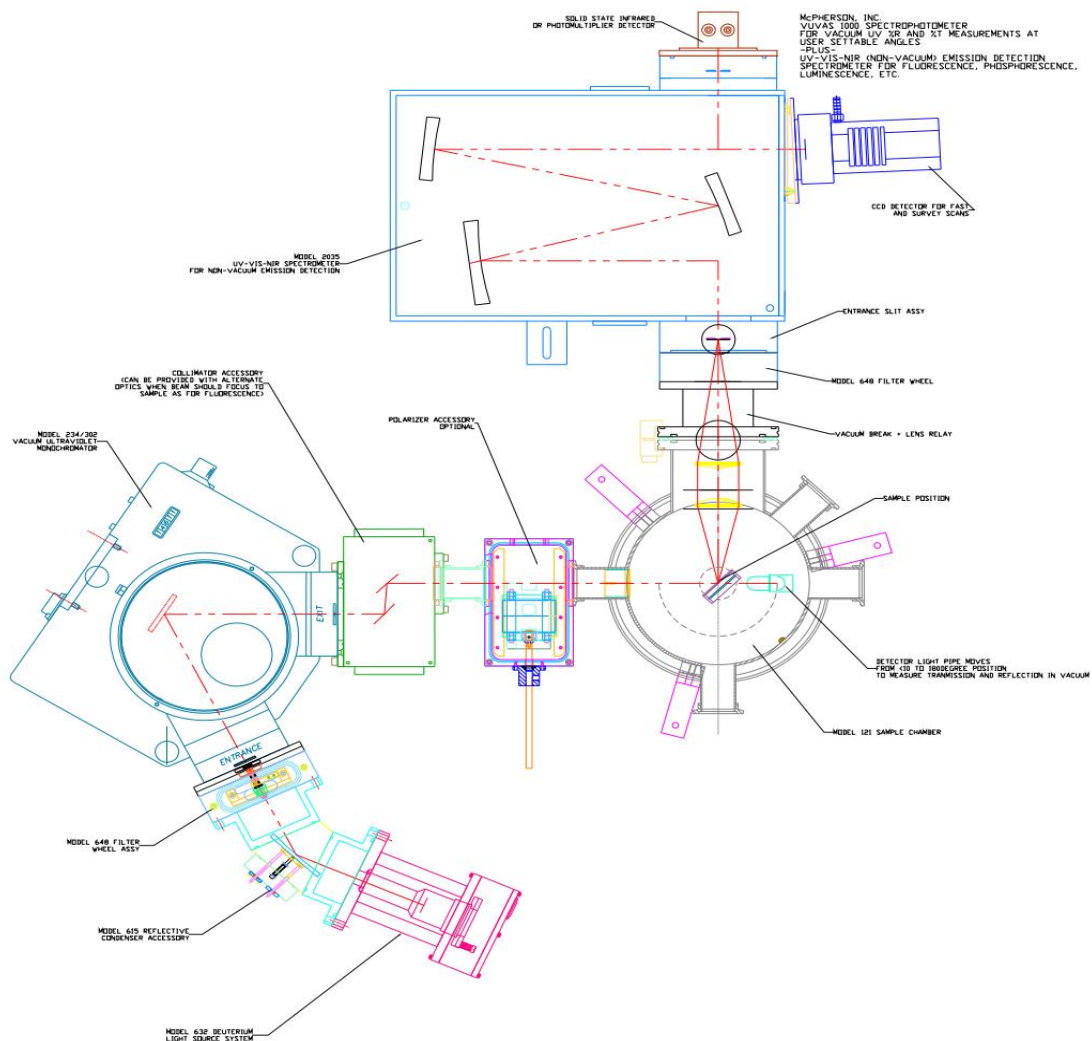


Figure 2.3 – Diagram of the optical path in the spectroscopic complex McPherson VuVAS 1000 PL

The spectral slots of the input and output monochromators were 0.5 nm, and the accuracy of setting the wavelength was 0.1 nm. The resolution was not less than 0.1 nm. The operating wavelength range was 120–500 nm for the optical absorption mode and 300–800 nm for the photoluminescence mode. The hardware capabilities of the experimental complex make it possible to obtain detailed information on the dynamics of short-lived excited states.

Optical absorption spectra were recorded on a McPherson VuVAS 1000 PL VUV spectrometer in the wavelength range of 150–350 nm Figure 2.4. All measurements were performed at room temperature.

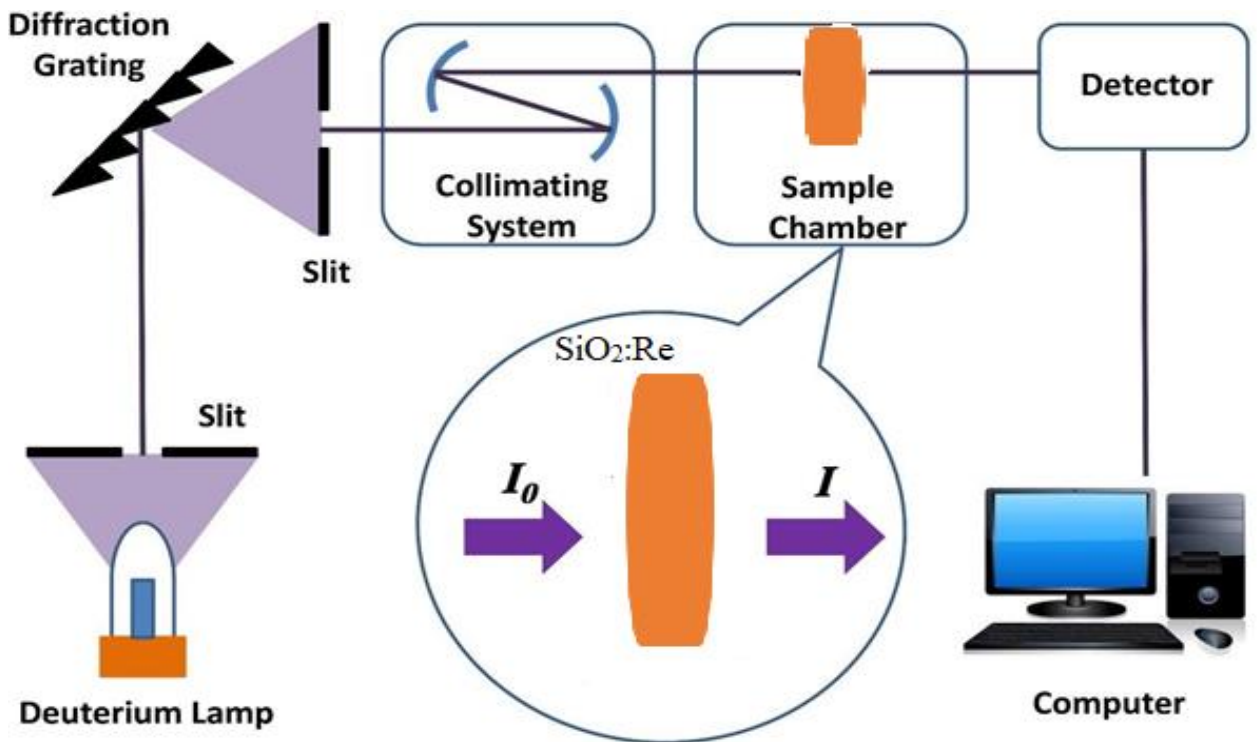


Figure 2.4 – Schematic image of the method for measuring the optical absorption of SiO₂: Re. I_0 and I are the intensities of the incident and transmitted radiation, respectively.

The processing of the absorption spectra and the approximation of the spectral dependences of the fundamental absorption edge was carried out using the Origin Pro 9.1 application.

2.6 Electron paramagnetic resonance spectroscopy (EPR)

It is possible to apply EPR spectroscopy to structures with a non-zero electronic magnetic moment resulting from electron spin and orbital angular momentum. The sample under study is situated in two external magnetic fields pointing in orthogonal directions in a standard EPR experiment. As a consequence of the interaction of the electronic magnetic moment with H , the first field, H , causes the ground state energy levels to scatter, the resulting splitting being around 0.3 cm^{-1} for magnetic fields of about 300 mT. The second external magnetic field, H_1 ($|H_1| \ll |H|$), with a microwave frequency oscillating amplitude, is used to cause resonant transitions between states separated by H . [131,132] In particular, the importance of EPR spectroscopy is related to its ability to provide valuable information on the microscopic structure of the paramagnetic centers being examined. Typical structures that are subject to EPR spectroscopy include

- I) solated atoms and ions;
- II) Ions of the transition metal and actinide group in solids;
- III) Localized imperfections in solids (point defects);
- IV) Systems with conduction electrons

2.7 Conclusions

1. The objects of study were samples of glassy SiO_2 of the KI and KUVI types implanted with various fluences of Re ions with energies of 80 and 30 keV.
2. To study the penetration depth of Re ions into the glassy matrix, SRIM modeling methods were used.
3. The certification of the obtained samples with the analysis of their chemical composition, including varieties and percentage of impurities, was carried out by the method of X-ray photoelectron spectroscopy.

4. To study the spectral-optical and spectral-luminescence properties of the samples, we used experimental methods of optical absorption and photoluminescence spectroscopy.
5. The study of the temperature dependences of the optical properties of the samples in the temperature range 8–500 K was carried out using a helium cryostat on a McPherson vacuum spectroscopic complex.
6. For the study of paramagnetic centers Silica glass arising in the ion-beam exposure used electron spin resonance method.
7. The entire set of experimental and computational research methods makes it possible to perform a comprehensive study of the electron-optical, luminescent and paramagnetic properties of quartz glasses of two types implanted with Re ions and to obtain extensive information about the changes that have occurred in them.

CHAPTER 3. OPTICAL AND LUMINESCENCE PROPERTIES OF OXY-GEN-DEFICIENT CENTERS IN KUVI GLASS IMPLANTED WITH 30 KEV RE IONS

3.1 Samples characterization by methods SRIM and X-ray photoelectron spectroscopy (XPS)

The first host matrices for pulsed ion implantation were KUVI glasses (type IV). Great-frequency plasma oxidation of the respective starting components produces this form of glass, which has high transparency in the visible, UV, and IR spectral ranges and improved radiation resistance. Trace impurities have a total concentration of less than 10^{-3} weight percent. The closest technological analogues of this type of glass are Spectrosil TMVF (Great Britain), Suprasil TMW (Germany), and Corning 7943TM [133].

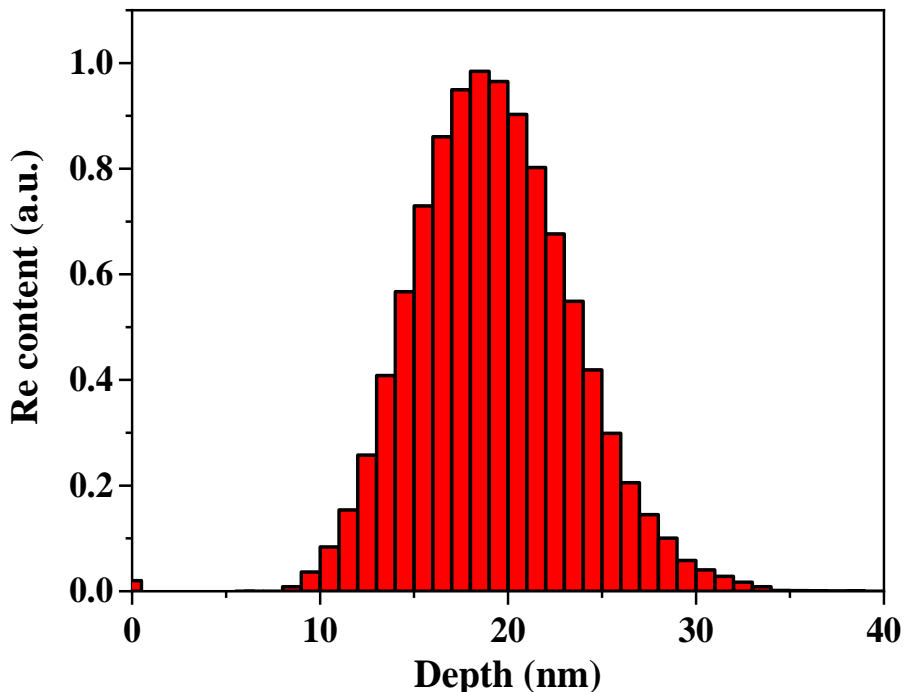


Figure 3.1 – Calculated implantation profile of Re^+ ions in the volume of SiO_2 glass ($E_{\text{exc}} = 30 \text{ keV}$) [13].

To calculate the penetration depth of Re^+ ions into for the studied SiO_2 samples, we used the software package for computer simulation Stopping and Range of Ions in Matter (SRIM), based on quantum-mechanical calculations of ion-atom collisions [134]

The calculation results showed that the introduction of rhenium ions with an initial energy of 30 keV into the surface layer of SiO_2 occurs in the depth range of 10–40 nm Figure 3.1 The maximum of the distribution of implanted ions corresponds to a depth of 22 nm. The obtained samples of implanted glasses were previously characterized by the methods of X-ray photoelectron spectroscopy (XPS) and density functional (DFT) simulations for replantation scenarios were reported in reference [5,135] to distinguish between implanted KUVI- SiO_2 glasses.

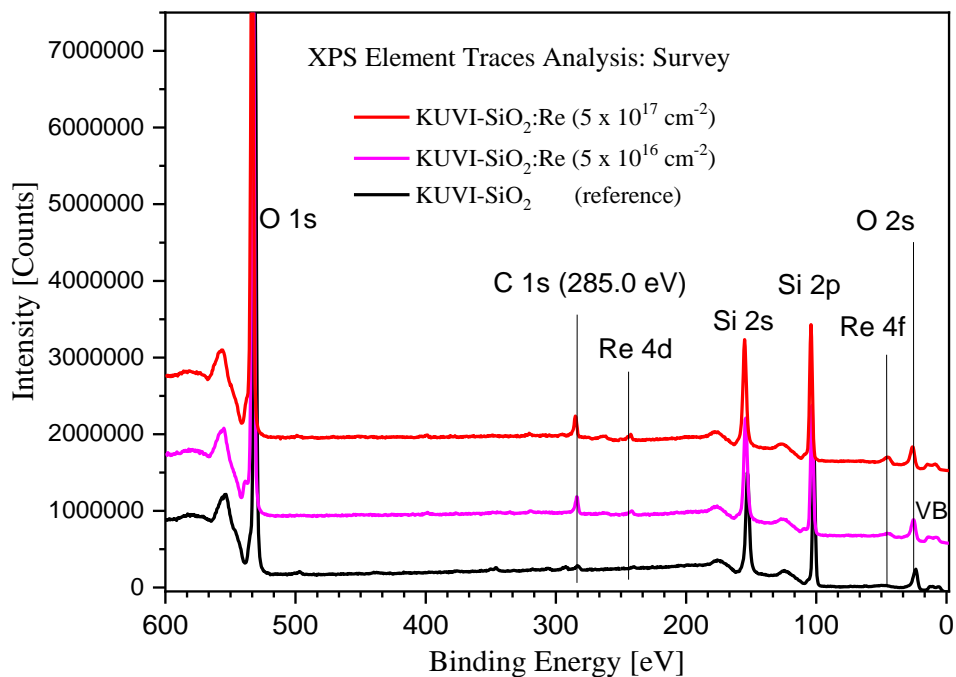


Figure 3.2 – XPS element trace analysis of Re implanted KUVI- SiO_2 glasses.

Only most typical survey spectra are shown. Carbon C 1s marker was applied for calibration (see details in [13,136]).

According to the known maximum depth resolution of -98-9 nm from XPS technology, this method will only cover the beginning of the estimated SRIM depth profile. However, the Thermal Scientific K-Alpha + XPS [5] showed a detection limit for

element concentrations of 0.05% atom%, so it successfully allowed us to analyze trace elements in our samples.

Currently, there are no foreign contaminants in the implanted KUVI-SiO₂ glasses after implantation in Figure 3.2 Therefore, we believe that the general structural damage in the test objects is mainly caused by internal radiological damage caused by implanted ions.

3.2 Optical absorption spectra of silica glass with rhenium ions

The absorption spectra of silica and Re implanted SiO₂ are shown in Figure 3.3(a) The ion-beam irradiation of silica matrix leads to a deterioration of its optical transparency in the spectral region of near UV. Significant increase in the absorption coefficient at energies of 2–8 eV is due to the formation of intrinsic optically-active defects in SiO₂ host after ion irradiation. Silicon dioxide is characterized by a variety of point defects that are formed as a result of the interaction with accelerated particles and high-energy radiation [137-139].

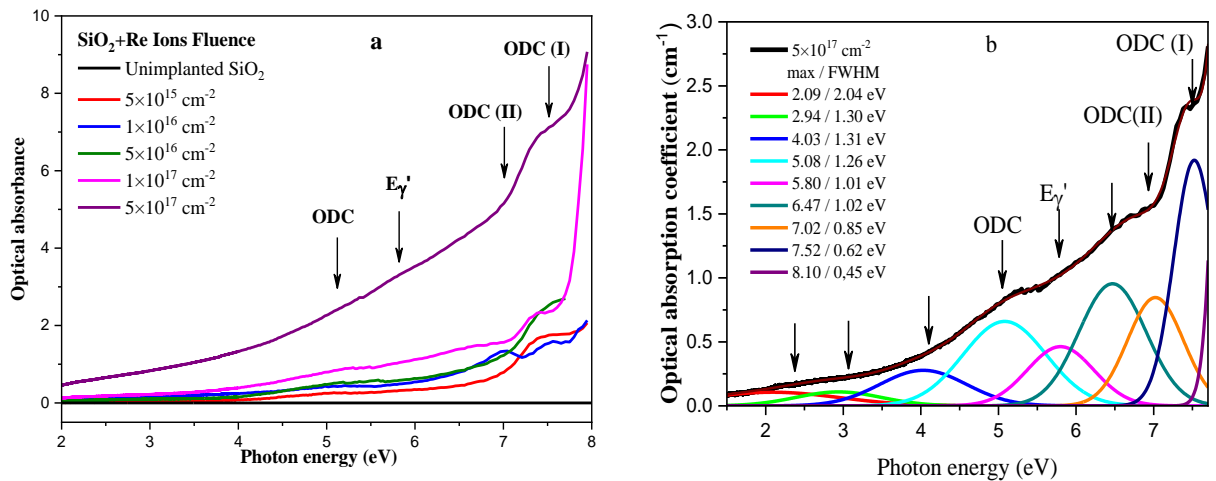


Figure 3.3 – Optical absorption (OA) spectra of SiO₂ implanted with Re ions with different fluences (a) and (b) the difference optical absorption spectrum after deconvolution for SiO₂ implanted with a rhenium fluence of 10¹⁷ cm⁻²

For a further more detailed analysis, the difference spectrum of optical absorption was selected, measured on silica glass implanted with a fluence of 10^{17} cm⁻² of rhenium Figure 3.3 (b) The spectrum was decomposed into Gaussian components to highlight the main absorption bands.

It was revealed that the OA spectrum of the studied samples contains eight bands, four of which: 5.1, 5.8, 7.0, and 7.5 eV can be attributed to the varieties of oxygen-deficient centers [58, 140, 141]. The 5.8 eV optical band is associated with a three-coordinated silicon atom (E_{γ}^I) [58, 143]. The bands at 5.1 and 7.0 eV correspond to the oxygen divacancies Si-ODC (II), 7.5 eV - to the neutral oxygen vacancy Si-ODC (I) [58, 140-142]. And the 6.3 eV band is due to the centers associated with Re ions.

3.3 Photoluminescence spectra upon excitation in the near ultraviolet

The photoluminescence (PL) spectra of Re implanted SiO₂ under excitation of 4.77 eV at room temperature are shown in Figure 3.4(a) The photoluminescence excitation spectra at emission 2.53 are shown in Figure 3.4(b) When luminescence is excited by light quanta with an energy of 4.77 eV, the intensity of all PL bands increases with increasing fluence from 5×10^{15} to 1×10^{17} cm⁻² [144].

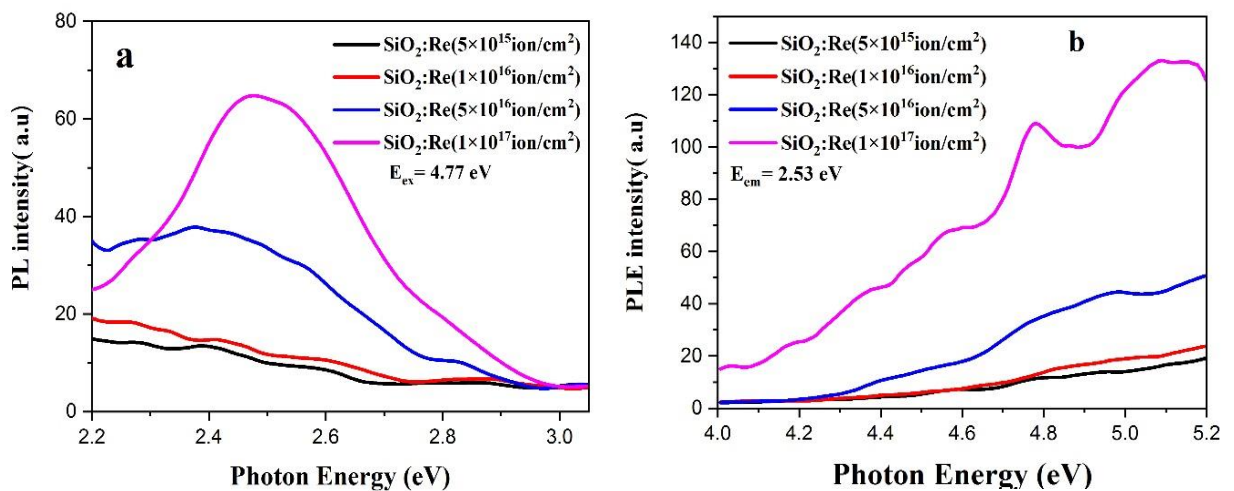


Figure 3.4 –The PL spectra of Re implanted SiO₂ with different the ion fluences at excitations of 4.77 eV (a) and (b) emission of 2.53 eV after thermal annealing (1000 °C, t = 1 h)

Figure 3.5 shows the photoluminescence (PL) spectra of Re implanted SiO₂ with a non-elementary feature and a variety of bands corresponding to different defect centers. With the PL band at 2.7 eV, we can differentiate oxygen-deficient center (ODC(II)), which is characteristic for silica glass and relates to the two-coordinated silicon atom [5,145,146].

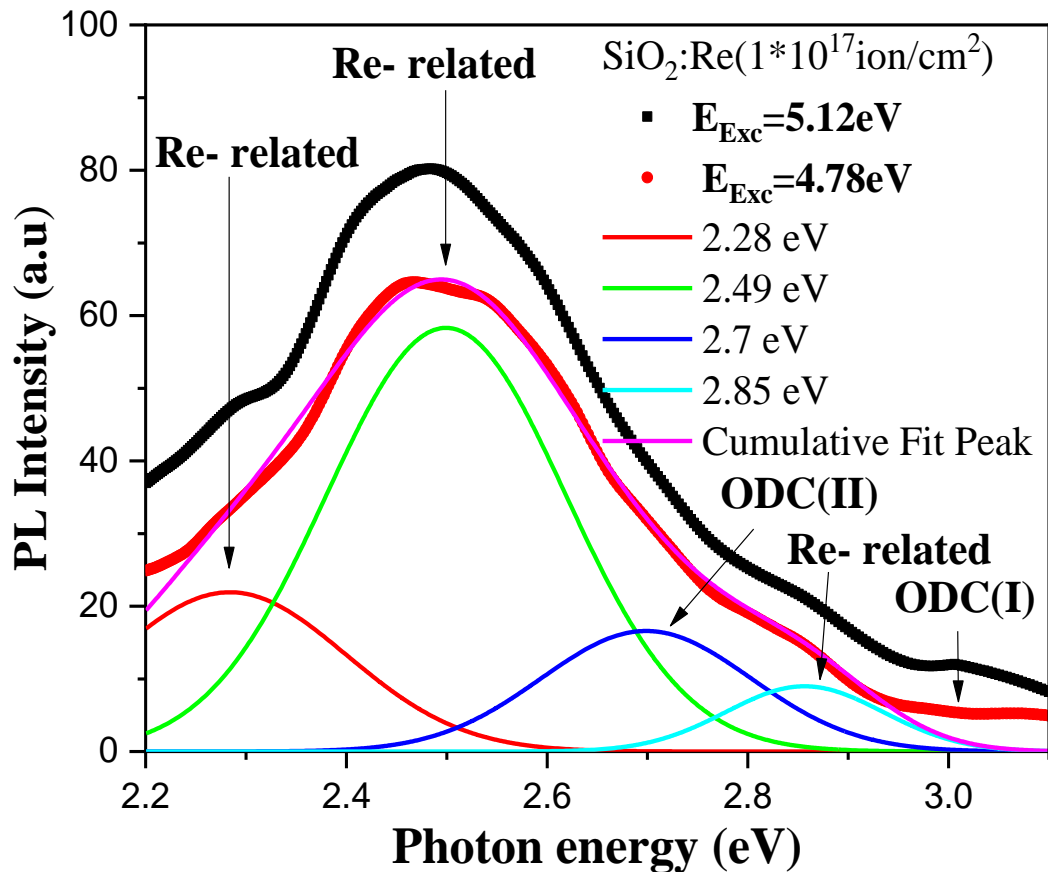


Figure 3.5 – The photoluminescence (PL) spectra for SiO₂: Re glass after thermal annealing. Arrows indicate the different types of Luminescence centers after deconvolution

At the same time, the main contribution in overall PL intensity is determined by the band with a maximum of 2.53 eV, caused to the Re-related centers. Notes, that under excitation of ODC we observe the PL of Re-related centers. It indicates the energy transfer between these centers occurs. Thermal annealing causes increasing the intensity of all PL bands and shifting of their maxima to the low-energy region. The main spectral parameters of emission bands are listed in Table 3.1.

Table 3.1 – Spectral parameters of PL and PLE bands for silica glass implanted with rhenium ions after thermal annealing

PL band	Re-related	ODC(II)	ODC(I)
Excitation = 5.12 eV			
h ν , eV	2.5	2.71	3.01
FWHM, eV	0.24	0.34	0.3
PLE band	Re-related	Re-related	ODC
Emission= 2.53 eV			
h ν , eV	4.35	4.78	5.12
FWHM, eV	0.28	0.19	0.49

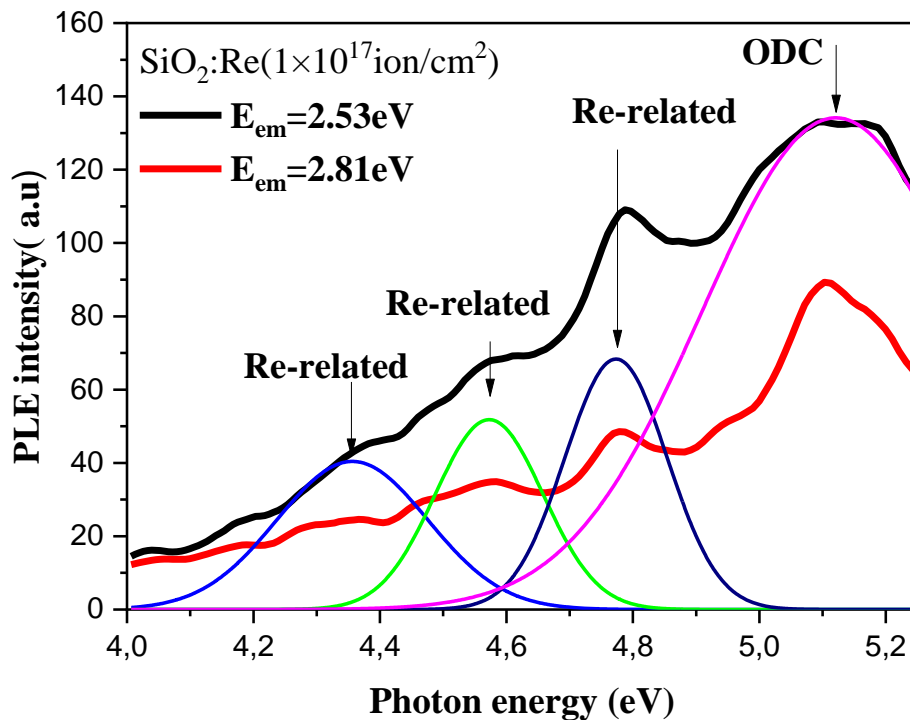


Figure 3.6 – The photoluminescence excitation (PLE) spectra for SiO₂: Re glass after thermal annealing. Arrows indicate the different types of Luminescence centers after deconvolution

The photoluminescence excitation (PLE) spectra of Re implanted SiO_2 , shown in Figure 3.6, At both 4.78 and 5.12 eV excitations, there are all PL bands (ODC and Re related center), but the emission of ODC(II) dominates regardless of the excitation energy [147]. When the excitation changes from 5.12 eV (transition in ODC) to 4.78 eV (transition in Re related center), a change in the ratio of the integrated PL intensities is observed in favor of the Re related center. Such features indicate the effective mutual energy transfer between two types of ODCs and Re related center.

The Scheme of electronic transitions for ODCs and Re related center is shown in Figure 3.7. At both excitations of ODC (5.12 eV) and Re related center (4.78 eV), there are three pathways followed by photons emission: (1) energy transfer of ODC(II) (2.71 eV); (2) energy transfer of ODC(I) (3.01 eV), (3) energy transfer of Re-related center (2.53 eV). Therefore, the obtained results indicate the possibility of modifying the luminescent properties of SiO_2 glass by implantation with rhenium ions

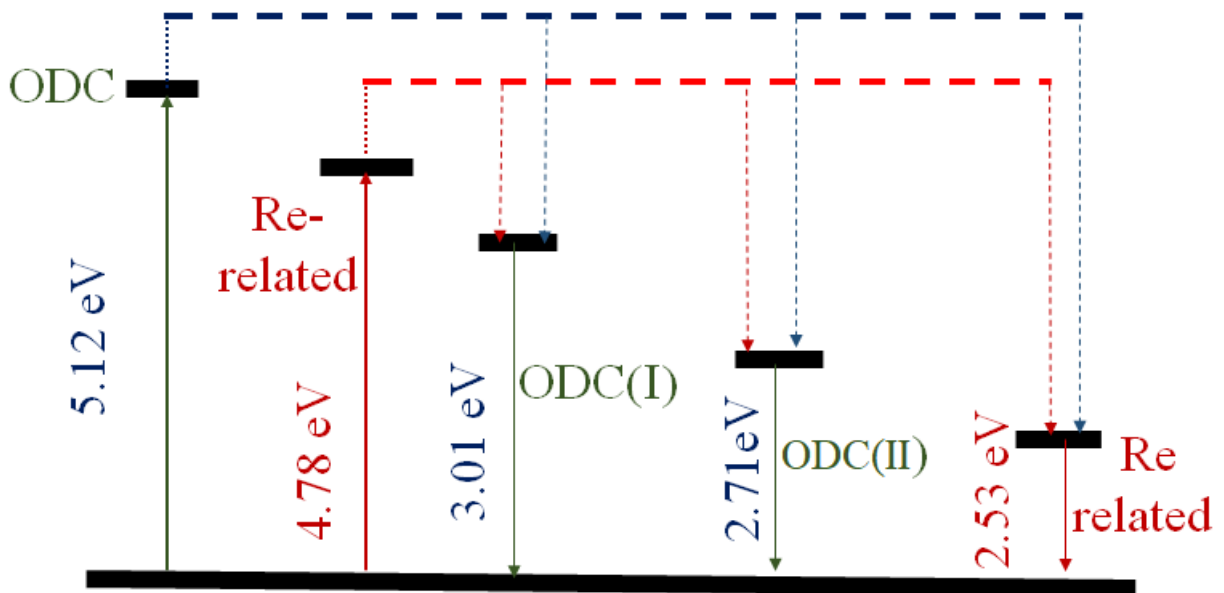
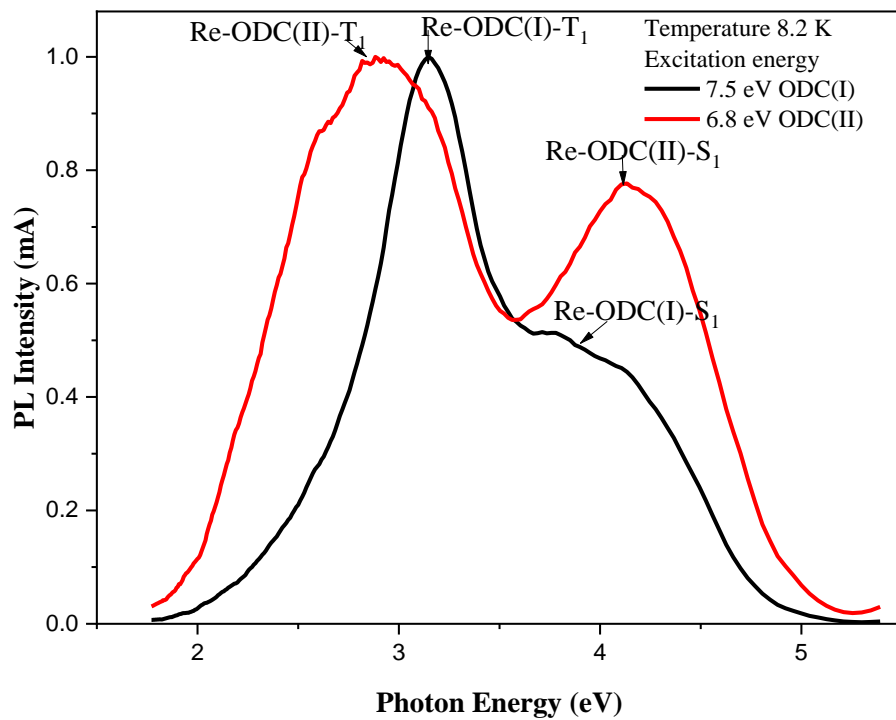


Figure 3.7 – Scheme of energy levels and electronic transitions for ODC and Re-

related centers in Re implanted SiO₂. Solid lines represent the excitation and emission optical transitions, dashed lines show the non-radiative energy transfer from the singlet excited states to the triplet emission levels [144].

3.4 Vacuum ultraviolet photoluminescence of silica glass implanted with Re ions measured at different temperatures¹

When studying different excitation methods, the photoluminescence depend on the temperature in the formation of dielectric and semiconductor nanostructures may differ significantly in shape and type, according to the results of several researches [148-152]. To determine the dominant processes of SiO₂: Re photoluminescence at different excitation energies, the PL spectra were measured at excitation energies of 7.5 and 6.8 eV and a temperature of 8.2 K (Figure 3.8). For visual comparison, the spectra are normalized to a unit of intensity.



¹ Vacuum ultraviolet photoluminescence spectra at different temperatures for silica glass implanted with Re ions were measured by Biryukov D.Yu.

Figure 3.8 – Comparison of photoluminescence peaks normalized to unit intensity at excitation energies of 7.5 and 6.8 eV and at a temperature of 8.2 K

In Figure 3.8 it can be seen that, at an excitation energy of 7.5 eV, the brightest luminescence is given by the bands at 3.2 and 3.7 eV, and at the excitation of 6.8 eV, by the bands at 2.8 and 4.1 eV. The photoluminescence spectra of SiO₂, obtained at an excitation energy of 7.5 eV, usually characteristic of Si-ODC (I) centers, of a diamagnetic monovacancy of oxygen, while the maximum of photoluminescence excitation at 6.8 eV, is attributed to the Si-ODC (II) centers, a two-coordinated silicon atom.

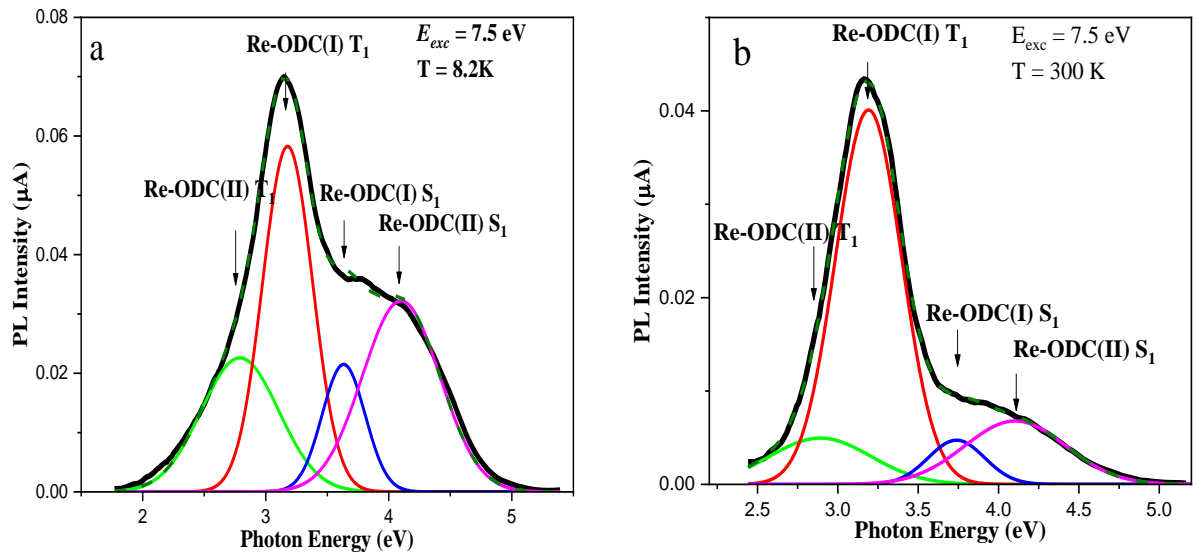


Figure 3.9 – Deconvolution of the PL spectra of KUVI silica glasses implanted with Re ions with a fluence of 10^{17} cm⁻², measured at an excitation energy of 7.5 eV and various temperatures.

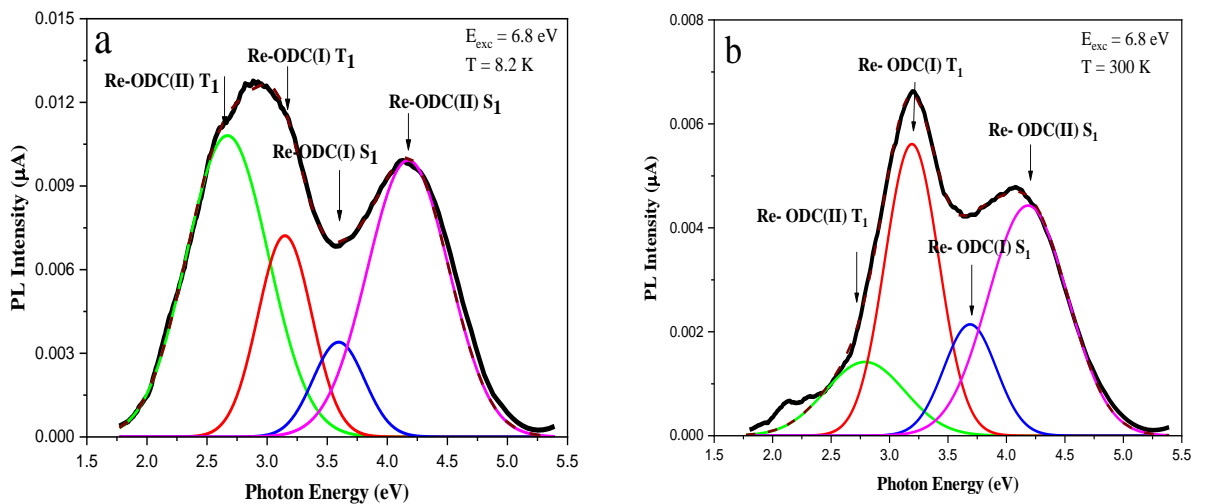


Figure 3.10 – Deconvolution of the PL spectra of KUVI silica glasses implanted with Re ions with a fluence of 10^{17} cm⁻², measured at an excitation energy of 6.8 eV and various temperatures.

Decomposition of the spectra into Gaussian components allows us to distinguish four elementary bands at 2.67, 3.17, 3.63 and 4.17 eV (Figures 3.9 and 3.10), which differ from the corresponding luminescence bands of the known Si-ODC (I) and Si-ODC (II) in pure SiO₂ (Table 3.2).

The data obtained suggest that the registered oxygen-deficient centers represent a new variant of defects modified with Re ions, which are designated as Re-ODC (I) and Re-ODC (II).

Table 3.2 – Spectral characteristics of radiative transitions in Re-ODC (I) and Re-ODC (II) centers in the temperature range 8 - 500 K

PL band	Re-ODC(II)-T ₁	Re-ODC(I)-T ₁	Re-ODC(I)-S ₁	Re-ODC(II)-S ₁
Excitation energy 7.5 eV, SiO ₂ :Re				
<i>hν, eV</i>	2.67-2.79 (2.7)	3.17-3.19 (3.1)	3.63-3.79 (4.3)	4.17-4.19 (4.4)
<i>FWHM, eV</i>	0.76	0.47-0.52	0.41	0.76
Excitation energy 6.8 eV, SiO ₂ :Re				
<i>hν, eV</i>	2.67-2.79 (2.7)	3.17-3.19 (3.1)	3.63-3.79 (4.3)	4.17-4.19 (4.4)
<i>FWHM, eV</i>	0.76	0.47-0.52	0.41	0.76

Note: The values of the radiative transition energies in the Si-ODC (I) and Si-ODC (II) centers in the unimplanted SiO₂ matrix are given in parentheses.

To trace the dynamics of photoluminescence with a change in temperature, the PL spectra were measured in the temperature range from 8.2 to 500 K with a step of 50 K with excitation energies of 7.5 (Figure 3.11) and 6.8 eV (Figure 3.12).

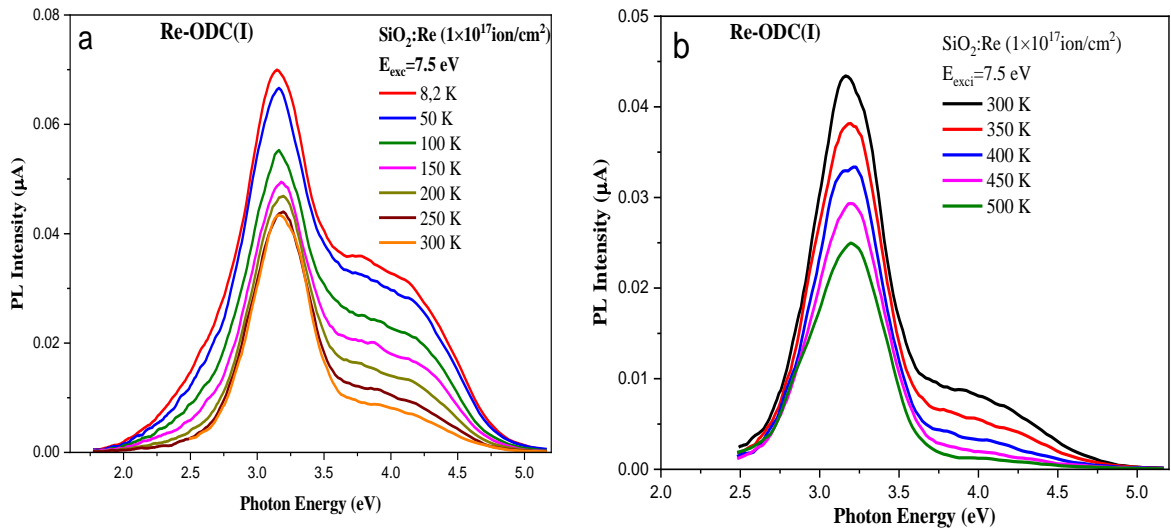


Figure 3.11 – PL spectra of KUVI Silica glasses implanted with Re ions with a fluence of 10^{17} cm^{-2} , measured at an excitation energy of 7.5 eV: (a) – in the temperature range 8.2 – 300 K, (b) – in the temperature range 300 – 500 K

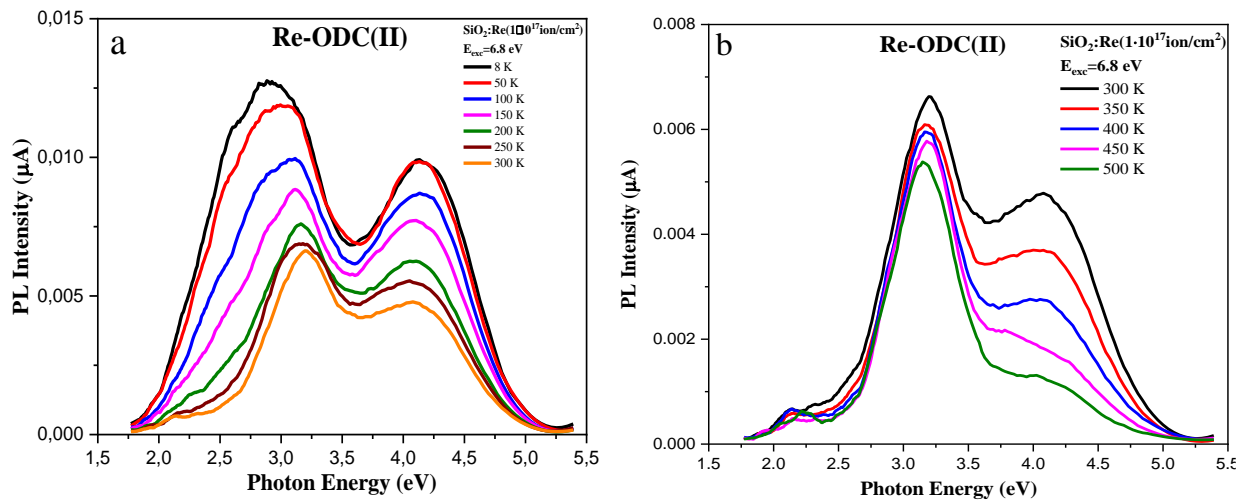


Figure 3.12 – PL spectra of KUVI Silica glasses implanted with Re ions with a fluence of 10^{17} cm^{-2} , measured at an excitation energy of 6.8 eV: (a) – in the temperature range 8.2 – 300 K, (b) – in the temperature range 300 – 500 K

To determine the optical parameters of oxygen-deficient centers, all spectra were decomposed into Gaussian components. Figure 3.9 and Figure 3.10 show the results of the Gaussian expansion at temperatures of 8.2 K and 300 K. These results show that the blue shift of the selective maximum of 2.9 - 3.2 eV observed at an excitation energy of 6.8 eV with an increase in temperature of 8 - 300 K (Figure 3.12a) is

associated with redistribution of the intensities of the luminescent bands. In particular, the 2.67 eV band is quenched much stronger than the 3.17 eV band, which leads to a blue shift of their total maximum.

At the same time, as can be seen from Figure 3.11 and Figure 3.12, with an increase in temperature from 8.2 to 500 K, the intensity of the bands decreases, and the luminescence maxima shift somewhat (Table 3.2). It should also be noted that the 3.2 eV band undergoes some broadening with increasing temperature, while the FWHM of the 2.8, 3.7, and 4.1 eV bands remains unchanged.

As noted above, the difference between the spectral parameters of the observed luminescence bands Re-ODC (I) and Re-ODC (II) from similar silicon centers Re-ODC (I) and Re-ODC (II) in unimplanted SiO₂ (Table 3.2) is associated with ion-induced modification of oxygen-deficient defects. The introduction of rhenium ions into the local environment of an oxygen vacancy and a two-coordinated silicon atom distorts the electronic subsystem of defects and displaces their excited states. A distinctive feature of modified defects is that the excitation energy practically coincides with the excitation energy of the Si-ODC, while the radiative transitions are changed. Modification of the structure of the nearest environment of defects leads to a decrease in the energy of singlet-singlet intracenter electronic transitions and an increase in the energy of singlet-triplet transitions. The levels of the triplet states are shifted to a lesser extent, and the levels of singlet states are shifted to the greatest extent.

For further analysis, the PL excitation spectra were experimentally measured at different recording energies (Figure 3.13).

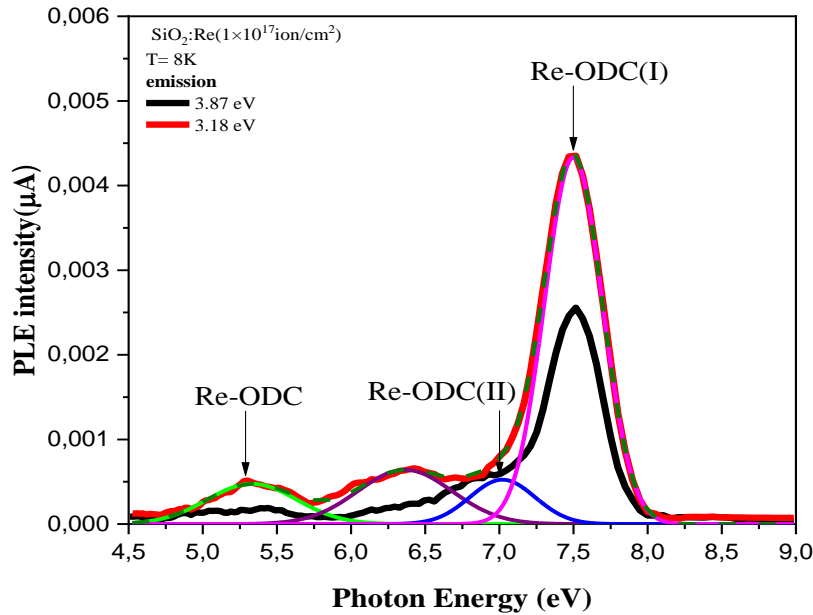


Figure 3.13 – PL excitation spectra of KUVI Silica glasses implanted with Re ions with a fluence of 10^{17} cm^{-2} , measured at a temperature of 8.2 K

The photoluminescence excitation spectra correlate well with the intensity of the PL bands 3.2 eV and 3.87 eV, confirming the oxygen-deficient type of PL centers modified with Re, which are responsible for the indicated bands. When photons with energies of 3.18 eV are detected, the 5.3 eV PL excitation band is associated with singlet-singlet transitions in $S_0 \rightarrow S_1$ in oxygen-deficient centers Re-ODC (I) and Re-ODC (II), whose transition energies are close in value. The 7 and 7.5 eV bands are associated with the $S_0 \rightarrow S_2$ transitions in Re-ODC (II) and Re-ODC (I), respectively.

3.5 Temperature dependences of vacuum ultraviolet photoluminescence of silica glass implanted with Re ions²

Investigation of the photoluminescence of modified Re-ODC (II) and Re-ODC (I) upon excitation in vacuum ultraviolet, measured at various temperatures, makes it

² Temperature dependences of vacuum ultraviolet photoluminescence of silica glass implanted with Re ions were measured by Biryukov D.Yu.

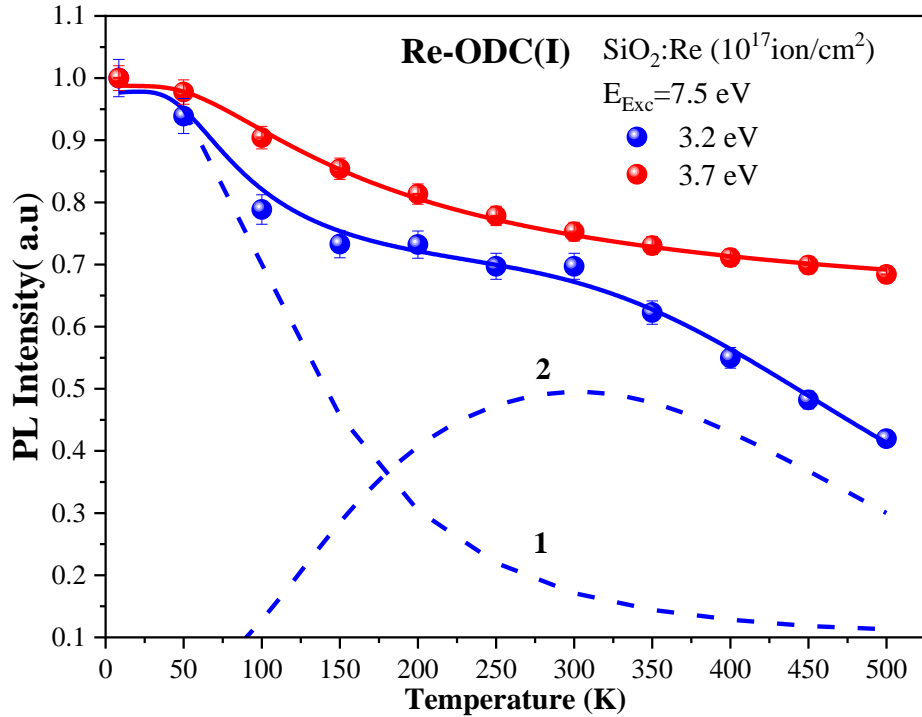


Figure 3.14 – Temperature dependences of the PL of silica glasses KUVI, measured at an excitation energy of 7.5 eV

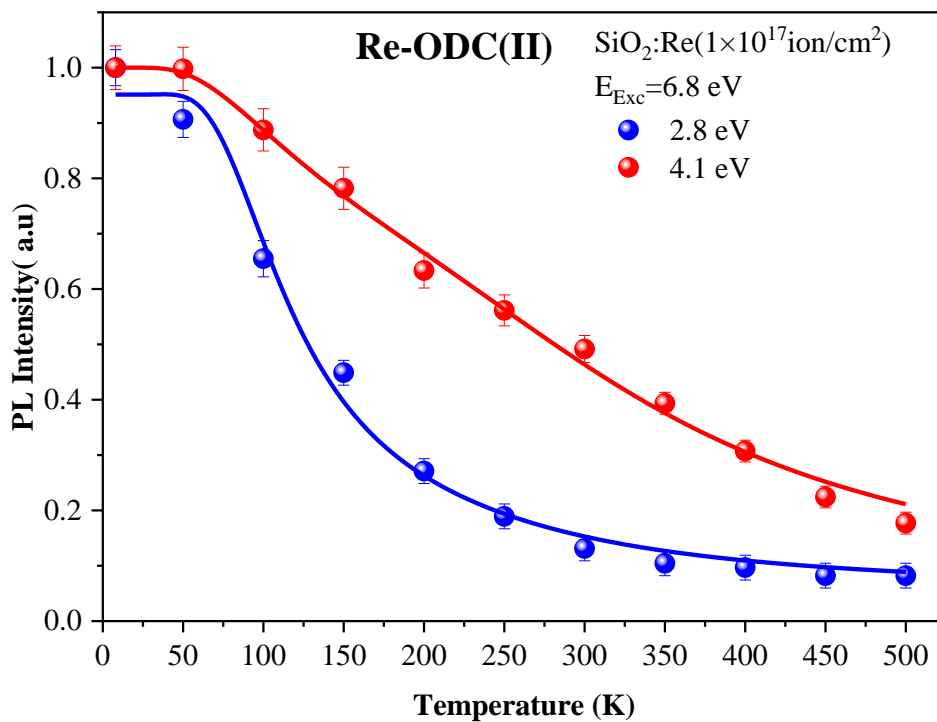


Figure 3.15 – Temperature dependences of the PL of KUVI silica glasses measured at an excitation energy of 6.8 eV

possible to study the mechanisms of excitation and relaxation of these defects. The temperature dependences for all luminescence bands are shown in Figure 3.14 and

Figure 3.15. Judging by the shape of the curves, relaxation processes with the participation of Re-ODC (II) and Re-ODC (I) obey multi-stage laws, including the presence of thermal activation stages [153], both during photoexcitation and in the course of radiative relaxation.

To describe the processes occurring during photoluminescence, we use the band diagram of electronic transitions, which is shown in Figure 3.16.

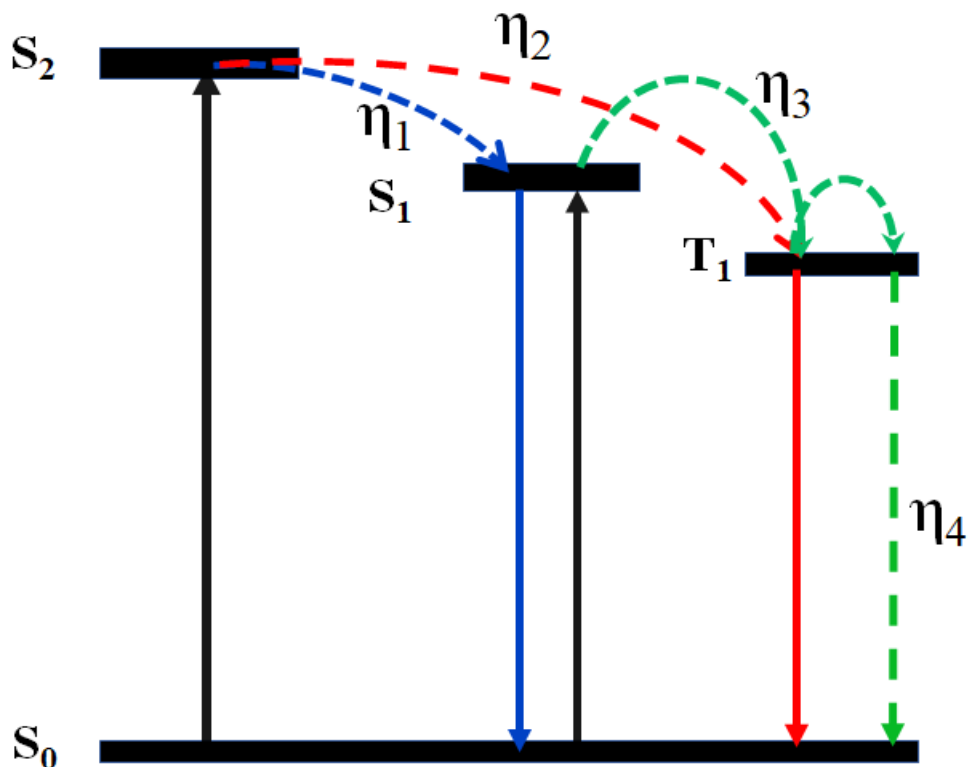


Figure 3.16 – Band diagram of Re-ODC electronic transitions in silicon dioxide implanted with rhenium ions: S_{0-2} , T_1 – energy levels; η_{1-4} – quantum efficiency of nonradiative electronic transitions

In the Figure 3.16, the dotted line denotes nonradiative (thermal) transitions, the solid line denotes radiative transitions or level filling for the case $S_0 \rightarrow S_2$. For defects of the type Re-ODC (I), the $S_0 \rightarrow S_2$ transition corresponds to an energy of 7.5 eV. The transitions $S_1 \rightarrow S_0$ and $T_1 \rightarrow S_0$ can occur with or without the emission of photons; during the radiative transition, photons are imparted with energies of 3.7 and 3.2 eV, respectively. For defects of the type ODC (II), the $S_0 \rightarrow S_2$ transition

corresponds to an energy of 6.8 eV, and the radiative transitions $S_1 \rightarrow S_0$ and $T_1 \rightarrow S_0$ are characterized by energies of 4.1 and 2.8 eV.

The dependence that describes the intensity of singlet-singlet luminescence depending on the temperature $I_s(T)$ can be described by the expression [153,154]:

$$\begin{aligned} I_s(T) &= I_0 \eta_1 \eta_3 = I_0 \eta_1 [1 + P_5/P_3 + P'_3/P_3]^{-1} = \\ &= I_0 \left\{ \left[1 + \frac{p_{03}}{P'_3} \exp\left(\frac{-E_3}{kT}\right) + \frac{p_{05}}{P'_3} \exp\left(\frac{-E_5}{kT}\right) \right] \right\}^{-1}, \end{aligned} \quad (3-1)$$

where, I_0 is the PL intensity at $T \rightarrow 0$.

where, p_{03} - frequency factor;

E_3 is the activation energy of the nonradiative transition $S_2 \rightarrow S_1$;

k is the Boltzmann constant;

T is the temperature.

Since photoluminescence is observed even at liquid helium temperatures, the factor η_1 can be neglected in formula (3-1), assuming that the energy barrier of the $S_2 \rightarrow S_1$ transition is dismissively small.

The intensity of the triplet-singlet luminescence $T_1 \rightarrow S_0$ might be described within the three-step model: [153,154]:

$$I_T(T) = I_0 \left[1 + \frac{p_{04}}{P'_4} \exp\left(\frac{-E_4}{kT}\right) \right] * \left\{ 1 + \frac{P'_3}{p_{05}} \exp\left(\frac{-E_5}{kT}\right) + \frac{p_{03}}{p_{05}} \exp\left(\frac{E_5 - E_3}{kT}\right) \right\}^{-1}. \quad (3-2)$$

It is clear from Figures 3.14, 3.15 and formulas (3-1) and (3-2) that singlet-singlet ($S_1 \rightarrow S_0$) and triplet-singlet ($T_1 \rightarrow S_0$) luminescence of ODCs under high energy excitation ($S_0 \rightarrow S_2$) are not one-stage process. Therefore, the temperature dependences of the PL of oxygen-deficient defects may have essential discrepancies with the Mott function, which is observed in Figure 3.14 and Figure 3.15. In this case, of particular interest is the dependence of the triplet-singlet luminescence ODC (I) on Figures 3.14 observed in the 3.2 eV band. The corresponding curve contains an inflection region in the temperature range above 100 K. Approximation of the experimental curve by function (3-2) shows that the triplet-singlet luminescence ODC (I) is provided by two channels of population of the T_1 radiative levels. As can

be seen from Figures 3.16, these are: 1) $S_2 \rightarrow T_1$ transitions with quantum efficiency η_2 , which begin to occur at temperatures above 50 K (Figures 3.14, curve 1); (2) $S_2 \rightarrow S_1 \rightarrow T_1$ transitions with quantum efficiencies η_1 and η_3 , which begin to occur at temperatures above 100 K. In this case, the presence of a nonzero thermal activation barrier at the $S_1 \rightarrow T_1$ transition leads to an increase in the quantum efficiency η_3 with increasing temperature and, accordingly, to an increase in the contribution of this channel for the population of the T_1 states in the temperature range 100 - 300 K.

The results of approximating experimental data using expressions (3-1) and (3-2) are presented in Table 3.3. Figures 3.14 and 3.15 show the calculated dependences $I_S(T)$ and $I_T(T)$. The approximation error does not exceed the measurement error (less than 3%).

Table 3. 3 Kinetic parameters of Re-ODC centers

Parameters	PL band			
	<i>Re-ODC(II)- T₁</i>	<i>Re-ODC(I)- T₁</i>	<i>Re-ODC(I)- S₁</i>	<i>Re-ODC(II)- S₁</i>
PL maximum ($h\nu$), eV	2,8	3,2	3,7	4,1
E_3 , meV	115,1	18,4	18,4	115,1
E_4 , meV	32,8	191,4	–	–
E_5 , meV	21,8	0,1	0,1	21,8
p_{03} / P'_3	–	–	0,1	40,0
p_{04} / P'_4	23,0	53,8	–	–
p_{05} / P'_3	1,6	0,7	1,6	1,6
p_{03} / p_{05}	50,0	15,0		

Since PL is observed even at low temperatures (8.2 K), this allows us to conclude that the energy barriers to nonradiative transitions $S_2 \rightarrow S_1$ and $S_2 \rightarrow T_1$ (Figure 3.16) do not hinder the mechanisms of radiative relaxation (have small values of E_1 and E_2). In turn, the complex nature of the quenching of the PL centers with maxima at 3.2 and 4.1 eV (Figure 3.14 and Figure 3.15) indicates the presence of at least two

or three relaxation stages, through which the energy is redistributed between the S_1 and T_1 levels, violating the Mott the nature of the temperature dependence [155].

3.6 Optical absorption edge of Re ion implanted silica glass

3.6.1 Urbach rule for Re ion implanted silica glass

The spectral dependences of the absorption coefficient in logarithmic coordinates in scale, acquired on Silica glasses before and after the ion bombardment shown in Figure 3.17. One can see that experimental curves for all samples in semi logarithmic coordinates are well approximated by direct dependences in the 7.95-8.11 eV spectral region. The optical absorption edge at higher fluences ($\Phi = 5 \times 10^{15} - 5 \times 10^{17} \text{ cm}^{-2}$) undergoes noticeable changes, becoming more sloping. It is evident that all spectral dependences have the same crossing point with coordinates $h\nu = 8.11 \text{ eV}$ and $\alpha_0 = 54 \text{ cm}^{-1}$.

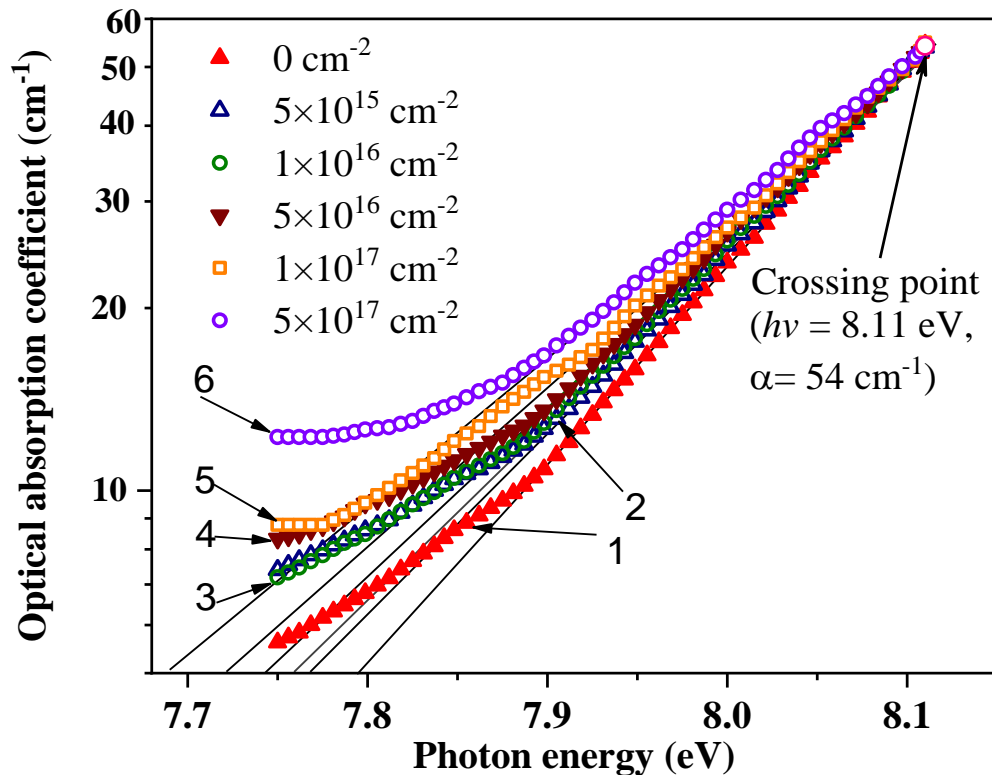


Figure 3.17 – Optical absorption edge spectra of glassy SiO_2 implanted with Re ions with different fluences. Obvious intersection point has $h\nu = 8.11 \text{ eV}$ and $\alpha_0 = 54 \text{ cm}^{-1}$ coordinate.

The results in Figure 3.17 can be analyzed through the Urbach rule, according to which spectral dependence of the optical absorption edge for various implantation doses obey the general exponential law of a general form [156-157]:

$$\alpha(h\nu, T, X) = \alpha_0 \exp\left(\frac{h\nu - E_g(T)}{E_u(T, X)}\right) \quad (3 - 3)$$

where α_0 is a constant, $E_g(T)$ is the optical gap breadth as a function of temperature, $h\nu$ is the photon energy, and $E_U(T, X)$ is the Urbach energy referred to the state density tail length at the energy band boundary and characterizing the static and dynamic disorder in a system.

3.6.2 Band gap of Re ion implanted silica glass

Absorption edge conduct of glasses under study allows to analyze the link between band gap transformations E_g^{opt} and increasing atomic structural disorder with varying implantation dose. According to the Tauc formula, the dependence of the fundamental optical absorption coefficient $\alpha(h\nu)$ is described by the following relation

$$\alpha(h\nu) = \frac{B(h\nu - E_g^{opt})^{1/n}}{h\nu} \quad (3 - 4)$$

where A is a constant, E_g^{opt} is the optical gap value, $h\nu$ is the energy of light quanta, and n is the optical transition factor determining the type of transition [158]. Optical absorption spectra plotted in Tauc coordinates (3-4) are shown in Figure 3.18.

Most appropriate approximation of the spectral dependence was obtained using expression (3-4) and $n = 2$. This value concurred well to the directly allowed interband transitions in silica glass. Extrapolated from linear of the spectrum (Figure 3.18) values of the optical gap E_g^{opt} are shown in Figure 3.19 (filled dots)

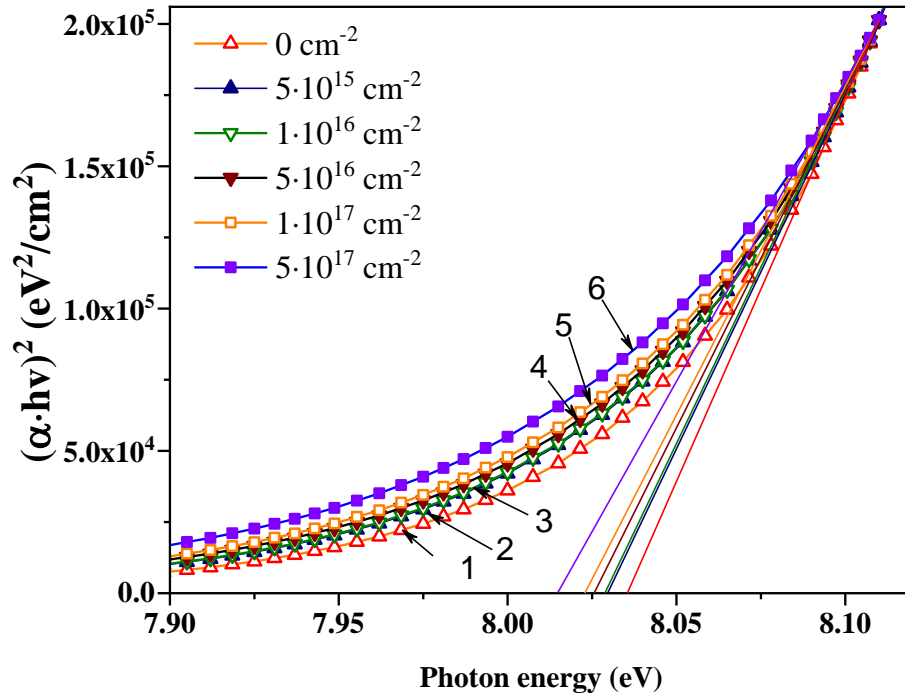


Figure 3.18 – Optical absorption edge spectra of glassy SiO₂ implanted by Re⁺ ions with various fluences plotted in Tauc coordinates.

The dose dependence of the Urbach energy E_U shown in Figure 3.19 (empty dots) is derived from the approximation results of the experimental curves using expression (1). One can see from this Figure that the Urbach energy increases super linearly on a logarithmic scale of the abscissa with an increase of fluence of Re ions. The dashed line with a constant E_U value denotes the original non-implanted sample. As seen from Figure 3.19, intimate decrease of the optical gap E_g^{opt} width occurs with increasing ion fluence and growth of Urbach energy E_U .

The effective energies of the phonons responsible for the broadening of the exponential absorption edge and participating in indirect interband optical transitions are close in magnitude. At the same time, the values the energy gaps determined for two different spectral regions of the absorption edge are somewhat different. This feature is due to the different physical meaning of the obtained values of E_g .

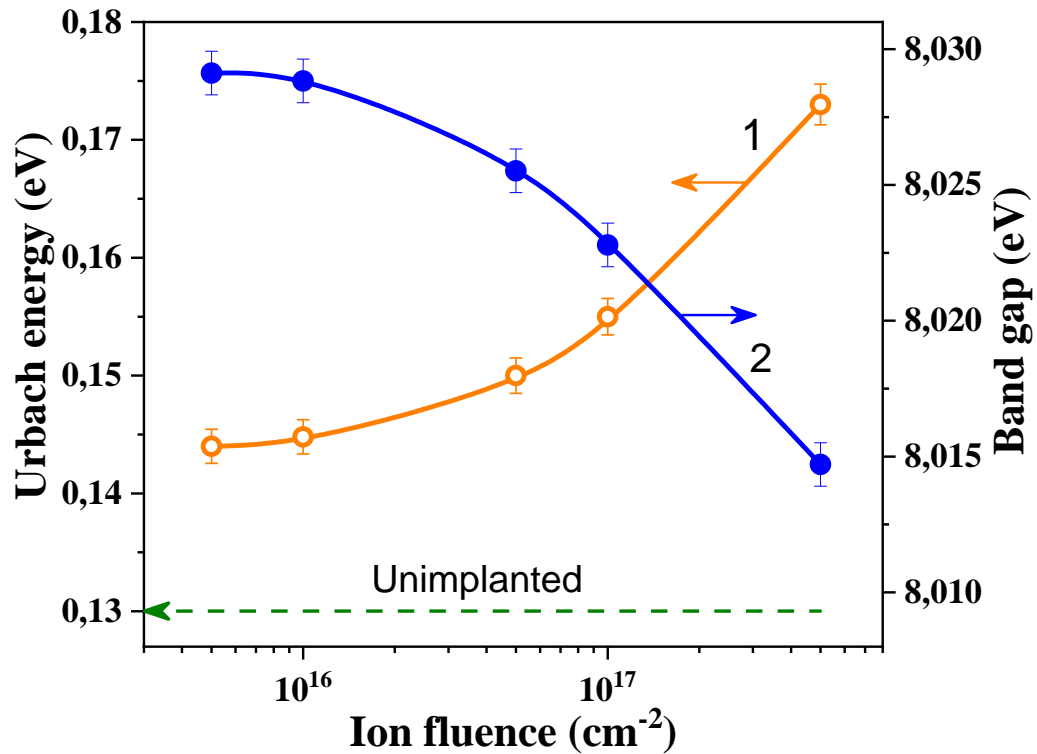


Figure 3.19 – Dependences of Urbach energy E_U (1) and band gap E_g (2) on the fluence of rhenium ions. Urbach energy of initial (non-implanted) sample is marked with a dotted arrow.

The optical gap corresponding to the region of the Urbach absorption edge is the energy gap between localized electronic states in tails of the valence and conduction bands (Figure 3.20). This value is also known as the “mobility gap” in amorphous systems with a high degree of structural disorder. The band gap values determined for the spectral region of the power-law dependence of the absorption coefficient in coordinates for direct and indirect optical transitions correspond to the energy gap between the common electronic states of the matrix.

The general structural disorder in silica glass with implanted Bi ions directly affects the features of their band-energy structure, which in turn determines the optical properties of the material.

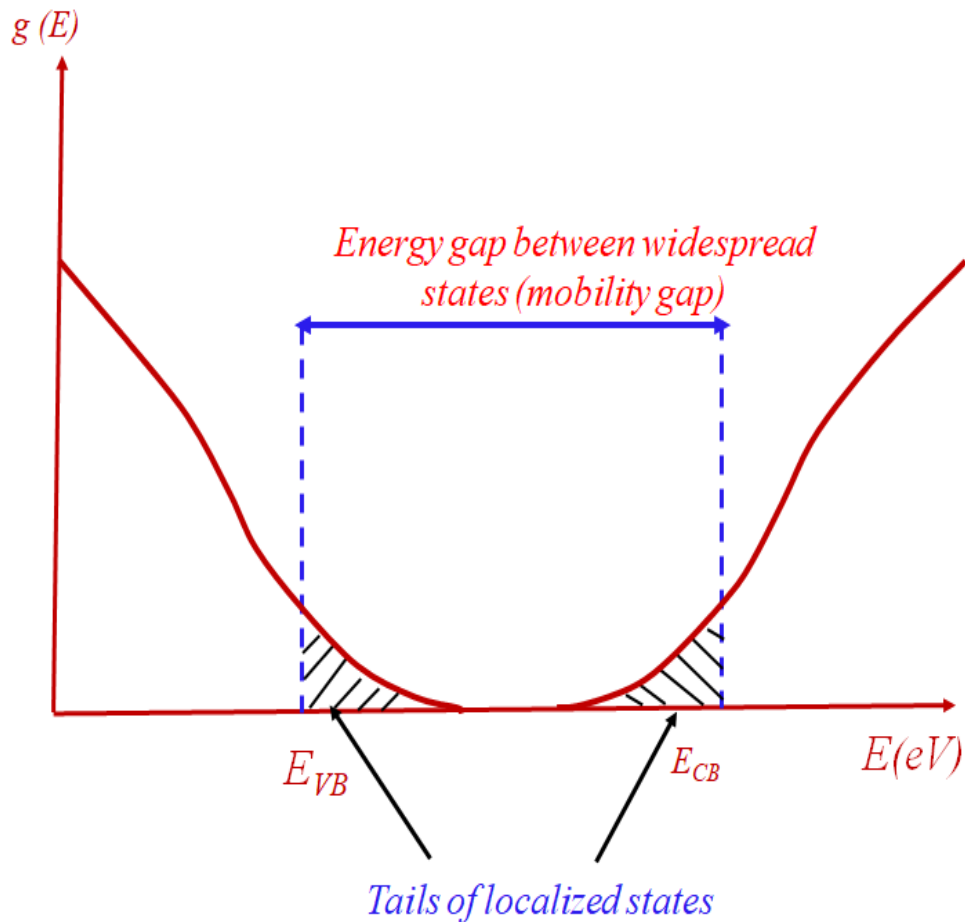


Figure 3.20 – Schematic representation of the energy band structure in disordered materials with widespread and localized electronic states

The general structural disorder in Silica glass with implanted Bi ions directly affects the features of their band-energy structure, which in turn determines the optical properties of the material.

3.6.3 Structural Disordering Regulations

According to works [159,160], The Urbach energy can be presented as a sum of static and dynamic terms of the total atomic disorder

$$E_u(T, X) = K(\langle u^2 \rangle_T + \langle u^2 \rangle_X) \quad (3 - 5)$$

Here $\langle u^2 \rangle_T$ and $\langle u^2 \rangle_X$ are the mean-square displacements of lattice atoms from their equilibrium position, which are associated with dynamic (thermal phonons) and static (“frozen” phonons) disordering, respectively. The K coefficient has units of second-order deformation potential constant. The value of the logarithmic slope of

the spectral curve E_U characterizes averaged blur of band tails, which occurs due to structural violations of atomic ordering [161]. The characteristic Urbach energy and monotonous increase of E_U parameter demonstrates Figure 3.17. The last corresponds to the radiation-induced disordering of the silica glass. approve of expressions (3-3) and (3-5), this effect indicates well that the formation of induced static disorder in the system under ion irradiation has regularities similar to dynamic disordering, so X and T parameters in eq (3-3) can be represented by the sum of static X (“frozen” phonons) and dynamic T (thermal phonons) disordering and corresponds to a certain degree of radiation-induced (quasi-dynamic) disturbances of the atomic structure.

The determined intubate behavior of dose dependences of the Urbach energy and optical gap (see Figure 3.19, curves 1 and 2) indicates correlations between these Parameters. The value of E_g can be obtained from expression (3-3), which was written through second-order deformation potential D constant as a function of different structural violations [159,161].

$$E_g(T, X) = E_g(0,0) - D(\langle u^2 \rangle_T + \langle u^2 \rangle_X) \quad (3 - 6)$$

where $E_g(0,0)$ is the gap width energy in the absence of disorder meaning zero thermal and zero frozen vibrations. So, considering expression (3-5), expression (3-6) can be rewritten as

$$E_g(T, X) = E_g(0,0) - \frac{D}{K} E_U(T, X) \quad (3 - 7)$$

This resulting expression describes the relationships between the Urbach energy E_U and the band gap width E_g under various static and dynamic disorder conditions. the latter is characterized by X and T parameters, respectively.

The relationship between the Urbach energy E_U and the optical gap E_g^{opt} shows in Figure 3.21. Assuming that E_g^{opt} is equal to the forbidden zone width $E_g(T, X)$, one can easily approximate the indicated dependence with expression (3-7). The linearity of this relationship means a constant D/K ratio for the entire range of ionic fluences,

which numerically is equal to the tangent of the slope angle of this correlation dependence. As a result of the approximation completed, the coefficient ratio is $D/K = 0.49$ (the value of $E_g(0,0) = 8.11$ eV), thus agree with the intersection point energy shown in Figure 3.17

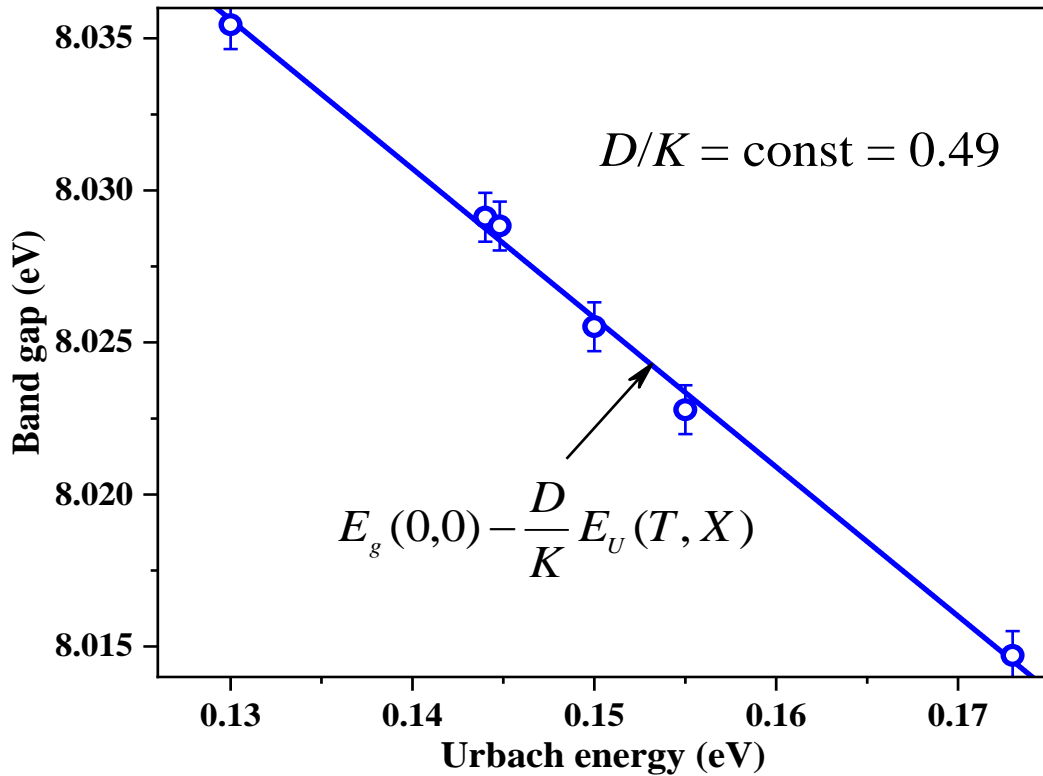


Figure 3.21 – Correlations between optical gap E_g^{opt} and the Urbach energy E_U ($E_g(0,0) = 8.11$ eV, $D/K = 0.49$).

The coefficients D and K have the meaning of the second-order deformation potential constants in the Urbach energy and optical transition energy scales, respectively. Thus, the ratio of these coefficients, determined for Silica glass implanted with rhenium ions, shows that the Urbach energy E_U is more than two times more sensitive to the degree of structural disorder than the band gap E_g .

3.7 Conclusion

1. The main regularities of defect formation and disordering of the atomic structure during the implantation of KUVI Silica glasses with various fluences of Re activator ions with an energy of 30 keV have been established.

2. After pulsed implantation of SiO_2 glass with Re ions, the matrix is damaged and intrinsic defects appear: E'-centers, ODC (I), ODC (II).
3. Along with intrinsic defects, centers modified by activator ions also arise. These include oxygen monovacancies ODC (I) and divacancies ODC (II), in the local environment of which Re ions are located.
4. Modification of ODC by impurity Re ions leads to a decrease in the energy of singlet-singlet intracenter electronic transitions and an increase in the energy of singlet-triplet transitions. The levels of singlet states are shifted to a greater extent. In the smaller - triplet.
5. Implantation with Re ions also creates centers of a new type (Re-related) associated with implanted ions, which are not registered in the initial pure SiO_2 .
6. It was found that the temperature dependences for all luminescence bands excited in the vacuum ultraviolet are described by multistage thermoactivation laws. This indicates the presence of thermal activation stages both in the process of photoexcitation and in the mechanism of nonradiative relaxation.
7. In the temperature dependence of the triplet luminescence ODC (I) upon excitation of the S_2 state, a stage of the PL intensity flaring up with an increase in temperature was found due to the influx of additional excitations from the S_1 state.
8. The fundamental absorption edge of Silica glass implanted with Re ions obeys the "crystal-like" Urbach rule, the parameters of which reflect the degree of structural disorder.
9. Ion implantation increases the degree of structural disorder and decreases the band gap. The proportional change in the Urbach energy and the optical gap shows that these are optical parameters of the material, reflecting the same process - lengthening of the tails of localized states.

CHAPTER 4. OPTICAL AND LUMINESCENCE PROPERTIES OF OXYGEN-DEFICIENT CENTERS IN KI GLASS IMPLANTED WITH 80 KEV RE IONS

4.1 SRIM simulation for 80 keV Re ions implanted SiO₂

The samples of KI-type (I) silica glass were used as hosts for ion implantation. Glass of this type has a high throughput in the visible and infrared regions, as well as high radiation resistance and a low concentration of impurities. [130,162]

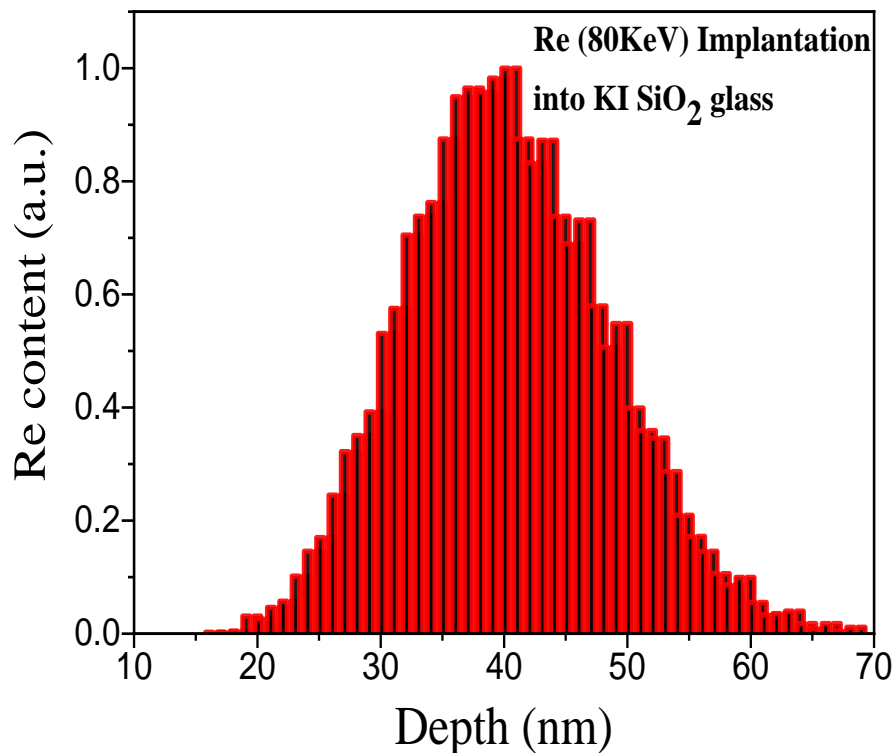


Figure 4.1 – SRIM simulation of the penetration depths for 80 keV Re-ions in KI SiO₂ glass. [144]

The depth of the Re ion implant in KI SiO₂ glass with an emission energy of 80 keV was evaluated using the SRIM [134] (termination and ion range) Release) software. The results showed that the introduction of rhenium ions into the surface layer of SiO₂ occurs in the depth range of 20-70 nm. The maximum distribution of implanted ions corresponds to a depth of 40 nm (Figure 4.1).

4.2 Optical absorption of silica glass implanted with Re-ions 80 keV

The Optical absorption spectra of maiden and Re-embedded glasses were recorded on a Perkin Elmer Lambda 35 spectrophotometer. The concentrations of light-absorbing defect centers in SiO₂ framed because of ions implantation, were determined using the Smakula-Dexter formula. [163]

$$N(n^2 + 2)f = 0.87 \times 10^{17} n \alpha_0 \Delta E \quad (4-1)$$

where n is the refractive index for SiO₂ in the spectral region of absorption band (1.53 for the Silica glass) [164,165],

α_0 is the absorption coefficient at the band's maximum,

ΔE is the FWHM of band,

f is the oscillator strength of optical transition.

Since the process of ion implantation was carried out in a pulsed position, point defects associated with centers of silicon oxygen defect center arise not only in the ion-modified layer, but also over the entire depth of the sample due to the shock wave mechanism. Given this feature, we calculated the average concentration of centers over the entire thickness of the samples (see Table 4.1)

Table 4.1 – Concentrations (cm⁻³) of E'-centers and oxygen-deficient centers (ODC) in Re implanted SiO₂ before and after thermal annealing.

Center	Ion Fluence, cm ⁻²		Ion Fluence, cm ⁻²		Ion Fluence, cm ⁻²	
	Before annealing	After annealing	Before annealing	After annealing	Before annealing	After annealing
	5×10 ¹⁶		1×10 ¹⁷		2.5×10 ¹⁷	
E'	1.2×10 ¹⁷	3.2×10 ¹⁶	1.6×10 ¹⁷	5.3×10 ¹⁶	4.1×10 ¹⁷	7.2×10 ¹⁶
Si-ODC	4.1×10 ¹⁵	8.5×10 ¹⁵	6.1×10 ¹⁵	1.4×10 ¹⁶	1.2×10 ¹⁶	2.1×10 ¹⁶
Re-ODC	6.3×10 ¹⁵	11.2×10 ¹⁵	9.1×10 ¹⁵ -	1.8×10 ¹⁶	1.6×10 ¹⁶	2.7×10 ¹⁶

Note: For annealed samples, the concentrations of Si-ODC and Re-ODC are listed, which correspond to two possible scenarios of the appearance of an absorption band at 5.15 eV.

Figure 4.2 (a) and (b) explain the absorption spectra of primary and implanted SiO_2 . Ion-beam irradiation of a silica matrix degrades its optical transparency in the spectral region close to ultraviolet rays. A significant increase in the absorption coefficient at 4.2-6 eV is due to the formation of optically active internal defects in the SiO_2 host after ion irradiation. Silicon dioxide is characterized by many point defects, which are formed as a result of interaction with accelerated particles and high-energy radiation [89,137,139,166].

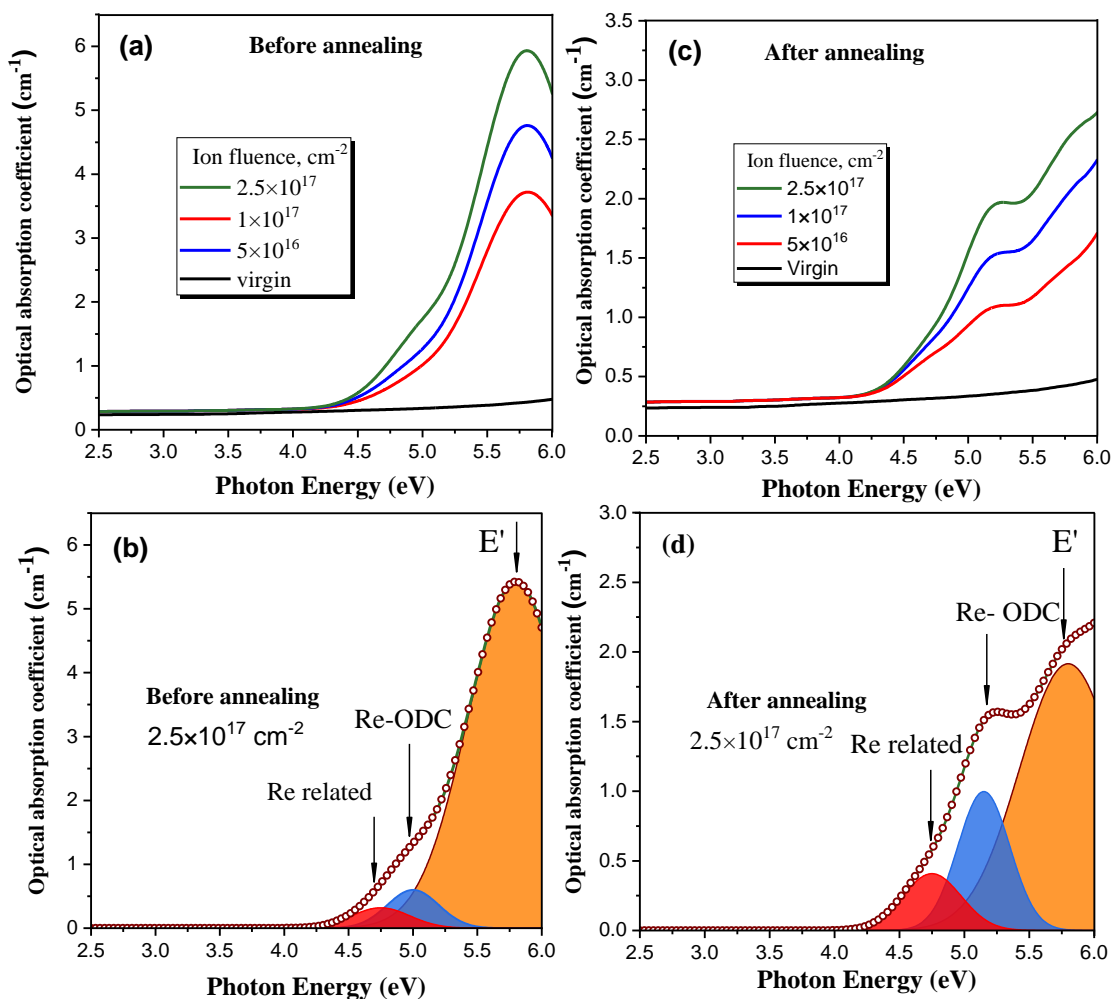


Figure 4.2 – Absorption spectra of SiO_2 implanted with Re ions at different fluencies before (a, b) and after (c, d) thermal annealing. Arrows indicate absorption bands corresponding to the optical transitions in defect centers induced by ion irradiation and subsequent thermal treatment.

Many of these defects are directly involved in the absorption and luminosity processes and can be determined by the position and half the width of the corresponding ranges in the spectra. The absorption spectra of replanted silica are not significant and consist of several separate peaks. In order to classify these signals and associate them with the indicated centers, we performed Gaussian deconvolution of the difference absorption spectra (Figure 4.2 (b)).

The peak at 5.8 eV (FWHM = 0.75 eV) gives the main contribution in the optical absorption of as-implanted SiO₂. This absorption band corresponds to the so-called E'-center representing the three-coordinated silicon atom with an unpaired electron on a dangling bond and often denoted by $\equiv\text{Si}^*$. A feature of this defect is paramagnetic resonance properties and the non-attendance of any photoluminescence signals [48,58]. There is a less intense absorption peak in the spectral area of 5 eV. This band is related with the twofold coordinated silicon (=Si:), so called ODC(II) [48,58].

The determination of the third absorption range at 4.75 eV (FWHM = 0.45 eV) turned out to be more complicated, and several hypotheses regarding its nature can be made. Education E'-centers are often accompanied by the appearance of other free defects. The breaking of the Si – O bond can occur in the primary silica network $\equiv\text{Si-O-Si}\equiv$, forming the center E' and the non-bridging oxygen hole center $\equiv\text{Si-O}\cdot$ (NBOHC), which has an absorption range at 4.8 eV. FWHM = 1.1 eV) [58,167]. In addition, there is a possible point defect arising together with the E' center, which is a light peroxy radical at 4.8 eV (FWHM = 0.8 eV) [58, 81, 168]. Despite the fact that the absorption transmission bands at these centers are at least twice the bandwidth observed in our experiment, they cannot be completely excluded at this point. Both NBOHC and POR are magnetically parallel and can be determined using EPR spectroscopy. Signals from NBOHC or POR were not recorded in the EPR spectra of the samples, but only the signal from the center E'. This allows us to make another assumption about the origin of the absorption range of 4.8 eV associated with the presence of the so-called bound ODC Re. It represents a local structural deformation

of the hypoxic type with Re ions in the near medium. We noted similar centers associated with the implanted ion in our work attributed to cultured Silica glass with Ge, Sn, and Pb ions [169-171]. The final conclusion about the nature of the absorption of 4.8 V can be made after analyzing the PL measurements described in the following sections

The concentrations of optically active centers were calculated using the Smakula – Dexter equation are listed in Table 4.1. As can be seen, the number of electronic centers and ODC centers has inverse dynamics. After the concentration of thermal annealing of E'-centers decreases, the number of ODC increases. Thermal processing of a structurally imperfect matrix usually leads to a partial elimination of network disturbances. In our case, we note the opposite effect, that is, an increase in the concentration of point defects associated with hypoxia. The reason for this effect may be due to the interaction of various types of defects and their transformation activated by thermal annealing

Cultivated samples become more transparent in the spectral region close to UV after thermal annealing; cultivated samples become more transparent in the spectral region close to UV (Figure 4.2(c) and (d)). The absorption spectra consist of the same sample ranges before annealing with an additional contribution in the range of 7 eV, which corresponds to the high-energy optical transfer $S_0 \rightarrow S_2$ in coordinated silicon ODC (II). The half-widths of the absorption bands remain constant after annealing, but changes in their additional intensity indicate a change in the focus of the optical centers [172]. It should be noted that the absorption range at 5 V for transplanted samples is transferred to the high energy region (Figure. 4.2 (c) and (d)). The absorption spectra consist of the same ranges of samples before annealing with an additional contribution in the range of 7 eV, which corresponds to the high-energy optical transfer $S_0 \rightarrow S_2$ in coordinated silicon (2). The half-widths of the absorption bands remain constant after annealing, but changes in their additional intensity indicate a change in the focus of the optical centers. It should be noted that the absorption range at 5 V for transplanted samples moves to the high-energy region.

At 5.15 eV. The debate over the 5.15 eV optical absorption range has been very difficult and controversial for a long time. On the one hand, this absorption range is associated with oxygen vacancies of neutral silicon ($\equiv\text{Si} - \text{Si} \equiv$), also called ODC (I) [67, 173-175]. On the other hand, many scientific groups attribute this band to the focus of hypoxia associated with Ge (bi-coordinated germanium) [78,176] Although high-purity Silica glass was studied in this work, we cannot completely exclude the possible presence of very low amounts of Ge impurities. Therefore, both scenarios can take place for the nature of the absorption range of 5.15 eV

We found two possible scenarios for the initial absorption range of 5.15 eV: Re-ODC (I) and Re-ODC (II). For the first scenario, after thermal annealing, the following defect transformation process can take place: two centers E' , each of which contains one unpaired electron, are combined into one oxygen vacancy according to the scheme $\equiv\text{Si}\cdot + \cdot\text{Si}\equiv \rightarrow \equiv\text{Si} - \text{Si}\equiv$. For the second scenario E' in the centers participates in the formation of ODC associated with Si by switching bonds as follows, for example: $\equiv\text{Si}\cdot + \cdot\text{Si}\equiv \rightarrow \equiv\text{Si} - \text{Si}\equiv$ In both cases, two parallel processes occur during heat treatment.

the transformation (1) $E' \rightarrow \text{ODC}$; (2) Annealing defects and reducing the structure of the host. Both operations equally affect the change in the number of centers E' , which led to its decrease. In the case of ODC, on the one hand, its concentration increases due to the conversion $E' \rightarrow \text{ODC}$ (I), but, on the other hand, thermoplastics leads to a decrease in the number of structural defects. Thus, these two processes are competitive, and the $E' \rightarrow \text{ODC}$ (I) conversion prevails over thermal annealing, as evidenced by the increased concentration of ODC after heat treatment (see Table 4.1)

Noting that the integral density of the absorption ranges at 4.8 eV, the nature of which at this stage remains uncertain, also increases after thermal annealing. Such similar behavior, such as ODC, can be considered the first argument in favor of the corresponding ODC. However, this fact is not enough, and a more reliable conclusion can be drawn about the origin of this range based on PL data. Noting that the

integral density of the absorption ranges at 4.8 eV, the nature of which at this stage remains undetermined, also increases after thermal annealing. Such similar behavior, such as ODC, can be considered the first argument in favor of the corresponding ODC. However, this fact is not enough, and a more reliable conclusion can be drawn about the origin of this range based on PL data.

4.3 Electron paramagnetic resonance (EPR) of E'-centers

Due to the special role the EPR techniques play in finding the defect structure on the atomic scale, the most common task of this kind is establishing the EPR–optical correlations. However, the number of reported unambiguous EPR–optical correlations for defects in glasses is small. EPR spectra are independent of the irradiation type, but they differ depending on the preparation conditions of the samples. In all cases the EPR signal of axial symmetry with $g_{||} = 2.00656 \pm 0.00003$ and $g_{\perp} = 2.00584 \pm 0.00004$ [177,178] components is detected (Figure 4.3), which was interpreted as paramagnetic absorption of Re ions, a more complicated EPR-signal is registered for SiO₂:Re. the main EPR defect is the Centre resulting from an unpaired electron spin highly localized in a sp³ hybrid orbital of a single threefold-coordinated silicon atom [179,180] This paramagnetic center is the best characterized intrinsic defect in SiO₂: Re, and exhibits a long spin lattice relaxation time; this feature makes the E'-center detectable at very low microwave powers, but after annealing there are not signal, and defect center.

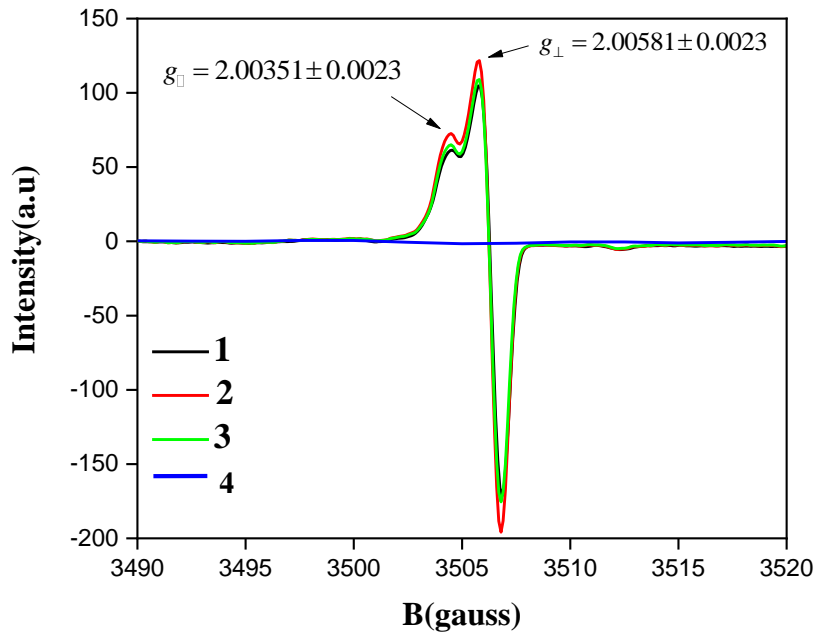


Figure. 4.3 – EPR spectra of SiO₂: Re at room temperature with: 1 – at dose 5×10^{16} ion/cm²; 2 – at dose 1×10^{17} ion/cm²; 3, 4 – at dose 2.5×10^{17} ion/cm² before annealing (3) and after annealing (4).

4.4 Photoluminescence spectra upon excitation in the near ultraviolet

The PL and excitation (PLE) spectra of Re implanted SiO₂ are shown in Figure.4.4. At 5 eV excitation, the luminescence spectrum is represented by a superposition of three bands with maxima at 3.2 eV (FWHM = 0.4 eV), 2.9 eV (FWHM = 0.3 eV) and 2.8 eV (FWHM = 0.5 eV). The 2.8 eV PL band is characteristic of triplet-singlet T₁ → S₀ transition in Re-ODC(II). The nature of 3.2 eV was a long-time subject for dispute. Concept proposed by Skuja states that this band is related with Ge-impurity center [78]. This point of view is supported by a number of scientific groups [176,181,182].

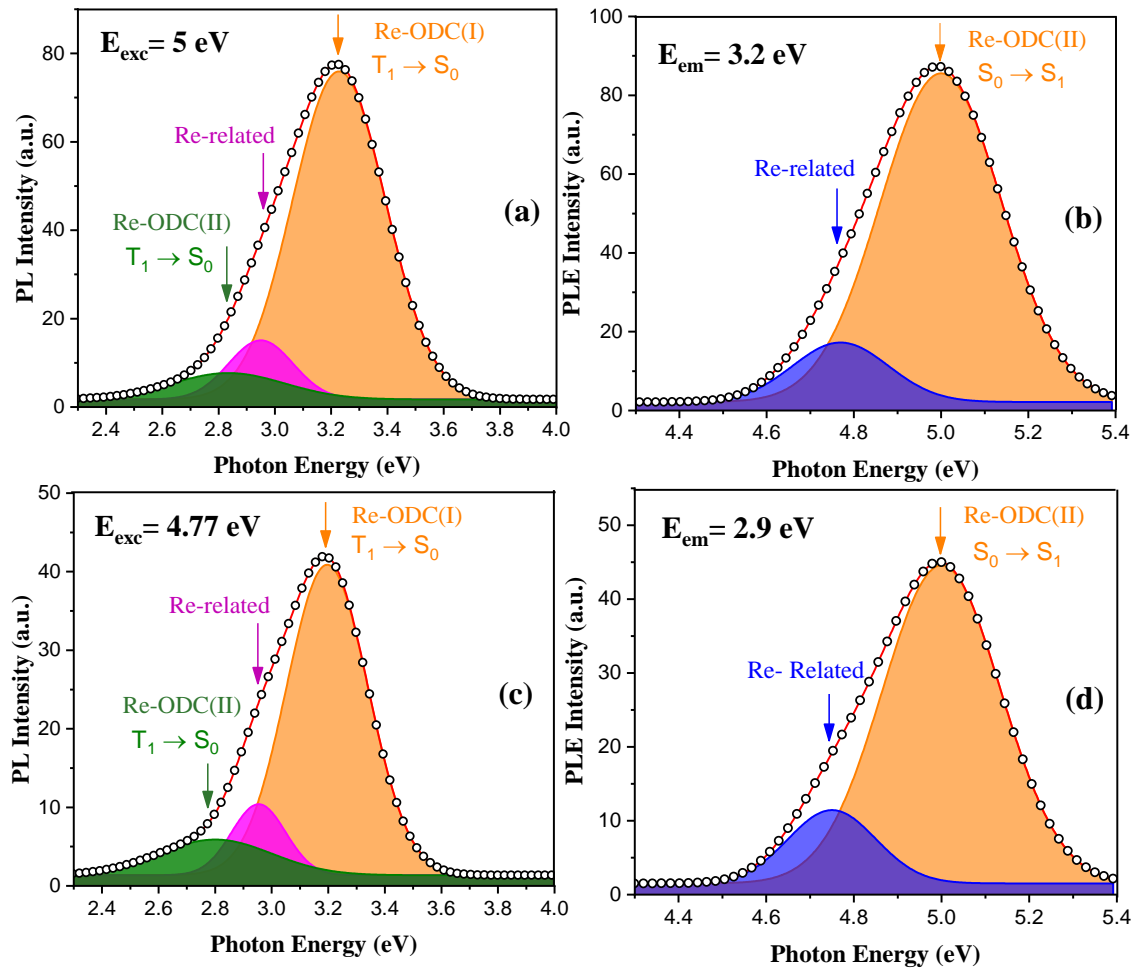


Figure. 4.4 – PL and excitation spectra of SiO_2 implanted with Re ions at $2.5 \times 10^{17} \text{ cm}^{-2}$ Fluence. Arrow indicate the optical transitions in modified oxygen deficient centers Re-ODC(I) and Re-ODC(II), and Re-related center.

At the same time, the 3.2 eV emission was clearly observed in high-pure silica glasses under the excitation of 5 eV [67,175]. Tohmon et al. reported that the relatively strong emission at 3.16 eV under excitation of 5 eV belongs to the ODC(I) and corresponds to the triplet-singlet $T_1 \rightarrow S_0$ transition [3, 183]. Also, in our earlier work we observed the similar PL signals from ODCs in irradiated and ion-implanted silica glasses [184,185]. By analogy with the interpretation of the nature of the 5.15 eV absorption band, we suppose there are two possible assignments for the 3.2 eV PL band: Re-ODC(I) and Re-ODC(II). The excitation bands in the region of 5 eV

and correspond to the population of the S_1 excited states of ODC. There are three pathways for deactivating the S_1 state:

- (1) radiative singlet-singlet $S_1 \rightarrow S_0$ transition.
- (2) energy transfer to the triplet state $S_1 \rightarrow T_1$;
- (3) nonradiative $S_1 \rightarrow S_0$ relaxation via phonons.

The singlet-singlet radiative transition is spin-allowed, so the lifetime of the singlet excitation is very short (several nanoseconds) [46, 58, 167]. The triplet-singlet radiative transition is spin-forbidden and has a much longer lifetime ($\sim 100 \mu\text{s}$) [3, 67]. The $S_1 \rightarrow T_1$ energy transfer is thermally-activated with the activation energy of about 0.1 eV [167]. For this reason, with an increase in temperature the intensity of triplet-singlet PL is constantly increasing. At room temperature, the $S_1 \rightarrow S_0$ transition is almost quenched and PL spectra contains only triplet-singlet transitions, as we also observed in this work. Thus, the depopulation of the S_1 singlet excited state of ODCs occurs via energy transfer to the triplet T_1 excited state with the consequence radiative emission $T_1 \rightarrow S_0$.

The PL band at 2.9 eV cannot be assigned to the silicon ODCs, since the position of peak is shifted from the Re-ODC(I) and Re-ODC(II) PL bands. The PLE spectra of 2.9 eV and 3.2 eV ($T_1 \rightarrow S_0$ for ODC) bands are qualitatively similar and contain two peaks with maxima at 4.77 eV (FWHM = 0.25 eV) and 5 eV (FWHM = 0.3 eV). The 5 eV PLE band is not surprising and corresponds to the excitation of the Si-ODC(II) singlet S_1 state. As for the 4.77 eV signal, we observed a band with the same maximum in the absorption spectra and put forward several hypotheses about its origin (along which NBOHC, POR, Re-related ODC) [58, 167]. This band we will further refer to as Re-related.

At both 4.77 and 5 eV excitations, there are all PL bands (both Re-ODC(II) and Re-related), but the emission of Re-ODC(II) dominates regardless of the excitation energy. When the excitation changes from 5 eV (transition in Si-ODC(II)) to 4.77 eV (transition in ODC/Re), a change in the ratio of the integrated PL intensities $I_{\text{Re-ODC}}/I_{\text{Re-related}}$ observed in favor of the Re-related (Table 4.2). Such features indicate

the effective mutual energy transfer between two types of ODCs: Re-ODC Re-related. After thermal annealing, the PL intensity increases by more than three times (Figure 4.5) and $I_{\text{Re-ODC}}/I_{\text{Re-related}}$ ratio decreases at both 4.77 and 5 eV excitations.

Table 4.2 – The ratio of integrated PL intensity of Re- ODC $I_{\text{Re-ODC}}/I_{\text{Re-related}}$ at different excitations before and after thermal annealing of SiO₂ implanted with Re ions.

Fluence, cm ⁻²	Before annealing		After annealing	
	E _{exc} =5 eV	E _{exc} =4.7 eV	E _{exc} =5 eV	E _{exc} =4.7 eV
5×10 ¹⁶	6.4	5.2	5.8	4.5
1×10 ¹⁷	7.5	6.3	6.4	5.3
2.5×10 ¹⁷	8.7	7.2	7.4	5.8

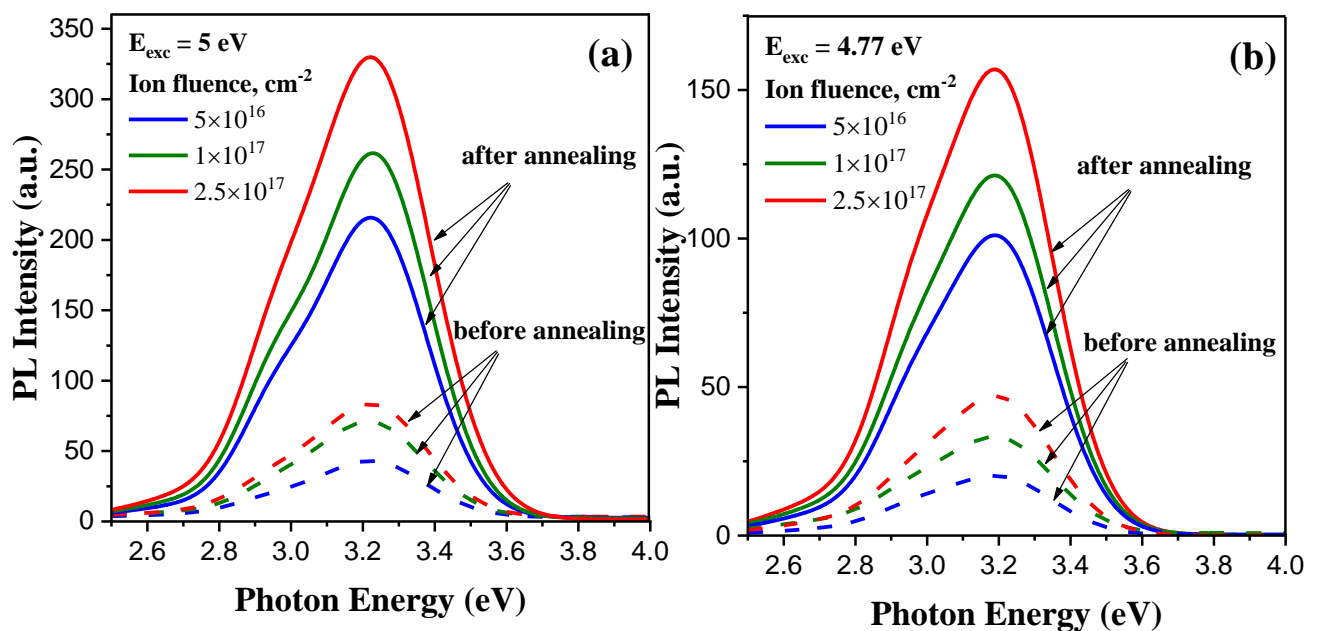


Figure 4.5 – The PL intensity of Re implanted SiO₂ depending on the ion fluence under thermal annealing at excitations of 5 eV (a) and 4.77 eV (b).

The increase in the PL intensity in annealed samples is due to the increase in the concentration of emission centers, as was determined from the absorption measurements (Table 4.1). Wherein, the larger the ion Fluence, the more pronounced the PL band assigned to the Re-related for annealed Re implanted SiO₂ in comparison with the as implanted samples (Table 4.2). We assume that thermal annealing activates the diffusion of Re ions into the bulk of the material, which leads to an increase in the number of Re-modified optically-active centers.

4.5 The decay of photoluminescence of ODC upon excitation in the near ultraviolet

Figure 4.6. show that the PL decay curves for various optical centers in SiO₂ implanted with Re ions at a Fluence of $2.5 \times 10^{17} \text{ cm}^{-2}$. The PL lifetimes of Re-ODCs at excitation of 5 eV are close to each other have the order of one hundred microseconds (Table 4.3). the SiO₂ with Re ion implanted is increase in PL lifetime for all emission centers after Thermal annealing. This is due to the decrease in the number of quenching centers (PL killers) providing channels for nonradiative relaxations, since thermal treatment partially remove the structural damage caused by ion implantation. The PL lifetimes are almost independent of the ion fluence and vary by only a few microseconds, which is within the limits of error.

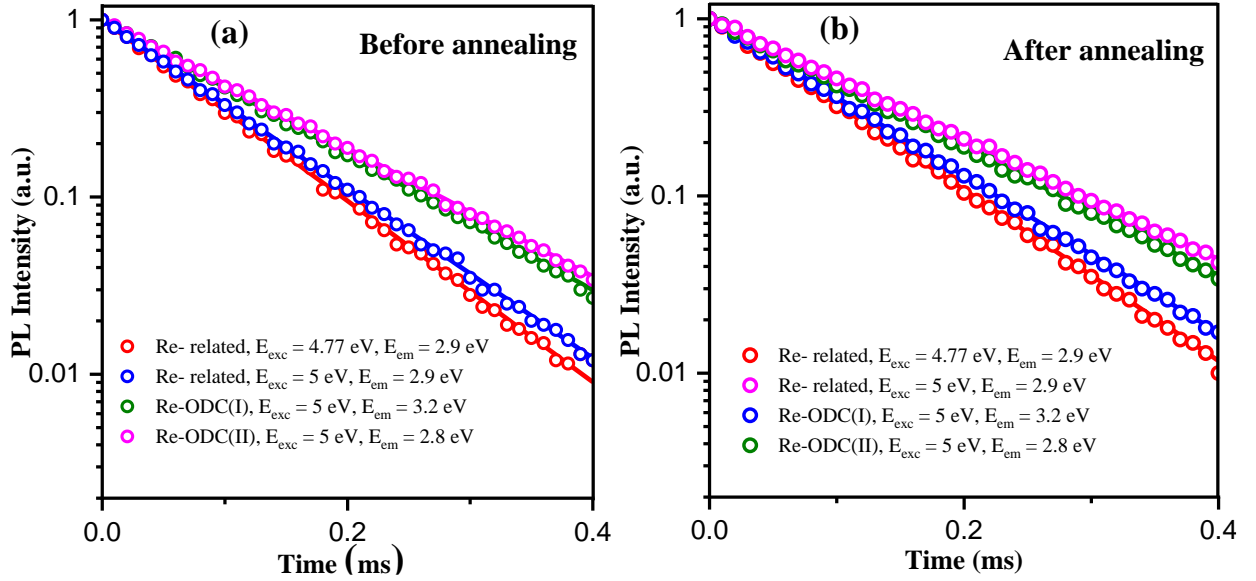


Figure 4.6 – PL decay curves of Re-related and Re-ODC in Re implanted ($2.5 \times 10^{17} \text{ cm}^{-2}$) SiO_2 before (a) and after (b) thermal annealing.

Table 4.3 – PL decay times (μs) of different emission centers in Re implanted ($2.5 \times 10^{17} \text{ cm}^{-2}$) SiO_2 before and after thermal annealing

Center	Before annealing		After annealing	
Re-ODC(I) $E_{\text{em}}=3.2\text{eV}$, $E_{\text{exc}}=5\text{eV}$	114 \pm 2		120 \pm 2	
Re-ODC(II) $E_{\text{em}}=2.8\text{eV}$, $E_{\text{exc}}=5\text{eV}$	120 \pm 2		128 \pm 2	
Re- related $E_{\text{em}}=2.9$	85 \pm 2 ($E_{\text{exc}}=4.77$)	91 \pm 2 ($E_{\text{exc}}=5\text{eV}$)	90 \pm 2 ($E_{\text{exc}}=4.77\text{eV}$)	98 \pm 2 ($E_{\text{exc}}=5\text{eV}$)

The dynamic (PL kinetic) and the Static (maxima and FWHM of PL and PLE bands) optical characteristics of Re- related indicate that emission in this center is most likely related to a radiative triplet-singlet transition $T_1 \rightarrow S_0$ by analogy with Si-ODCs. Silicon ODCs and Re-modified ODC differ in the system of energy levels and the lifetime of the PL. Triplet-singlet transition for Re-ODC is spin-prohibited.

that leads to the long-lived PL. The PL of Re-related is a bit faster, indicating a partial reducing the forbiddance of $T_1 \rightarrow S_0$ optical transition for Re-modified center.

4.6 Scheme of electronic transitions for silica glass with implanted Re ions

Scheme of electronic transitions for Re-ODCs and Re-related is shown in (Figure 4.7.) At both excitations of Re-ODC(II) (5 eV) and Re-related (4.77 eV) there are three

pathways followed by photons emission: (1) energy transfer to the triplet state of Si-ODC(II); (2) energy transfer to the triplet state of Re-ODC(I)/Re-ODC(II); (3) energy transfer to the triplet state of Re-related

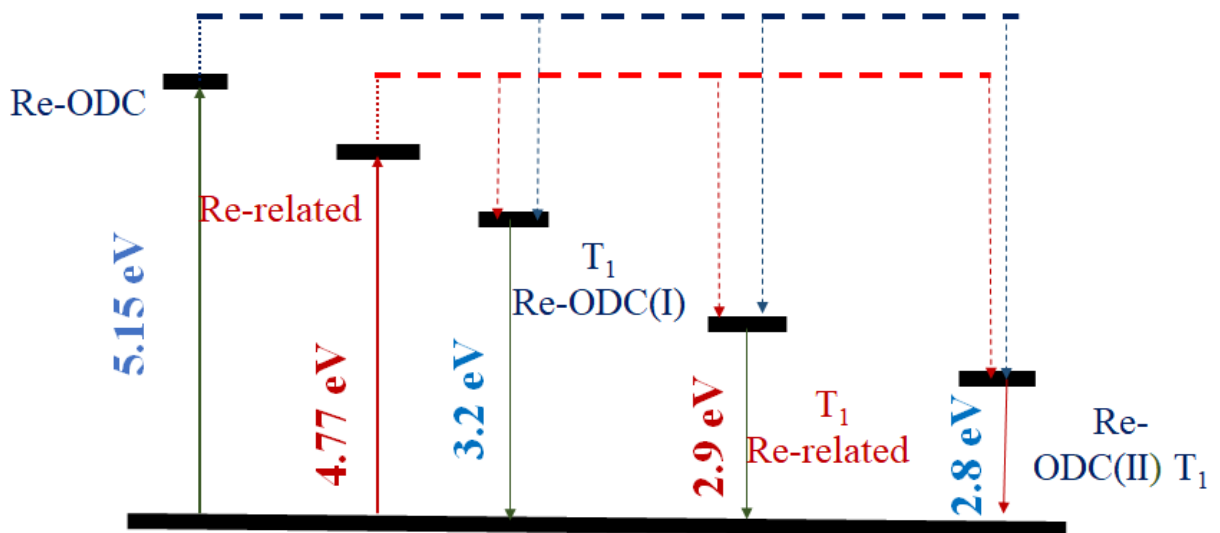


Figure 4.7 – Scheme of energy levels and electronic transitions for Re-ODC and Re-related centers in Re implanted SiO₂. Solid lines represent the excitation and emission optical transitions, dashed lines show the non-radiative energy transfer from the singlet excited states (S_1) to the triplet emission levels (T_1).

We can summarize the results obtained, assume the Re-related center represents the silicon oxygen-deficient center modified by Re ion located in the near circumference. Change in the energy structure of Re-related compared to the Re-ODCs is due to the bothersome influence of Re ions and is related to the alteration of local atomic

configuration of Re-ODCs. We suppose, shifts of PL and PLE bands of ODCs under the modification by Re ion is associated with changes in the positions of adiabatic terms (Figure 4.8).

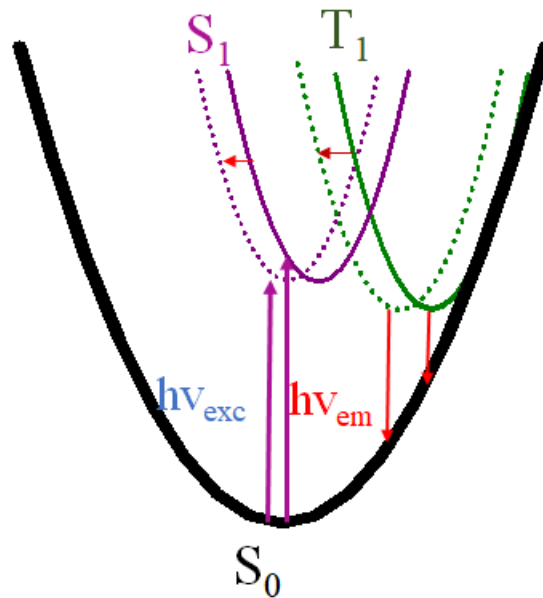


Figure 4.8 – Adiabatic terms of singlet and triplet states in Re-ODC (solid lines) and Re- related (dot lines). Arrows show excitation and emission transitions[⁶].

System of singlet S_1 and triplet T_1 energy levels should be shifted to the left along the configuration coordinate for Re- related compared with Re-ODC in order to provide the lower energy of excitation and the higher energy of emission, as we observe from experiment. Summarizing the obtained spectral data, we suppose that the atomic structure of Re-modified ODC can apparently be attributed to the ODC(II)-type.

4.7 Luminescence at VUV-excitation of Re ions implanted silica glass

4.7.1 The photoluminescence Re-ODC(II) under excitation 6.97 eV

The photoluminescence spectra of Re implanted SiO_2 under excitation of 6.97 eV at room temperature before and after thermal annealing are shown in Figure 4.9. These spectra were deconvoluted using Gaussian components in order to separate the contribution of luminescence bands with different nature.

Before thermal annealing, the photoluminescence spectrum of SiO₂: Re exhibits intense bands with maxima at 2.53, 2.77, 3.1 eV along with the less intense bands at 3.7 and 4.15 eV (Figure 4.9a). After annealing, there is increase in the intensities of 3.1 and 3.7 eV bands, as well as a slight decrease in the intensity of 2.53 eV band. Spectral parameters of observed luminescence signals are summarized in Table 4.4.

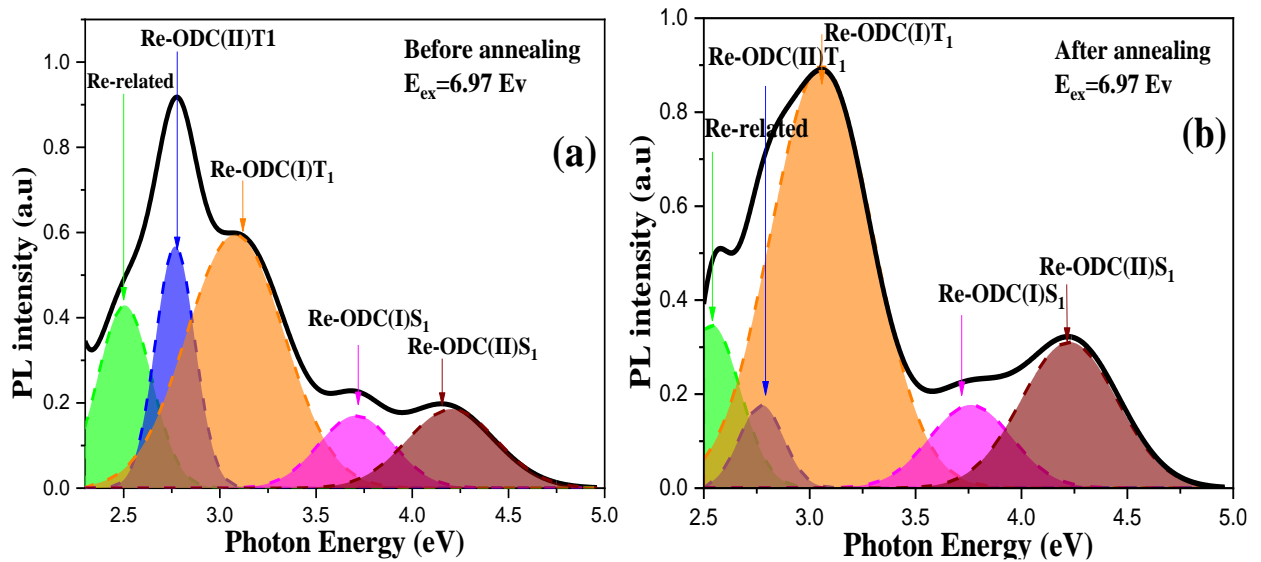


Figure 4.9 – Photoluminescence spectra of SiO₂: Re glass (ion fluence $5 \times 10^{16} \text{ cm}^{-2}$) at excitation of 6.97 eV before (a) and after (b) thermal annealing (1000 °C, t = 1h).

Table 4.4 – Spectral parameters of PL bands under excitation of 6.97 eV for silica glass implanted with rhenium ions before and after thermal annealing.

<i>PL band</i>	Re-related	Re- ODC(II)- T ₁	Re- ODC(I)-T ₁	Re- ODC(I)- S ₁	Re- ODC(II)- S ₁
Before annealing					
<i>hν, eV</i>	2.50	2.76	3.08	3.708	4.20
<i>FWHM, eV</i>	0.316	0.239	0.592	0.454	0.545
After annealing					
<i>hν, eV</i>	2.53	2.7	3.057	3.76	4.22
<i>FWHM, eV</i>	0.319	0.243	0.562	0.455	0.527

4.7.2 The photoluminescence Re-ODC(I) under excitation 7.75 eV

The photoluminescence spectrum at excitation of 7.75 eV for SiO₂:Re before thermal annealing consist of bands with a maximum at 2.77, 3.1, 3.67 and 4.15 eV (Figure 4.10a).

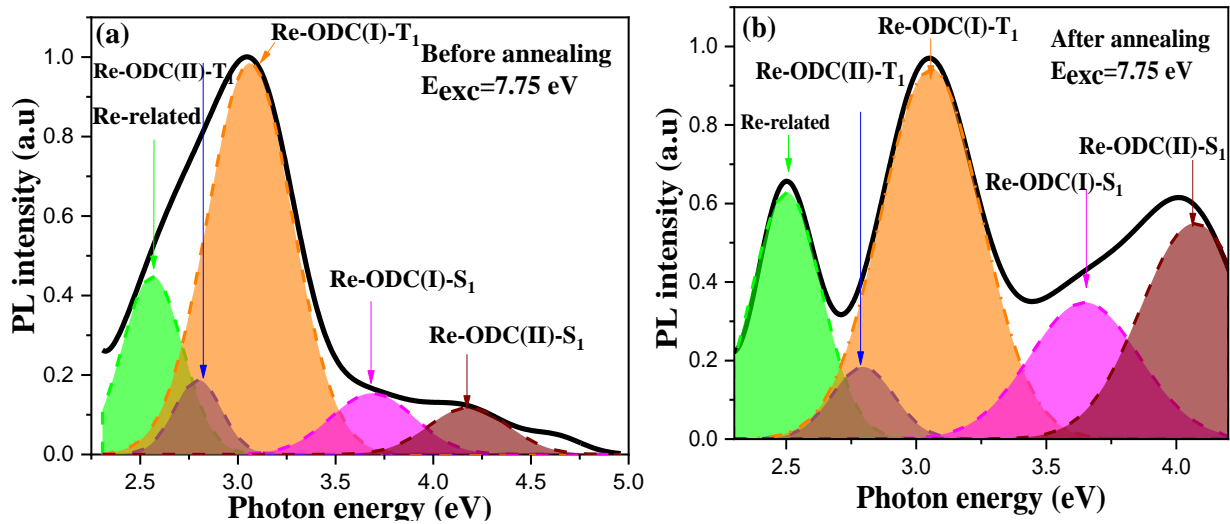


Figure 4.10 – Photoluminescence spectra of SiO₂:Re glass (ion fluence 5×10^{16} cm⁻²) at excitation of 7.75 eV before (a) and after (b) thermal annealing (1000 °C, t = 1 h).

Table 4.5 – Spectral parameters of PL bands under excitation of 7.75 eV for silica glass implanted with rhenium ions before and after thermal annealing.

PL band	<i>Re-related</i>	<i>Re-ODC(II)-T₁</i>	<i>Re-ODC(I)-T₁</i>	<i>Re-ODC(I)-S₁</i>	<i>Re-ODC(II)-S₁</i>
Before annealing					
hν, eV	2.56	2.79	3.06	3.68	4.18
FWHM, eV	0.351	0.280	0.5031	0.491	0.478
After annealing					
hν, eV	2.50	2.79	3.057	3.64	4.072
FWHM, eV	0.312	0.279	0.445	0.491	0.489

After thermal annealing, a new band at 2.5 eV appears (Figure 4.10 2b). In addition, the band at 2.77 eV shows a strong decrease in intensity with a simultaneous increase in the intensity of the bands at 3.67 eV and 4.15 eV. The main spectral parameters of emission bands are listed in Table 4.5.

4.7.3 The photoluminescence excitation at emission 4.1 eV

The PLE spectra for the SiO₂:Re measured for emission 4.1eV are shown in Figure 4.11. It is known that the PLE bands with the maxima at 7.71 eV and 6.9 eV are caused by optical transitions in so-called ODC(I) and ODC(II), respectively. ODC(I) represents the neutral single oxygen vacancy, and ODC(II) is the two-fold coordinated silicon atom (divacancy of oxygen) [186]. Thermal annealing leads to a shift in the PLE bands for ODC(I) and ODC(II), which become to be located at 7.81 and 7.02 eV (see Table 4.6).

The observed luminescence bands (Figure 4.9 and Figure 4.10) indicate the formation of oxygen-deficient centers in Re implanted SiO₂ [187]. Radiative transitions from excited triplet states ($T_1 \rightarrow S_0$) of ODC's showed up as luminescence bands at 2.77 and 3.1 eV before annealing and at 2.76 and 3.08 eV after annealing. The luminescence bands of 3.7 and 4.15 eV are associated with singlet-singlet radiative transitions ($S_1 \rightarrow S_0$) in ODCs (Figure 4.10). The shift of the maxima of the singlet and triplet PL bands in the spectra of SiO₂:Re relative to those of the analogous bands in pure glassy SiO₂ was explained by the modification of oxygen-deficient centers with Re ions. Also, the predominance of defects like ODC (II) over defects ODC (I) was seen after thermal treatment of SiO₂:Re. Therefore, the obtained results indicate the possibility of modifying the Luminescence properties of SiO₂ glass by implantation with rhenium ions.

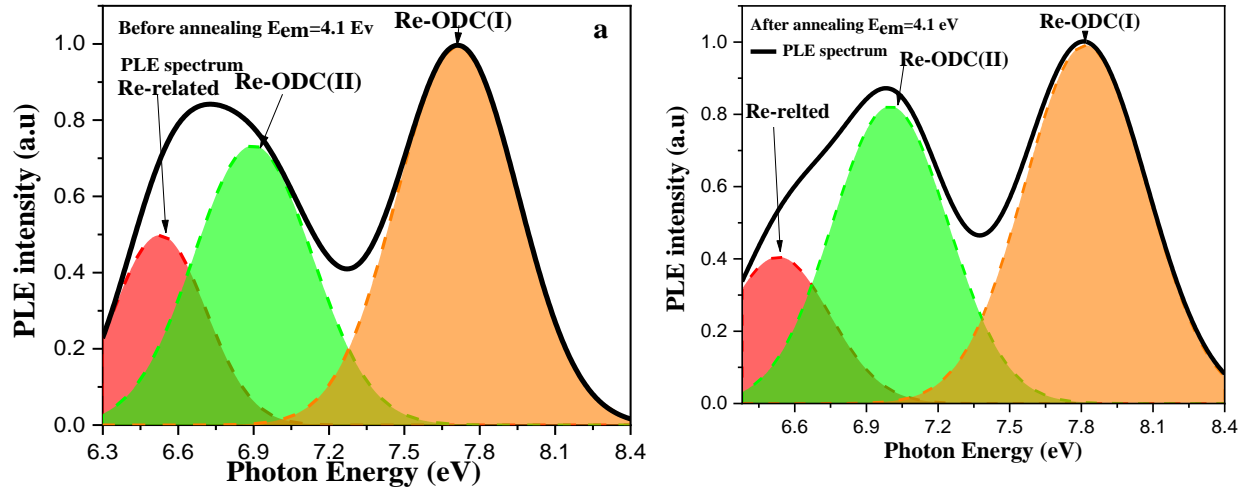


Figure 4.11 – PLE spectra for SiO₂: Re glass (ion fluence $5 \times 10^{16} \text{ cm}^{-2}$) before (a) and after (b) annealing (at 1000 °C, $t = 1 \text{ h}$) at the emission 4.1 eV.

Table 4.6 – Spectral parameters of PLE bands under emission of 4.1 eV for silica glass implanted with rhenium ions before and after thermal annealing.

PLE band	Re-related	Re-ODC(II)	Re-ODC(I)
Before annealing			
h ν , eV	6.527	6.9	7.71
FWHM, eV	0.4282	0.551	0.562
After annealing			
h ν , eV	6.53	7.01	7.81
FWHM, eV	0.504	0.567	0.597

An energy diagram of radiative and nonradiative transitions in ODCs is shown in Figure 4.12. The PL bands at 7.71 eV and 6.9 eV (Figure 4.11) correspond to transition 1 in ODC(I) and ODC(II), respectively.

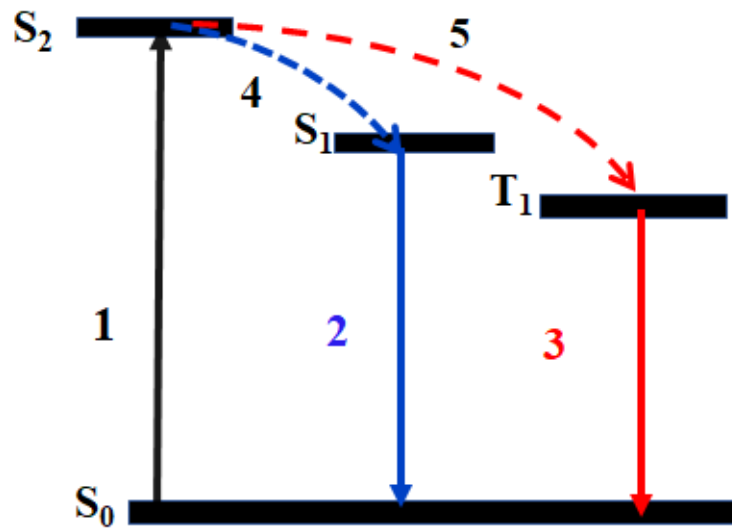


Figure 4.12 – Energy scheme of radiative and non-radiative optical transitions in oxygen-deficient centers (Re-ODCs).

Radiative transitions 2 and 3 characterize the PL bands of singlet-singlet and triplet-singlet luminescence (Figure 4.9 and 4.10). Finally, transitions 4 and 5 illustrate the occupation of singlet states S_1 and triplet states T_1 under the excitation of ODC luminescence.

4.8 Conclusions

We studied the formation of optically active radiation-induced defects in the surface layer of KI silica glass implanted with rhenium ions.

the main results obtained can be summarized as follows:

1. The ion-beam modification of KI glass samples implanted with rhenium ions with an energy of 80 keV has been investigated.
2. The calculation of the ion depth distribution profiles showed that with an increase in the ion energy, both the penetration depth and the width of the distribution profile increase, which covers two times thicker layers than at an energy of 30 keV.

3. The formation of optically active radiation defects in the surface layer of Silica glass has been studied by the methods of optical absorption and photoluminescence. Type E' and Re-ODC centers were found.
4. A new type of centers with an absorption band of 4.77 eV and a luminescence band of 2.9 eV, which have a different energy structure than Re-ODC, has been registered.
5. The photoluminescence method has revealed an efficient energy transfer from Re-ODC to Re-related centers, the luminescence of which can be excited through the Re-ODC absorption band.
6. Thermal annealing of SiO₂ samples implanted with Re ions causes the conversion of paramagnetic defects such as E'-centers, which leads to an additional increase in the concentration of modified diamagnetic Re-ODC and Re-related centers.
7. The photoluminescence of Re-ODC is characterized by a shorter lifetime compared to the PL of a typical Si-ODC due to a partial decrease in the exclusion of optical transitions.
8. The results of studies of photoluminescence under high-energy excitation indicate the formation of various modifications of oxygen-deficient centers, which include Re-modified oxygen monovacancies (ODC (I)) and two-coordinated silicon atoms (ODC (II)).
9. The results obtained indicate the possibility of changing the luminescence properties of SiO₂ glass by implantation with rhenium ions. Subsequent annealing of the samples makes it possible to additionally change the ratio of the concentrations of the resulting defects.

CHAPTER 5. OPTICAL PROPERTIES OF SILICA GLASSES IRRADIATED WITH DIFFERENT TYPES OF HEAVY IONS

The studies presented in the previous chapters show that irradiation of glassy SiO₂ with Re ions carries out both from the modification of the structure of the glass matrix itself, and to the modification of intrinsic defects by implanted ions. In this regard, it is of interest to comparatively analyze data from studies of SiO₂ samples implanted with other types of ions (for example, rare earth and typical elements) in order to establish general patterns and differences of such effects.

5.1 Influence of the type of silica glass matrix on structural disordering during ion implantation

The effective penetration depth of Re ions in KUVI Silica glass at 30 keV is 21 nm, and Re ions implanted into KI Silica glass with an energy of 80 keV penetrate most effectively to a depth of 40 nm (Fig. 5.1a). In this case, the distribution profile of Re ions implanted with an energy of 80 keV is twice as wide.

It was also found that Bi and Gd ions implanted in Hongan and KUVI Silica glass, respectively, at energies of 30 keV, have approximately the same effective penetration depth (20-22 nm) [188,189], as in the case of Re ions of 30 keV (fig. 5.1b), however, the profiles of the distribution of Bi and Gd ions over the depth are one and a half times wider than that of Re ions (30 keV). The results of calculations by the SRIM program are shown in Table 5.1.

The Simulation data show that the features of the SiO₂ matrix are weakly affected by the process of its implantation with ions. The radius and mass of ions, as well as their kinetic energy, have a greater influence. The depth of penetration of ions is almost directly proportional to the energy (twice the energy - twice the maximum of the distribution). With a decrease in the radius of ions and an increase in their mass, the distribution profile becomes wider. The increase in energy also widens the distribution profile.

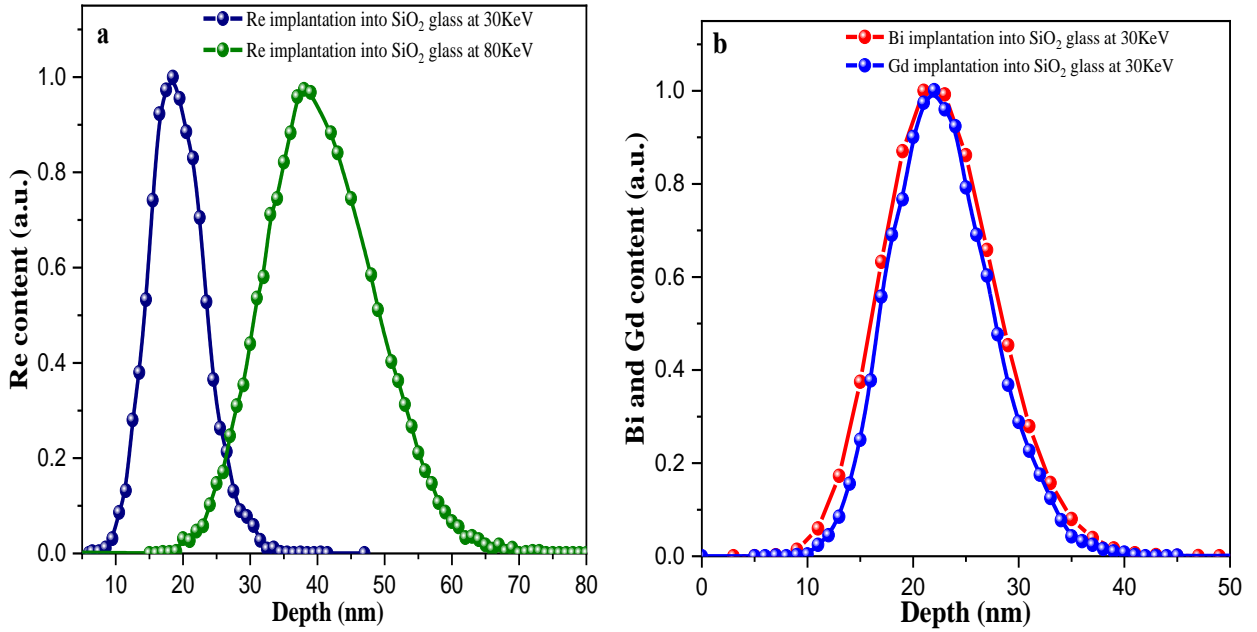


Figure 5.1 – SRIM simulation of penetration depths for: (a) 30 keV and 80 keV Re ions into the KUVI-SiO₂ matrix and the KI-SiO₂ matrix, respectively; (b) Bi and Gd ions with an energy of 30 keV into the Honan-SiO₂ matrix-base and KUVI-SiO₂ matrix-base, respectively.

Table 5.1 – Parameters of Silica glass implanted with Re at 30 keV and 80 keV, Bi and Gd ions at 30 keV

Type	KUVI Silica glass with Re at 30 keV	KI Silica glass with Re at 80 keV	KV Silica glass (Hongon) with Bi at 30 keV	KUVI Silica glass with Gd at 30 keV
Energy gap E_g^{opt} (eV)	8.035*, (8.11)* 8.015 – 8.029	—	8.019*, (8.49)* 7.920 – 8.008	8.115*, (8.45)* 7.966 – 8.076
Urbach energy E_U (eV)	0.130* 0.144– 0.173	—	0.355* 0.400– 0.582	0.249* 0.295– 0.405

Note: * data for non-implanted Silica glass (the value of the bandgap determined by the Urbach method is shown in brackets).

The behavior of the absorption edge of the glasses under study makes it possible to analyze the relationship between the change in the band gap E_g^{opt} and the degree of disordering of the atomic structure at different doses of implantation. The magnitude of the atomic disorder of the matrix of the optical material can be estimated from the value of the Urbach energy, which is associated with the length of the band tails of localized states in the forbidden gap. A decrease in the band gap E_g^{opt} occurs with lengthening of the band tails and correlates with an increase in the Urbach energy. For all Silica glass samples and ion implantation modes, the Urbach crystal rule is observed, which is characterized by a fan-shaped change in the slope of the spectral dependences. Results of studying the regularities of structural disordering of various SiO₂ matrices upon implantation with Re, Bi, and Gd ions, are shown in Table 5.1. [13,188,189].

Different grades of Silica glass have close band gaps E_g^{opt} in the range from 8.02 to 8.12 eV, determined by the Taus method. Urbach's method gives overestimated values in the range of 8.11 - 8.46 eV.

This feature is associated with the different physical meaning of the obtained E_g^{opt} values. The optical gap corresponding to the region of the Urbach absorption edge is the band gap between the localized electronic states in the tails of the valence and conduction bands. This value is also known as the "mobility gap" in amorphous systems with a high degree of structural disorder. The values of the band gap determined for the spectral region of the power-law dependence of the absorption coefficient in coordinates for direct and indirect optical transitions correspond to the band gap between the general electronic states of the matrix.

Ion implantation increases the degree of structural disorder and decreases the band gap. The highest degree of disorder was recorded in Silica glasses from the Chinese manufacturer Hongan. The Urbach energies in this glass varied in the range 0.355 - 0.582 eV [13] and the lower value corresponds to the original non-implanted glass.

The KUVI glass is distinguished by the most ordered structure. The Urbach energy in the indicated matrix varied in the range 0.130–0.173 eV.

One more general effect should also be noted - an abrupt increase in Urbach energy at low implantation doses, which is observed for all types of ions used. Already the first small dose gives a change in the Urbach energy by 0.015 - 0.046 eV. Further irradiation leads to a gradual increase in the degree of structural disorder (Table 5.4). The highest radiation resistance was demonstrated by the KUVI glass upon implantation with Re ions. In the range of Re fluences $5 \cdot 10^{15}$ - $5 \cdot 10^{17}$ cm⁻², the Urbach energy increased by only 30 meV. The Hongan glass was disordered to a greater extent upon implantation with Bi ions. In the range of Bi fluences of 10^{16} - $3 \cdot 10^{17}$ cm⁻², the Urbach energy increased by 180 meV, which is 6 times more than in the case of KUVI glass.

The general structural disorder in silica glass with implanted Re, Bi, and Gd ions directly affects the features of their band-energy structure, which, in turn, determines the optical properties of the material.

5.2. Ion-modified centers of the type oxygen monovacancy or ODC(I)

According to independent literature data [58,187] and our research [167] ODC (I) defects have two absorption bands at 7.5–7.6 and at 5.05 eV and two luminescence bands at 3.1 and 4.3 eV, as shown in Figure 5.2. The luminescence energy of 4.3 eV is associated with singlet-singlet radiative transitions, and 3.1 eV is associated with singlet-triplet transitions. Intercombination conversion ($S_1 \rightarrow T_1$) is possible between singlet and triplet states. The 7.6 eV transition is interpreted differently in various literary sources. A number of authors define it as the transition $S_0 \rightarrow S_1$ [46,58,187], while others consider $S_0 \rightarrow S_2$ [167,190] In the latter case, the 5.05 eV absorption band is attributed to the $S_0 \rightarrow S_1$ transition.

ODC(I)

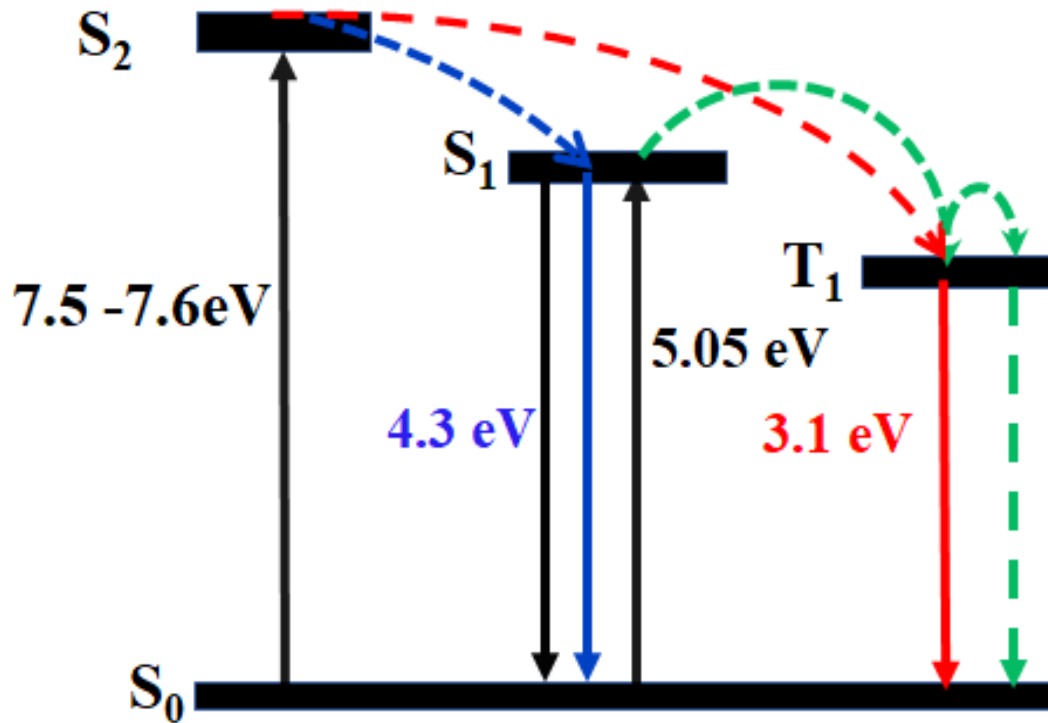


Figure 5.2 – Diagram of electronic transitions of defect centers Si-ODC (I) in silica glass: S_0 , S_1 and T_1 are the ground and excited states of the singlet and triplet type, respectively.

At the same time, as shown by the studies presented above, implantation with Re ions leads to the modification of defect centers ODC (I), which manifests itself in the form of displacement of luminescence bands. In KUVI silica glass implanted with Re ions at 30 keV, triplet-singlet radiative transitions ($T_1 \rightarrow S_0$) gave a maximum luminescence at energies 3.17-3.19 eV (FWHM = 0.47-0.52 eV) at various temperatures from 8 to 500 K, which differs by 0.07 - 0.09 eV from the peaks with pure SiO_2 . Significantly large changes were observed for singlet-singlet radiative transitions ($S_1 \rightarrow S_0$), which at various temperatures from 8 to 500 K gave a maximum luminescence at energies of 3.63–3.79 eV (FWHM = 0.41 eV), which differs by 0.51–0.67 eV from similar transitions in pure SiO_2 (Table 5.2). Implantation with

80 keV Re ions leads to a similar modification of ODC (I). The energy of singlet-triplet radiative transitions is 3.06 eV, and that of singlet-singlet transitions is 3.68 eV (Table 5.2).

Table 5.2 – Optical electronic transitions upon excitation and luminescence of ODC (I) defect centers in pure silica glass and matrices implanted with 30 keV Re, Bi, and Gd ions and 80 keV Re ions.

Type Defects	Unimplanted, pure SiO ₂	KUVI Silica glass with Re at 30 keV	KI Silica glass with Re at 80 keV	KV Silica glass (Hongang) with Bi at 30 keV	KUVI Silica glass with Gd at 30 keV
ODC(I) T ₁ at Exc = 7.5-7.75 eV	3.1	3.17-3.19 (0.47-0.52)	3.06 (0.501)	—	3.1
ODC(I) T1 at Exc = 5-5.05 eV	3.1 (0.5)	3.01 (0.3)	3.2 (0.4)	3.33 (0.18),	—
ODC(I) S1 at Exc = 7.5-7.75 eV (ODC(I))	4.3	3.63-3.79 (0.41)	3.68 (0.45)	—	—
ODC(I) T1 at Exc = 5-5.05 eV	4.3	—	—	—	—

Were also investigated ODC (I) arising from the implantation of Silica glass with Bi and Gd ions [184,191] Measurements have shown that the energy of triplet-singlet radiative transitions in modified Bi-ODC (I) is 3.33 eV (FWHM = 0.7-0.8 eV). Upon implantation of 30 keV Gd, triplet-singlet radiative transitions ODC (I) have the same energy as in pure SiO₂ (Table 5.2). The excitation bands for all of the listed

luminescence bands have approximately the same energy as in pure SiO₂: 5.05 eV and 7.5-7.75 eV for the S₀ → S₁ and S₀ → S₂ transitions, respectively.

Thus, we can conclude that the modification of ODC (I) with Re and Bi ions increases the energy of triplet-singlet radiative transitions by 0.1-0.2 eV and decreases the energy of singlet-singlet ones by 0.51 - 0.67 eV.

5.3. Ion-modified centers of the two-coordinated silicon or ODC(II).

According to independent literature data [58,187] and our research [167] ODC (II) defects have two absorption bands at 6.8-7.0 and at 5.15 eV and two luminescence bands at 2.7 and 4.4 eV, as shown in Figure 5.3. The luminescence energy of 4.4 eV is associated with singlet-singlet radiative transitions, and 2.7 eV with singlet-triplet transitions. Intercombination conversion (S₁ → T₁) is possible between singlet and triplet states. The 6.8 eV transition is interpreted by most authors as S₀ → S₂ between the ground and the second excited singlet state [52, 58,187]. At the same time, the 5.15 eV absorption band is attributed to the S₀ → S₁ transition.

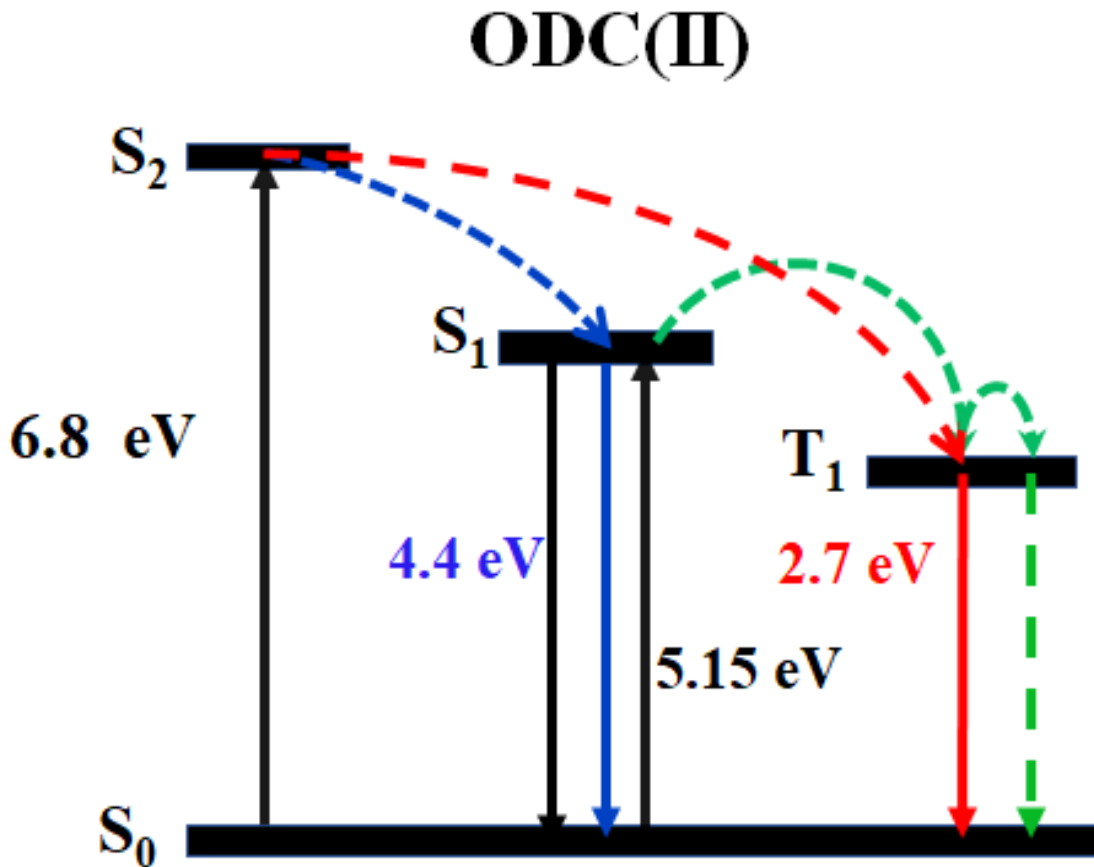


Figure 5.3 – Diagram of electronic transitions of defect centers Si-ODC (II) in silica glass: S_0 , S_1 , S_2 and T_1 are the ground and excited states of the singlet and triplet type, respectively.

At the same time, as shown by the studies presented above, implantation with Re ions leads to the modification of defect centers Si-ODC (II), which manifests itself in the form of displacement of luminescence bands. In KUVI Silica glass implanted with Re ions at 30 keV, triplet-singlet radiative transitions ($T_1 \rightarrow S_0$) gave a maximum luminescence at energies of 2.67-2.79 eV (FWHM = 0.76 eV) at different temperatures from 8 to 500 K, which at equal temperatures is approximately differs by 0.09 eV from the peaks with pure SiO₂. Somewhat larger changes were observed for singlet-singlet radiative transitions ($S_1 \rightarrow S_0$), which at various temperatures from 8 to 500 K gave a maximum luminescence at energies 4.17-4.19 eV (FWHM

= 0.76 eV), which differs by 0.21 - 0.23 eV from similar transitions in pure SiO₂ (Table 5.3). Implantation with 80 keV Re ions leads to a similar modification of ODC (II). The energy of singlet-triplet radiative transitions is 2.70-2.76 eV, and singlet-singlet 4.20-4.22 eV (Table 5.3).

Table 5.3 – Optical electronic transitions upon excitation and luminescence of ODC (II) defect centers in pure silica glass and matrices implanted with 30 keV Re, Bi, and Gd ions and 80 keV Re ions.

Type Defects	Unim- planted, pure SiO ₂	KUVI Sil- ica glass with Re at 30 keV	KI Silica glass with Re at 80 keV	KV Sil- ica glass (Hongan) with Bi at 30 keV	KUVI Sil- ica glass with Gd at 30 keV
ODC(II) T1 at Exc = 6.6-7 eV	2.7	2.67-2.79 (0.76)	2.7-2.76 (0.31)	—	2.8
ODC(II) T1 at Exc= 5,15-5.2	2.75-2.8 (0.32)	2.71 (0.34)	2.82	2.8,	—
ODC(II) S1 at Exci = 6.6-7 eV	4.4	4.17-4.19 (0.76)	4.20-4.22 (0.52-0.54)	—	—
ODC(II) S1 at Exc = 5,15-5.2 eV	4.4	—	—	—	—

We also studied ODC (II) arising from the implantation of quartz glasses with Bi and Gd ions [184,191]. Measurements have shown that the energies of triplet-singlet radiative transitions in ODC (II) modified Bi and Gd are the same and amount to 2.8 eV.

The excitation bands for all of the listed luminescence bands have approximately the same energy as in pure SiO₂: 5.15 eV and 6.6-7.0 eV for the S₀ → S₁ and S₀ → S₂ transitions, respectively.

Thus, it can be concluded that the modification of ODC (II) with Re, Bi, and Gd ions increases the energy of triplet-singlet radiative transitions by 0.06-0.1 eV and decreases the energy of singlet-singlet transitions by 0.18 - 0.23 eV. As shown in Section 5.3, the modification of ODC (I) defect centers is similar to the same regularities, but the magnitude of the shift of the singlet-singlet luminescence band is much larger.

5.4. New defect centers related with Re, Bi and Gd Ions.

As shown by the studies given in the previous chapters, ion implantation leads to the emergence of centers of a new type, which are absent in pure silica glass.

The main result of comparing the processes of defect formation in SiO₂ matrices upon their implantation with Re, Bi, and Gd ions is the established fact of the appearance of modified defect centers M-ODC (I) and M-ODC (II), where M = Re, Bi, or Gd. Their modification with these ions increases the energy of triplet-singlet radiative transitions and decreases the energy of singlet-singlet transitions. In this case, the change in the spectral parameters of the singlet-singlet luminescence of the M-ODC (I) centers occurs much more noticeably than for the M-ODC (II) centers.

Another important result is that ion implantation leads to the appearance of Re-related centers with a PL excitation band of 4.7–4.8 eV, which in its position can be attributed to the absorption of non-bridging oxygen centers (NBOHC). However, the energy of the luminescence transitions of this defect is 2.53–2.58 eV (Table 5.4), which is 0.6–0.7 eV higher than the luminescence energy of NBOHC in pure SiO₂. It can be assumed that, by analogy with Re-modified ODCs, this defect is a non-bridging oxygen center modified with rhenium ions. As our studies show, the effect of Re ions in the local environment of luminescent centers is of a general nature: the PL excitation bands remain unchanged, and the energy of luminescent transitions changes by tenths of electron volts. Similar effects of the appearance in silica glasses of modified centers of nonbridging oxygen with altered spectral characteristics were observed earlier in [192].

Another luminescence band with a maximum of 2.9 eV is also excited at an energy of 4.77 eV and, apparently, is associated with defects of a different nature (Table 5.4). It should also be noted that the indicated bands at 2.53 and 2.9 eV are also recorded upon excitation of Re-ODC. This fact can be explained by the transfer of energy between Re-ODC and centers of a new type, which confirms our assumption that one of the new defects belongs to Re-NBOHC. In particular, the paper [167] revealed the fact of energy transfer between ODC and NBOHC in pure SiO₂. Similar effects can occur with Re modified centers.

Table 5.4 – Table 3. Comparison of the parameters of M-related centers in Silica glasses implanted with Re ions with energies of 30 keV and 80 keV, Bi and Gd ions with energies of 30 keV

Excitation energy (eV)	Unimplanted, pure SiO ₂	KUVI Silica glass with Re at 30 keV	KI Silica glass with Re at 80 keV	Silica glass (Hongan) with Bi at 30 keV	KUVI Silica glass with Gd at 30 keV
6.6-7, indirect (ODC(II))	—	—	2.50-2.53 (0.31)	—	2.2 -2.3 (0.3)
5.15-5.2, indirect (ODC)	—	2.85 (0.18), 2.53 (0.34), 2.28 (0.28)	2.92	3.08 (0.18)	—
4.7-4.8, intracenter M -related	—	2.85 (0.18), 2.53 (0.24), 2.28 (0.27)	2.9 (0.3)	2.95 (0.11) 2.58 (0.19)	—
Si QDs Exc = 6.6-7 eV (ODC(II))	1.8	—	—	—	1.8 (0.1)

Note: M = Re, Bi or Gd (type of implanted ion).

Implantation of Bi ions with an energy of 30 keV also leads to the appearance of both types of similar defects. In the luminescence spectrum upon excitation of 4.7–

4.8 eV, the bands at 2.58 eV and 2.95 eV are observed, which are presumably related by bismuth ions introduced into the SiO₂ matrix [192]. By analogy with Re-NBOHC, the 2.58 eV band can presumably be associated with Bi-NBOHC

In Silica glass of the KUVI brand, implanted with Gd ions, centers of a new type associated with implanted ions are also recorded. the 2.2 eV PL band appears at an excitation energy of 6.6 eV and cannot be assigned to any known active PL center in SiO₂. It can be assumed that the luminescence in this center is associated with optical transitions in Gd ions localized near ODC (II), which provides the possibility of nonradiative energy transfer between these defects.

In addition, in KUVI SiO₂ samples implanted with Gd ions, after annealing, a PL band appears with a maximum at 1.8 eV, which, in terms of spectral parameters, corresponds well to the luminescence of silicon quantum dots. [154, 184,193]. The formation of these centers of luminescence, in the article [184] is explained by the transformation of oxygen-deficient centers during thermal annealing with the formation of silicon quantum dots.

5.5 Conclusion

As a result of a comparison of the properties of SiO₂ matrices of various types and the regularities of defect formation in these matrices upon implantation of Re, Bi, and Gd ions with an energy of 30 keV and Re ions with an energy of 80 keV, the following conclusions can be shown:

1. The distribution profiles of embedded ions are largely influenced by their energy, and to a lesser extent by their radius and mass. The depth of penetration of ions proportionally depends on the energy. The increase in energy also widens the distribution profile. With a decrease in the radius of ions and an increase in their mass, the distribution profile also broadens.
2. Ion implantation increases the degree of structural disorder and decreases the energy gap of the irradiated matrix. The highest degree of disorder and the lowest radiation resistance was recorded in Silica glasses from the Chinese manufacturer

Hongan. The most ordered and radiation-resistant structure is characteristic of the ultrapure glass KUVI, type (IV).

3. Implantation of silica glasses with heavy Re, Bi, and Gd ions leads to the appearance of modified defect centers of the ODC (I) and ODC (II) types, which are not recorded in the pure SiO₂ glasses.
4. New optical centers of unknown nature, different from ODCs and formed under the action of different types of heavy ions (Re, Bi, Gd), have been discovered, a separate type of which is presumably associated with the presence of Re ions in the local environment of the centers of the nonbridging oxygen atom (NBOHC).
5. Using Re ions as an example, it is shown that the formation mechanism, local structure, and, accordingly, the luminescent properties of Re-related centers substantially depend on the energy of the ions being introduced. Upon implantation of ions with energies of 30 and 80 keV, the luminescence bands have different positions.
6. The general regularity of the modification of ODC (I) and ODC (II) centers by heavy ions (Re, Bi, and Gd) consists in the distortion of their energy structure and manifests itself in an increase in the energy of triplet-singlet radiative transitions and a decrease in the energy of singlet-singlet transitions. In this case, the modification of the ODC with Bi ions leads to a larger shift of the luminescent bands, and the modification of Gd - to a smaller one than under irradiation with Re.

CONCLUSION

The main results of the dissertation work are as follows

1. By the methods of optical, luminescence and ERP spectroscopy, it has been established that under ion-beam exposure to SiO_2 glasses, the matrix is damaged and intrinsic defects appear: E' -centers, NBOHC, ODC (I), ODC (II).
2. Together with the known defects, new oxygen-deficient centers, modified by Re ions, appear. These include oxygen monovacancies Re-ODC (I) and divacancies Re-ODC (II), in the local environment of which implanted ions are located. Modification of the structure of the nearest environment of defects leads to a decrease in the energy of singlet-singlet intracenter electronic transitions and an increase in the energy of singlet-triplet transitions. The levels of the triplet states are shifted to a lesser extent, and the levels of singlet states are shifted to the greatest extent.
3. Implantation with Re ions also creates specific defects of a fundamentally new type (designated as Re-related). A separate type of these defects is presumably the Re-modified center of non-bridging oxygen (Re-NBOHC). The electronic structure of Re-related centers depends on the energy of implanted ions: upon implantation of ions with energies of 30 and 80 keV, the luminescence bands have different spectral characteristics.
4. The impact of different types of heavy ions is of a similar nature: defects of the M-ODC (I) and M-ODC (II) types are created with an altered energy structure, where M are implant ions (Re, Bi or Gd). In this case, the magnitude of the shift of the luminescence bands is mainly influenced by the radius and mass of the implanted ions.

5. Methods of optical spectroscopy established the main regularities of the disordering of the atomic structure during the implantation of Silica glasses with various fluences of heavy ions. The behavior of the fundamental absorption edge of Silica glass obeys the "crystal" Urbach rule. Ion-beam exposure leads to an increase in the total structural disorder of glassy SiO_2 , the degree of which depends on the type of matrix, the energy of the ion beam and manifests itself as a smearing of the band tails and a decrease in the effective energy gap.
6. The highest degree of disordering and the lowest radiation resistance are characteristic of Hongan Silica glasses from a Chinese manufacturer, and the most ordered structure and, accordingly, higher radiation resistance are characteristic of domestic ultra-pure glass KUVI (type IV).

Prospects for Further Development of The Topic. The results of this work are prerequisites for the further development of the physical foundations of creating new functional materials based on non-crystalline silicon dioxide and its analogs, obtained by methods of ion-beam technologies and intended for planar structures and devices of photonics and micro-, optoelectronics of a new generation.

LIST OF REFERENCES

1. Devine R. A. B. Structure and Imperfections in Amorphous and Crystalline Silicon Dioxide / R. A. B Devine, J. P. Duraud, E. Dooryhée. – Wiley, New York. – 2000. – 528P.
2. Griscom D. L. Defects in SiO₂ and related dielectrics: Science and Technology/ G. Pacchioni, L. Skuja, D. L. Griscom // Kluwer Academic, Dordrecht. - 2000. pp 73 –116.
3. Bogomolova L. D. Paramagnetic Species Induced by Ion Implantation of Pb⁺ and C⁺ Ions in Oxide Glasses / L. D. Bogomolova, V. A. Jachkin, S. A. Prushinsky, S.A. Dmitriev, S. V. Stefanovsky, Yu. G Teplyakov, F. Caccavale // J. Non-Cryst. Solids. – 1998. – V. 241. – P. 174 – 183.
4. Magruder R. H. Linear and Non-Linear Optical Properties of Lead Nanometer Dimension Metal Particles in Silica Formed by Ion Implantation / R. H. Magruder, R. A. Weeks, S. H. Morgan, Z. Panb, D. O. Henderson, R. A. Zuhrc // J. Non-Cryst. Solids. – 1995. – V. 192–193. – P. 546 – 549.
5. Zatsepin A. F. The MRO-Accompanied Modes of ReImplantation into SiO₂-Host Matrix: XPS and DFT Based Scenarios //A. F. Zatsepin, D. A. Zatsepin, D. W. Boukhvalov, N. V. Gavrilov, V. Ya. Shur, A. A. Esin // J. Alloys Compd. – 2017. – V. 728. – P. 759 – 766.
6. Tarpani Lu. Photoactivation of Luminescent Centers in Single SiO₂ Nanoparticles/ Lu. Tarpani, Daja Ruhlandt, Loredana Latterini, Dirk Haehnel, Ingo Gregor, Jörg Enderlein, Alexey I. Chizhik // Nano Lett. 2016 – V. 16. – P. 4312 – 43161.
7. Devine R. A. B. The structure of SiO₂, its defects and radiation hardness / R. A. B. Devine // IEEE Trans. Nucl. Sci. – 1994. – V. 41. – P. 452 – 459.
8. Francesca D. Di. Resonance Raman of oxygen dangling bonds in amorphous silicon dioxide / D. Di Francesca, A. Boukenter, S. Agnello, A. Alessi, S. Girard, M. Cannasband Y. Ouerdane // J. Raman Spectrosc. 2017. – V. 48. – P. 230 – 234.

9. Zatsepin A. F. Ionization effects in Si/SiO₂: Li, Na, K implanted structures under the impact of high-energy α particles / A. F. Zatsepin, E. A. Buntov, A. I. Slesarev, D. Yu. Biryukov // *Journal of Surface Investigation*. – 2016. – V. 306. – P. 603 – 607.
10. Zatsepin A. F. Energy band gaps and excited states in Si QD/SiO_x/R_yO_z (R = Si, Al, Zr) suboxide superlattices / A F Zatsepin, E A Buntov, D A Zatsepin, E Z Kurmaev, V A Pustovarov, A V Ershov, N W Johnson, Alexander Moewes // *J. Phys.: Condens. Matter* – 2019. – V. 31. – № 415301.
11. Fossum E.R. A Review of the Pinned Photodiode for CCD and CMOS Image Sensors / E.R. Fossum, D. B. Hondongwa // *IEEE J. Electron Devices Soc.* – 2014. – V. 2. – P. 33 – 43.
12. Green R. J. Electronic band gap reduction and intense luminescence in Co and Mn ion-implanted SiO₂ / R. J. Green, D. A. Zatsepin, D. J. St. Onge, E. Z. Kurmaev, N. V. Gavrilov, A. F. Zatsepin, A. Moewes // *Journal of Applied Physics*. – 2014. – V. 115. – № 103708.
13. Zatsepin A. F. Quasi-Dynamic Approach in Structural Disorder Analysis: An IonBeam-Irradiated Silica / Anatoly F. Zatsepin, Dmitry Yu Biryukov, Dmitry A. Zatsepin, Tatiana V. Shtang, Nikolay V. Gavrilov // *J. Phys. Chem. C*. – 2019. – V. 123. – P. 29324 – 29330.
14. Seddon A. S. Progress in rare-earth-doped mid-infrared fiber lasers / A. S. Seddon, Z. Tang, D. Furniss, S. Sujecki, T. M. Benson // *Optics Express*. – 2010. – V. 18. – P. 26704 – 26719.
15. Nekrashevich S. S. Electronic Structure of Silicon Dioxide (A Review) / S. S. Nekrashevich, V. A. Gritsenko // *Physics of the Solid State*. – 2014. – V. 56. – P. 207 – 222.
16. Yasaitis John A. Structure of Amorphous Silicon Monoxide / John A. Yasaitis, Roy Kaplow // *Journal of Applied Physics*. – 1972. – V.43. – P. 995 – 1000.

17. Lisovskii I. P. IR spectroscopic investigation of SiO₂ film structure / I. P. Lisovskii, V. G. Litovchenko, V. G. Lozinskii and G. I. Steblovskii // *Thin Solid Films*. – 1992. – V. 213. – P. 164–169.
18. El-Kareh B. *Fundamentals of Semiconductor Processing Technology* / B. El-Kareh. – academic publishers. – New York. – 1995. – 602P.
19. Altman I. Eric Structural and Electronic Heterogeneity of Two-Dimensional Amorphous Silica Layers / Eric I. Altman, Udo D. Schwarz // *Adv. Mater. Interfaces*. – 2014. – V. 1. – № 1400108.
20. Davis K.M. Quantitative infrared spectroscopic measurement of hydroxyl concentrations in silica glass / K.M. Davis, A. Agarwal, M. Tomozawa, K. Hirao // *Journal of Non-Crystalline Solids*. – 1996. – V. 203. – P. 27–36.
21. Horii N. Promoting vitreous silica devitrification by placement on a NaCl grain at 800 °C–1150 °C / N. Horii, N. Kuzuu, H. Horikoshi // *Jpn. J. Appl. Phys.* – 2021. – V. 60. – № 045503.
22. Osawa Ke. Smoothing of surface of silica glass by heat treatment in wet atmosphere / Kenta Osawa, Hiroyuki Inoue, Atsunobu Masuno, Keiichi Katayama, Yingjiu Zhang, Futoshi Utsuno, Yoshiyuki Sugahara, Kazuo Koya, Akira Fujinoki, Hiromasa Tawarayama, Hiroshi Kawazoe // *Journal of Applied Physics*. – 2011. – V. 109. – № 103520.
23. Schmelzer Jörn W. P. *Glass Selected Properties and Crystallization* / Jörn W. P. Schmelzer, Alexander S. Abyzov, René Androsch, Vladimir G. Baidakov, Vladimir M. Fokin, Stoyan Gutzov, Ivan S. Gutzow, Gyan P. Johari, Nikolai Jordanov, Alexander Karamanov, Viktor K. Leko, Frank-Peter Ludwig, Irena Markovska, Radost Pascova, Ivan Penkov, Boris Z. Pevzner, Irina G. Polyakova, Christoph Schick, Sergey V. Tarakanov, Natalia M. Vedishcheva, Gerhard Wilde, Adrian C. Wright, Andreas Wurm, Edgar D. Zanotto, Evgeny Zhuravlev // chapter 7 Regularities and Peculiarities in the Crystallization Kinetics of Silica Glass, De Gruyter. – 2014. – P. 377–439.

24. Plotnichenko V.G. Hydroxyl groups in high-purity silica glass / V.G. Plotnichenko, V.O. Sokolov, E.M. Dianov // *J. Non-Cryst. Solids.* – 2000. – V. 261. – P. 186–194.
25. Brockner R. Properties and Structure of Vitreous Silica/ R. Brockner // *J. Non-Cryst. Solids.* – 1970. – V. 5. – P. 123–175.
26. Alessi A. Phosphorous doping and drawing effects on the Raman spectroscopic properties of O = P bond in silica-based fiber and preform / A. Alessi, S. Girard, M. Cannas, A. Boukenter, Y. Ouerdane // *Opt. Mater. Express.* – 2012. – V.2. – 1391–1396.
27. Francesca D. Di Resonance Raman of oxygen dangling bonds in amorphous silicon dioxide / D. Di Francesca, A. Boukenter, S. Agnello, A. Alessi, S. Girard, M. Cannas, Y. Ouerdane // *J. Raman Spectrosc.* – 2017. – V. 48. – P. 230–234.
28. Skuja L. Luminescence and Raman detection of molecular Cl₂ and ClClO molecules in amorphous SiO₂ matrix / L. Skuja, K. Kajihara, Kr. Smits, A. Silins, Hi. Hosono // *J. Phys. Chem. C.* – 2017. – V.121. – P. 5261–5266
29. Sousa C. Optical properties of peroxy radicals in silica: multiconfigurational perturbation theory calculations / C. Sousa, C. de Graaf // *J. Chem. Phys.* – 2001. – V. 114. – P. 6259–6264.
30. Uchino T. Structure, energies, and vibrational properties of silica rings in SiO₂ glass / T. Uchino, Y. Kitagawa, T. Yoko, // *Phys. Rev. B.* – 2000. – V. 61. – P. 234–240.
31. Das U. Effect of Siloxane Ring Strain and Cation Charge Density on the Formation of Coordinately Unsaturated Metal Sites on Silica: Insights from Density Functional Theory (DFT) Studies / U. Das, Guanghui Zhang, Bo Hu, Adam S. Hock, Paul C. Redfern, Jeffrey T. Miller, Larry A. Curtiss // *ACS Catal.* – 2015. – V. 5. – P. 7177–7185.
32. Donadio D. Ab initio simulations of photoinduced interconversions of oxygen deficient centers in amorphous silica / D. Donadio, M. Bernasconi, M. Boero // *Phys. Rev. Lett.* – 2001. – V. 87. – № 195504.

33. Jia Ba. Structural disorder in fused silica with ODC(I) defect / Ba. Jia, Zixuan Guan, Zhixing Peng, Jie Zhang, Xiaoning Guan, Pengfei Guan, Bin Yang, You Wang, Pengfei Lu // *Applied Physics A*. – 2018. – V. 124. – № 696
34. Martin-Samos L. Neutral self-defects in a silica model: a first-principles study / L. Martin-Samos, Y. Limoge, J.-P. Crocombette, G. Roma, N. Richard, E. Anglada, and E. Artacho // *Phys. Rev. B*. – 2005. – V. 71. – № 014116.
35. Martin-Samos L. Defects in amorphous SiO₂: valence alternation pair model / L. Martin-Samos, Y. Limoge, G. Roma // *Phys. Rev. B*. – 2007. – V. 76. – № 104203.
36. Giacomazzi L. Medium-range structure of vitreous SiO₂ obtained through first-principles investigation of vibrational spectra / L. Giacomazzi, P. Umari, A. Pasquarello // *Phys. Rev. B*. – 2009. – V. 79. – № 064202.
37. Gerosa M. Communication: Hole localization in Al-doped Silica SiO₂ within ab initio hybrid-functional DFT / M. Gerosa, C. Di Valentin, C. E. Bottani, Gi. Onida, G. Pacchioni // *J. Chem. Phys.* – 2015. – V. 143. – № 111103.
38. Chang E.K. Excitons and optical properties of α -Silica / E.K. Chang, M. Rohlfing, S.G. Louie // *Phys. Rev. Lett.* – 2000. – V. 85. – P. 2613 – 2616.
39. Pickard C.J. All-electron magnetic response with pseudopotentials: NMR chemical shifts / C.J. Pickard, F. Mauri // *Phys. Rev. B*. – 2001. – V. 63. – № 245101.
40. Yates J.R. Calculation of NMR chemical shifts for extended systems using ultrasoft pseudopotentials / J.R. Yates, C.J. Pickard, F. Mauri // *Phys. Rev. B*. – 2007. – V. 77. – № 024401.
41. Pickard C.J. First-principles theory of the EPR g tensor in solids: defects in Silica / C.J. Pickard, F. Mauri // *Phys. Rev. Lett.* – 2002. – V. 88. – № 086403.
42. Pfanner G. Ab initio EPR parameters for dangling-bond defect complexes in silicon: effect of Jahn-Teller distortion / G. Pfanner, C. Freysoldt, J. Neugebauer, U. Gerstmann // *Phys. Rev. B*. – 2012. – V. 85. – № 195202.

43. Giacomazzi L. EPR parameters of E' centers in v-SiO₂ from first-principles calculations / L. Giacomazzi, L. Martin-Samos, A. Boukenter, Y. Ouerdane, S. Girard, N. Richard // *Phys. Rev. B.* – 2014. – V. 90 – № 014108.
44. Girard S. Radiation effects on silica-based preforms and optical fibers - II: coupling Ab initio simulations and experiments / S. Girard, Member, N. Richard, Member, Y. Ouerdane, G. Origlio, A. Boukenter, L. Martin-Samos, P. Paillet, Senior Member, J.-P. Meunier, Member, J. Baggio, Member, M. Cannas, R. Boscaino // *IEEE Trans. Nucl. Sci.* – 2008. – V. 55. – P. 3508 – 3514.
45. Richard N. Coupled theoretical and experimental studies for the radiation hardening of silica-based optical fibers / N. Richard, S. Girard, L. Giacomazzi, L. Martin-Samos, D. Di Francesca, C. Marcandella, A. Alessi, P. Paillet, S. Agnello, A. Boukenter, Y. Ouerdane, M. Cannas, R. Boscaino // *IEEE Trans. Nucl. Sci.* – 2014. – V. 61. – P. 1819 – 1829.
46. Girard, S. Overview of radiation induced point defects in silica-based optical fibers / S. Girard, A. Alessi, N. Richard, L. Martin-Samos, V. De Michele, L. Giacomazzi, S. Agnello, D. Di Francesca, A. Morana, B. Winkler, I. Reghioua, P. Paillet, M. Cannas, T. Robin, A. Boukenter, Y. Ouerdane // *Rev. Phys.* – 2019. – V. 4. – № 100032.
47. Skuja L. Optical properties of defects in silica. In *Defects in SiO₂ and related dielectrics: science and technology* edited by G. Pacchioni, L. Skuja, and D. L. Griscom, pp. 73–116. Springer, 2000.
48. Skuja L. Defects in oxide glasses / L. Skuja, M. Hirano, H. Hosono, and K. Kajihara // *physica status solidi (c)*. – 2005. – V. 2. – P.15–24.
49. Griscom D. L. Optical properties and structure of defects in silica glass / D. L. Griscom // *Journal of the Ceramic Society of Japan.* – 1991. – V. 99. – P. 923 – 942.
50. Griscom D. L. The natures of point defects in amorphous silicon dioxide. In *Defects in SiO₂ and related dielectrics: science and technology* edited by G. Pacchioni, L. Skuja, and D. L. Griscom, pp. 117 – 159. Springer, 2000.

51. Pacchioni G. Ab initio theory of optical transitions of point defects in SiO₂ / G. Pacchioni, G. Ierano. // *Physical Review B*. – 1998. – V. 57. – P. 818 – 832.
52. Sushko P. Structure and properties of defects in amorphous silica: new insights from embedded cluster calculations / P. Sushko, S. Mukhopadhyay, A. Mysovsky, V. Sulimov, A. Taga, and A. Shluger // *Journal of Physics: Condensed Matter*. – 2005. – V.17. – P. 2115 – 2140.
53. Weeks R.A. Paramagnetic Resonance of Lattice Defects in Irradiated Quartz / R.A. Weeks // *J. Appl. Phys.* – 1956. – V.27. – P.1376 – 1381.
54. Silsbee R.H. Electron Spin Resonance in Neutron-Irradiated Quartz / R.H. Silsbee // *J. Appl. Phys.* – 1961. – V.32. – P.1459 – 1461.
55. Yip K. L. Electronic structure of E₁' centers in SiO₂ / K.L. Yip, W.B. Fowler // *Physical Review B*. – 1975. – V. 11. – P. 2327 – 2338
56. Mahmud H. H. Generation and bleaching of E' centers induced in a-SiO₂ by c-irradiation / H. H. Mahmud, A. Mansour, F. M. Ezz-Eldin // *J Radioanal. Nucl. Chem.* – 2014. – V. 302. – P. 261 – 272.
57. Griscom D. L. Characterization of three E'-center variants in X- and γ-irradiated high purity a-SiO₂ / D. L. Griscom // *Nucl. Instrum. Methods Phys. Res. B*. – 1984. – V. 1. – P. 481 – 488.
58. Skuja L. Optically active oxygen-deficiency-related centers in amorphous silicon dioxide / L. Skuja // *J. Non-Cryst. Sol.* – 1998. – V. 239. – P. 16 – 48.
59. Guzzi M. Neutron irradiation effects in amorphous SiO₂: optical absorption and electron paramagnetic resonance / M. Guzzi, M. Martini, A. Paleari, F. Pio, A. Vedda, C.B. Azzoni // *J. Phys.: Condens. Matter*. – 1993. – V. 5. – P. 8105 – 8116.
60. Nishikawa H. Defects and optical absorption bands induced by surplus oxygen in high-purity synthetic silica / H. Nishikawa, R. Tohmon, Y. Ohki, K. Nagasawa, Y. Hama / *J. Appl. Phys.* – 1989. V. 65. – P. 4672 – 4678.

61. Cohen A.J. Neutron Specific Color Center in Fused Silica and an Impurity Band of Identical Wavelength //A.J. Cohen // Phys. Rev. – 1957. V. 105. – P. 1151 – 1155.
62. Guzzi M. Luminescence of fused silica: Observation of the O₂ emission band / M. Guzzi, M. Martini, M. Mattaini, F. Pio, and G. Spinolo // Phys. Rev. B. – 1987. – V. 35. – P. 9407 – 9409.
63. Watanabe M. Luminescence and defect formation by visible and near-infrared irradiation of vitreous silica / M. Watanabe, Sa. Juodkazis, H.-Bo Sun, Sh. Matsuo, H. Misawa, Phys. Rev. B. – 1999. V. 60. – P. 9959 – 9964.
64. Arnold G.W. Ion-Implantation Effects in Noncrystalline SiO₂ / G.W. Arnold // IEEE Trans. Nucl. Sci. – 1973. V. 20. – P. 220 – 223.
65. Imai H. Two types of oxygen-deficient centers in synthetic silica glass / H. Imai, K. Arai, H. Imagawa, H. Hosono, Y. Abe // Phys. Rev. B. – 1988. V. 38. – P. 12772 – 12775.
66. Kohketsu M. Photoluminescence in VAD SiO₂:GeO₂ Glasses Sintered under Reducing or Oxidizing Conditions / M. Kohketsu, K. Awazu, H. Kawazoe, M. Yamane, Jpn. J. Appl. Phys. – 1989. – V. 28. – P. 622 – 631.
67. Tohmon R. Correlation of the 5.0- and 7.6-eV absorption bands in SiO₂ with oxygen vacancy /R. Tohmon, H. Mizuno, Y. Ohki, K. Sasagane, K. Nagasawa, Y. Hama // Phys. Rev. B. – 1989. – V. 39. – P. 1337 – 1345.
68. Pio F. Intrinsic and Impurity-Related Point Defects in Amorphous Silica. A Spectroscopic Study / F. Pio, M. Guzzi, G. Spinolo, M. Martini // Phys. Status Solidi (b). – 1990. – V. 159. – P. 577 – 588.
69. Anedda A. Time resolved photoluminescence of a centers in neutron irradiated SiO₂ /A. Anedda, F. Congiu, F. Raga, A. Corazza, M. Martini, G. Spinolo, A. Vedda // Nucl. Instr. Meth. Phys. Res. B. – 1994. – V. 91. – P. 405 – 409.
70. Weissbluth M. Atoms and Molecules / M. Weissbluth. –Academic Press Inc., New York. – Elsevier. – 1978.

71. Friebele E.J. Fundamental Defect Centers in Glass: The Peroxy Radical in Irradiated, High-Purity, Fused Silica / E.J. Friebele, D.L. Griscom, M. Stapelbroek, R.A. Weeks // *Phys. Rev. Lett.* – 1979. – V. 42– P. 1346. – 1349.
72. O'Reilly E. P. Theory of defects in vitreous silicon dioxide/ E. P. O'Reilly, J. Robertson // *Phys. Rev. B.* – 1983. – V. 271. – P. 3780 – 3795.
73. Bhattacharyya P. Systematic First-Principles Configuration-Interaction Calculations of Linear Optical Absorption Spectra in Silicon Hydrides: Si_2H_{2n} ($n = 1-3$) / P. Bhattacharyya, D. K. Rai, A. Shukla // *J. Phys. Chem. A.* – 2019. – V.123. – P. 8619 – 8631.
74. Rupta R. P. Origin of the 7.6-eV peak in the optical absorption spectrum of neutron- and heavy-ion-irradiated SiO_2 / R.P. Rupta // *Phys. Rev. B.* – 1986. – V. 33. – P. 7274 – 7276.
75. Trukhin A. N. The correlation of the 7.6 eV optical absorption band in pure fused silicon dioxide with twofold-coordinated silicon / A. N. Trukhin, L. N. Skuja, A.G. Boganov, V.S. Rudenko, *J. Non-Cryst. Solids.* – 1992. – V. 149. – P. 96 – 101.
76. Khalilov V. K. Character, mechanism of formation and transformation of point defects in type IV silica glass / V.K. Khalilov, G. A. Dorfman, E. B. Danilov, M. I. Guskov, V. E. Ermakov // *J. Non Cryst. Solids.* – 1994. – V. 169. – P. 15 – 28.
77. Cannas M. Time resolved photoluminescence associated with non-bridging oxygen hole centers in irradiated silica / M. Cannas, V. Lavinia, B. Roberto // *Nucl. Instr. Meth. Phys. Res. B.* – 2008. – V. 266. – P. 2945 – 2948.
78. Skuja L. N. Isoelectronic series of twofold coordinated Si, Ge, and Sn atoms in glassy SiO_2 : a luminescence study / L. N. Skuja // *J. Non- Cryst. Solids.* – 1992. – V. 149. – P. 77 – 95.
79. Nishikawa H. Decay kinetics of the 4.4-eV photoluminescence associated with the two states of oxygen-deficient-type defect in amorphous SiO_2 / H. Nishikawa, E. Watanabe, D. Ito, Y. Ohki // *Phys. Rev. Lett.* – 1994. – V. 72. – P. 2101 – 2104.

80. Skuja L. Defects in oxide glasses / L. Skuja, M. Hirano, H. Hosono, K. Kajihara // *Phys. Stat. Sol. (c)*. – 2005. – V. 2. – P.15 – 24.
81. Li B. Impact of heat treatment on NBOHC luminescence of OH-containing and H₂-impregnated fused silica for deep-ultraviolet application // B. Li, J. Zhou, Y. Han, Q. Wang, H. Liu // *Journal of Luminescence*. – 2019. – V. 209. – P. 31 – 38
82. Cannas M. Vacuum ultraviolet excitation of the 1.9-eV emission band related to nonbridging oxygen hole centers in silica / M. Cannas, F.M. Gelardi // *Phys. Rev. B*. – 2004. – V. 69. – № 153201.
83. Skuja L. Oxygen-Related Intrinsic Defects in Glassy SiO₂: Interstitial Ozone Molecules / L. Skuja, M. Hirano, H. Hosono // *Phys. Rev. Lett.* – 2000. – V. 84. – P. 302 – 305.
84. Winkler B. Correlations between Structural and Optical Properties of Peroxy Bridges from First Principles / B. Winkler, L. Martin-Samos, N. Richard, L. Giacomazzi, A. Alessi, S. Girard, A. Boukenter, Y. Ouerdane, M. Valant // *J. Phys. Chem. C*. – 2017. – V. 121. – P. 4002 – 4010.
85. Paleari A. Competition between green self-trapped-exciton and red non-bridging-oxygen emissions in SiO₂ under interband excitation / A. Paleari, F. Meinardi, S. Brovelli, R. Lorenzi // *Communications Physics*. – 2018. – V. 1. – P. 67 – 79.
86. Cannas M. Spectroscopic parameters related to non-bridging oxygen hole centers in amorphous-SiO₂ / M. Cannas, L. Vaccaro, B. Boizot // *J. Non-Cryst. Solids*. – 2006. – V. 352. – P. 203 – 208.
87. Michele V. D. Photoluminescence of Point Defects in Silicon Dioxide by Femto-second Laser Exposure / V. D. Michele, E. Marin, A. Boukenter, M Cannas, S. Girard, Y. Ouerdane // *Phys. Status Solidi A*. – 2021. – V. 218. – № 2000802
88. Radtsig V. A. Point Defects on the Silica Surface: Structure and Reactivity / V. A. Radtsig // *Thin Films and Nanostructures* – 2007. – V. 34. – P. 231 – 345.
89. Messina F. Generation and excitation of point defects in silica by synchrotron radiation above the absorption edge / F. Messina, L. Vaccaro, M. Cannas // *Phys. Rev. B*. – 2010. – V. 81. – № 035212.

90. Messina F. Photochemical generation of E' centres from Si-H in amorphous SiO₂ under pulsed ultraviolet laser radiation / F. Messina, M. Cannas // *J. Phys.: Condens. Matter.* – 2006. – V. 18. – P. 9967 – 9973.
91. Griscom D.L. Optical Properties and Structure of Defects in Silica Glass / D.L. Griscom // *J. Ceram. Soc. Jpn.* – 1991. – V. 99. – P. 923 – 942.
92. Skuja L. Luminescence of non-bridging oxygen hole centers as a marker of particle irradiation of α -quartz / L. Skuja, N. Ollier, K. Kajihara // *Radiation Measurements.* – 2020. – V. 135. – № 106373.
93. Kajihara K. Diffusion and reactions of interstitial oxygen species in amorphous SiO₂: A review / K. Kajihara, T. Miura, H. Kamioka, Ak Aiba, A., M. Uramoto, Yu. Morimoto, M. Hirano, L. Skuja, H. Hosono // *J. Non-Cryst. Solids.* – 2008. – V. 354. – P. 224 – 232.
94. Skuja L. Direct singlet-to-triplet optical absorption and luminescence excitation band of the twofold-coordinated silicon center in oxygen-deficient glassy SiO₂ / L. Skuja // *J. Non-Cryst. Solids.* – 1994. – V. 167. – P. 229 – 238.
95. Zhang, Yiming "Corrected Values for Boiling Points and Enthalpies of Vaporization of Elements in Handbooks". *Journal of Chemical and Engineering Data.* – 2011. – 56P.
96. Xia Chao. Effects of rhenium on graphene grown on SiC (0001) / Chao Xia, Alexey A. Tal, Leif I. Johansson, Weine Olovsson, Igor A. Abrikosov, Chariya Jacobi // *Journal of Electron Spectroscopy and Related Phenomena.* – 2018. – V. 222. – P. 117 – 121.
97. Liu L. G Effect of pressure and temperature on lattice parameters of rhenium / L. G. Liu, T. Takahashi, W. A. Bassett // *Journal of Physics and Chemistry of Solids.* – 1970. – V. 31. – P. 1345 – 1351.
98. Naumov A. V. Rhythms of rhenium / A. V. Naumov // *Russian Journal of Non-Ferrous Metals.* – 2007. – V. 48. – P. 418 – 423.

99. Ryashentseva, Margarita A. (1998). "Rhenium-containing catalysts in reactions of organic compounds / Margarita A. Ryashentseva // *Russian Chemical Reviews*. – 1998. – V. 67. – P. 157 – 177.
100. Mol Johannes C. Olefin metathesis over supported rhenium oxide catalysts / *Catalysis Today*. – 1999. – V. 51. – P. 289 – 299.
101. Angelidis T. N. Selective Rhenium Recovery from Spent Reforming Catalysts / T. N. Angelidis, D. Rosopoulou, V. Tzitzios // *Ind. Eng. Chem. Res.* – 1999. – V. 38. – P. 1830 – 1836.
102. Stefanov B.B. Cluster models for the photoabsorption of divalent defects in silicate glasses: Basis set and cluster size dependence / B.B. Stefanov and K. Raghavachari //, *Appl. Phys. Lett.* – 1997. – V. 71. – P. 770 – 772.
103. Rebane K.K. *Impurity Spectra of Solids* / K.K. Rebane – Springer: New York. – 1970. – P. 155 – 171.
104. Weissbluth, M. *Atoms and Molecules* / M. Weissbluth – Elsevier: New York, 1978. – 251 p.
105. Bransden B.H. *Physics of atoms and molecules* / B.H. Bransden, C.J. Joachain, John Wiley: New York. – 1983. – 61 p.
106. Jaffé H.H. *Theory and applications of UV spectroscopy* / H.H. Jaffé and M. Orchin. – Wiley and Sons, New York. – 1970 – 624 p.
107. Harris D.C. *Symmetry and Spectroscopy* / D.C. Harris and M.D. Bertolucci // *J. Chem. Educ.* – 1980. V. 57. – № A60.
108. Huang B.K. Theory of Light Absorption and Non-Radiative Transitions in F-Centres / B.K. Huang and A. Rhys // *Proc. R. Soc. Ser. A.* – 1950. V. 204. – P. 406 – 423.
109. Cupane A. Low temperature optical absorption spectroscopy: an approach to the study of stereodynamic properties of heme proteins / A. Cupane, M. Leone, E. Vitrano, L. Cordone // *J. Eur. Biophys.* – 1995. V. 23. – P. 385 – 398.
110. Markham J. J. Interaction of Normal Modes with Electron Traps / J. J. Markham // *Rev. Mod. Phys.* – 1959. V. 31. – P. 956 – 989.

111. Bagratashvili V. N. Inhomogeneous nature of UV absorption bands of bulk and surface oxygen-deficient centers in silica glasses / V.N. Bagratashvili, S.I. Tsykina, V.A. Radtsig, A.O. Rybaltovskii, P.V. Chernov, S.S. Alimpiev, Y.O. Simanovskii // *J. Non-Cryst. Solids.* – 1995. V. 180. – P. 221 – 229.
112. Leone M. Low temperature photoluminescence spectroscopy relationship between 3.1 and 4.2 eV bands in vitreous silica / M. Leone, R. Boscaino, M. Cannas, F.M. Gelardi // *J. Non-Cryst. Solids.* – 1997. V. 216.– P. 105 – 110.
113. Chiodini N. Photoluminescence of Sn-doped SiO₂ excited by synchrotron radiation / N. Chiodini, F. Meinardi, F. Morazzotti, A. Paleari, R. Scotti, D. Di Martino // *J. Non Cryst. Solids.* – 2000. V. 261.– P. 1 – 8.
114. Rybaltovskii A. O. Spectroscopic Features of Silica Glasses Doped with Tin / A.O. Rybaltovskii, I.A. Kamenskikh, V.V. Mikhailin, N.L. Semenova, D.A. Spasskii, G. Zimmerer, P.V. Chernov, K.M. Golant // *Glass Phys. Chem.* – 2002. V. 22. – P. 379 – 388.
115. Sukumar Basu, *Crystalline Silicon – Properties and Uses*, chp 8 Defect Related Luminescence in Silicon Dioxide Network: A Review by Roushdey Salh 2011. – P. 135 – 172.
116. Fossum E.R. A Review of the Pinned Photodiode for CCD and CMOS Image Sensors / E.R. Fossum, D. B. Hondongwa // *IEEE J. Electron Devices Soc.*– 2014.– V. 2. – P. 33 – 43.
117. Teranishi N. Effect and Limitation of Pinned Photodiode / N. Teranishi // *IEEE Trans. Electron Devices.* – 2016.– V. 63. – P.10 – 15.
118. Teranishi N. Analysis of Subthreshold Current Reset Noise in Image Sensors / N. Teranishi // *Sensors.* – 2016. –V. 16. – P. 663 – 680.
119. Wang X. Y. A CMOS Image Sensor with a Buried– Channel Source Follower / X.– Y. Wang, M.F. Snoeij, P.R. Rao, A. Mierop, A. J. P. Theuwissen // *In Proceedings of the 2008 IEEE International Solid– State Circuits Conference –Digest of Technical Papers, San Francisco, CA, USA.* – 2008. – P. 62 – 63.

120. Hoshino Y. A novel mechanism of ultrathin SOI synthesis by extremely low-energy hot O^+ implantation / Y. Hoshino, G. Yachida, K. Inoue, T. Toyohara, J. Nakata // *J. Phys. D: Appl. Phys.* – 2016. – V. 49. – № 315106.
121. Hara T. Delaminations of Thin Layers by High Dose Hydrogen Ion Implantation in Silicon / T. Hara, K. Kajiyama, T. Yoneda, M. Inoue // *J. Electrochem. Soc.* – 1996. – V.143. – P.166–168.
122. Kurita K. Proximity Gettering Design of Hydrocarbon–Molecular–Ion–Implanted Silicon Wafers Using Dark Current Spectroscopy for CMOS Image Sensors / K. Kurita, T. Kadono, S. Shigematsu, R. Hirose, R. Okuyama, A. Onaka-Masada, H. Okuda, Y. Koga // *Sensors.* – 2019. – V. 9. – № 2073
123. Impellizzeri G. Fluorine in preamorphized Si: Point defect engineering and control of dopant / G. Impellizzeri, S. Mirabella, F. Priolo // *J. Appl. Phys.* – 2006. – V. 99. – № 103510.
124. Klinger D. Nanostructure of Si-Ge Near-Surface Layers Produced by Ion Implantation and Laser Annealing / D. Klinger, S. Kret, J. Auleytner, D. `ymierska // *Acta Physica Polonica A.* – 2002. – V. 102. – P. 259 – 264.
125. Litta E. D. CMOS integration of high-k/metal gate transistors in diffusion and gate replacement (D&GR) scheme for dynamic random-access memory peripheral circuits / E. D. Litta, R. Ritzenthaler, T. Schraml, A. Spessot, B. Sullivan, V. Machkaoutsan, P. Fazan, Y. Ji, G. Mannaert, Ch. Lorant, F. Sebaai, A. Thiam, M. Ercken, S. Demuynck, N. Horiguchi // *Jpn. J. Appl. Phys.* – 2018. – V.57. – № 04FB08.
126. Zatsepin D. A. Sn-loss effect in a Sn-implanted a-SiO₂ host-matrix after thermal annealing: A combined XPS, PL, and DFT study / D.A. Zatsepin, A.F. Zatsepin, D.W. Boukhvalov, E.Z. Kurmaev, N.V. Gavrilov // *Applied Surface Science.* – 2016. – V. 367. – P. 320 – 326.
127. Zatsepin A. F. Defects and localized states in silica layers implanted with lead ions / A.F. Zatsepin, H.-J. Fitting, E.A. Buntov, V.A. Pustovarov, B. Schmidt // *Journal of Luminescence.* – 2014. – V.154 – P. 425 – 429.

128. Green R. J. Electronic band gap reduction and intense luminescence in Co and Mn ion-implanted SiO₂ / R. J. Green, D. A. Zatsepin, D. J. St. Onge, E. Z. Kurmaev, N. V. Gavrilov, A. F. Zatsepin, A. Moewes // *J. Appl. Phys.* – 2014. – V. 115. – № 103708.
129. Buntov E. A. Electronic and vibrational states of oxygen and sulfur molecular ions inside implanted SiO₂ films / E.A. Buntov, A.F. Zatsepin, V.S. Kortov, V.A. Pustovarov, H.-J. Fitting // *J. Non-Cryst. Solids.* – 2011. – V. 357. – P. 1977 – 1980.
130. Zatsepin D. A. Effect of long-term storage on the electronic structure of semiconducting silicon wafers implanted by rhenium ions / D. A. Zatsepin, D. W. Boukhvalov, A. F. Zatsepin, A. N. Mikhaylov, N. N. Gerasimenko, O. A. Zaporozhan // *J Mater. Sci.* – 2021. – V.56. – P. 2103 – 2112.
131. Abragam A. Electron paramagnetic resonance of transition ions / A. Abragam and B. Bleaney. – Clarendon, Oxford. – 2012. – 911 p.
132. Weil J. A. Electron Paramagnetic Resonance. Elementary Theory and Practical Applications / J.A. Weil, J.R. Bolton and J.E. Wertz. – Wiley, New York. – 1994. – 568 pp.
133. Gavrilov N.V. High-current pulse sources of broad beams of gas and metal ions for surface treatment / N.V. Gavrilov, E.M. Oks // *Nucl. Instrum. Meth. Phys. Res. A.* – 2000. – V. 439. – P. 33 – 44.
134. Ziegler James F. SRIM The Stopping and Range of Ions in Matter/ James F. Ziegler, Jochen P. Biersack, Matthias D. Ziegler // Ion Implantation Press, 2013. Electronic manual, available at <http://www.srim.org> .
135. Buntov E. Point defects and interference effects in electron emission of Si/SiO₂: Li, Na, K structures /E. Buntov, A. F. Zatsepin, A. Slesarev A. Mikhailovich, A. Mikhaylov // *Phys. Status Solidi (a)* – 2015. – V. 212. – P. 2672 – 2676.

136. Zatsepin D.F. Quality assessment of GaN epitaxial films: Acidification scenarios based on XPS-and-DFT combined study / D. A. Zatsepin, D. W. Boukhvalov, A. F. Zatsepin // *Applied Surface Science*. – 2021. – V. 563. – № 150308.
137. Zatsepin A. F. Ionization effects in Si/SiO₂: Li, Na, K implanted structures under the impact of high-energy α particles / A.F. Zatsepin, E. A. Buntov, A.I. Slesarev, D.Y. Biryukov // *J. Surf. Investig. C* – 2016. – V. 10. – P. 603 – 607.
138. Messina F. Generation and excitation of point defects in silica by synchrotron radiation above the absorption edge // F. Messina, L. Vaccaro, M. Cannas // *Phys. Rev. B* – 2010. – V. 81. – №. 035212.
139. Leon M. Neutron Irradiation Effects on the Structural Properties of KU1, KS-4V and I301 Silica Glasses / M. Leon, L. Giacomazzi, S. Girard, N. Richard, P. Martín, L. Martín-Samos, A. Ibarra, A. Boukenter, Y. Ouerdane // *IEEE Trans. Nucl. Sci.* – 2014. – V. 61. – P. 1522 – 1530.
140. Schmidt B. Ion Beams in Materials Processing and Analysis / B. Schmidt, K. Wetzig // Ch. 4. Materials processing, Springer-Verlag, Wien. –2013.– P. 117–251.
141. Skuja L.N. A new intrinsic defect in amorphous SiO₂: Twofold coordinated silicon / L.N. Skuja, A.N. Streletsky, A.B. Pakovich // *Solid State Commun.* – 1984. V. 50. – P. 1069 – 1072.
142. Hosono H. Experimental evidence for the Si-Si bond model of the 7.6-eV band in SiO₂ glass / H. Hosono, Y. Abe, H. Imagawa, H. Imai, K. Arai // *Phys. Rev. B* –1991. – V. 44. – P. 12043 – 12045.
143. Richard N. First principles study of oxygen-deficient centers in pure and Ge-doped silica / N. Richard, S. Girard, L. Martin-Samos, V. Cuny, A. Boukenter, Y. Ouerdane, J. P. Meunier // *J. Non-Cryst. Solids.* – 2011. – V. 357. – P. 1994 – 1999.

144. Zatsëpin A.F. New optical oxygen-deficient centers in 80 keV Re-implanted amorphous silica / A.F. Zatsëpin, Y.A. Kuznetsova, T.V. Shtang, A.N. Mikhaylov, M.S.I. Koubisy // *J. Non-Cryst. Solids.* – 2020. – V. 529 – № 119775.
145. Griscom David L. Trapped-electron centers in pure and doped glassy silica: A review and synttsis /David L. Griscom // *J. Non-Cryst. Solids.* – 2011. – V. 357 – P. 1945 – 1962.
146. Lia W. Highly selective separation of Re (VII) from Mo (VI) by using bio-material-based ionic gel adsorbents: Extractive adsorption enrichment of Re and surface blocking of Mo / W. Lia, X. Dongb, L. Zhub, H. Tang // *Chemical Engineering Journal.* – 2020. – V. 387. – № 124078.
147. Trukhin A.N. Luminescence of localized states in silicon dioxide glass. A short review / A.N. Trukhin // *J. Non-Cryst. Solids.* – 2011. – V. 357. – P. 1931 – 1940.
148. Zatsëpin A. F. Silicon Based Nanomaterials / A. F. Zatsëpin, E. A. Buntov // Chapter 5. Synchrotron-excited photoluminescence spectroscopy of silicon- and carbon-containing quantum dots in low dimensional SiO₂ matrices. Springer: New York. – 2013. – pp. 89 –117.
149. Pan Z. Photoluminescence of Er-doped ZnO nanoparticle films via direct and indirect excitation / Z. Pan, A. Ueda, H. Xu, SK. Hark, SH. Morgan, Mu. R // *Journal of Nanophotonics.* – 2012. – V. 6. – № 063508.
150. Savchenko S. S. Temperature-induced shift of the exciton absorption band in InP/ZnS quantum dots / S. S. Savchenko, A. S. Vokhmintsev, I. A. Weinstein // *Opt. Mater. Express.* – 2017. – V. 7. – P. 354 – 359.
151. Reznitsky A. N. Temperature dependence of photoluminescence intensity of self-assembled CdTe quantum dots in the ZnTe matrix under different excitation conditions / A. N. Reznitsky, A. A. Klochikhin, S. A. Permogorov// *Physics of the Solid State.* – 2012.– V. 54.– P. 123 – 133.

152. Wang J. Thermal activation energy of crystal and amorphous nano-silicon in SiO₂ matrix / J. Wang, M. Righini, A. Gnoli, S. Foss, T. Finstad, U. Serincan, R. Turan // *Solid State Communications*. – 2008.– V. 147.– P. 461 – 464.
153. Zatsepin A. F. The temperature behavior and mechanism of exciton luminescence in quantum dots / A. F. Zatsepin, D.Y. Biryukov // *Physical Chemistry Chemical Physics*. – 2017.– V. 19.– P. 18721 – 18730.
154. Zatsepin A. F. Temperature Dependence of Photoluminescence of Semiconductor Quantum Dots upon Indirect Excitation in a SiO₂ Dielectric Matrix / A. F. Zatsepin, D. Yu. Biryukov // *Physics of the Solid State*. – 2015. – V. 57. – P. 1601 – 1606.
155. Biryukov D. Yu. Analytical Temperature Dependence of the Photoluminescence of Semiconductor Quantum Dots / D. Yu. Biryukov and A. F. Zatsepin // *Physics of the Solid State*. – 2014. – V. 56. – P. 635 – 638.
156. Tauc J. Optical Properties and Electronic Structure of Amorphous Germanium / J. Tauc, H. Grigorovici, A. Vancu // *Phys. Status Solidi (b)*. – 1966.– V. 15.– P. 627 – 637.
157. Zakaly H. M. H. Synthesis, optical, structural and physical properties of newly developed dolomite reinforced borate glasses for nuclear radiation shielding utilizations: An experimental and simulation study / Hesham M. H. Zakaly, M. Rashad, H.O. Tekin, H.A. Saudi, Shams A. M. Issa, A.M. A. Henaishah // *Optical Materials*. – 2021.– V. 114.– № 110942.
158. Anuar M. F. Sustainable Production of Arecanut Husk Ash as Potential Silica Replacement for Synthesis of Silicate-Based Glass-Ceramics Materials / M. F. Anuar, Y.W. Fen, M. Z. Azizan, F. Rahmat, M. H. M. Zaid, R. E. M. Khaidir, N. A. S. Omar // *Materials*. – 2021. – V. 14. – № 1141.
159. Vainshtein I. A the Urbach Rule for the PbO-SiO₂ Glasses / I. A Vainshtein, A. F. Zatsepin, V. S. Kortov, Yu. V. Schapova // *Physics of the Solid State*. – 2000.– V. 42.– P. 230 – 2375.

160. Zatsepin A. F. UV Absorption and Effects of Local Atomic Disordering in the Nickel Oxide Nanoparticles / A. F. Zatsepin, Yu. A. Kuznetsova, V. I. Sokolov // *Journal of Luminescence*. – 2017. – V. 183. – P. 135 – 142.
161. Dunstan, D. J. Band-gap fluctuations in amorphous semiconductors / D. J. Dunstan // *Solid State Commun.* – 1982. – V. 43. – P. 341 – 344.
162. Zatssepin A.F. New optical oxygen-deficient centers in 80 keV Re-implanted amorphous silica / A.F. Zatssepin, Y.A. Kuznetsova, T.V. Shtang, A.N. Mikhaylov, M.S.I. Koubisy // *J. Non-Cryst. Solids*. – 2020. – V. 529. – № 119775.
163. Dexter D. L. Absorption of Light by Atoms in Solids / D. L. Dexter // *Phys. Rev.* – 1956. – V. 101. – P. 48 – 55.
164. Kitamura R. Optical constants of silica glass from extreme ultraviolet to far infrared at near room temperature / R. Kitamura, L. Pilon, M. Jonasz // *Appl. Opt.* – 2007. – V. 46. – P. 8118 – 8133.
165. Andrie A. The anisotropy in the optical constants of quartz crystals for soft X-rays / A. Andrie, P. Hönicke, J. Vinson, R. Quintanilha, Q. Saadeh, S. Heidenreich, F. Scholze, V. Soltwisch // *J. Appl. Cryst.* – 2021. – V. 54. – P. 402 – 408.
166. Ollier N. Relaxation study of pre-densified silica glasses under 2.5 MeV electron irradiation / N. Ollier, M. Lancry, C. Martinet, V. Martinez, S. Le Floch, D. Neuville // *Sci. Rep.* – 2019. – V. 9. – № 1227.
167. Zatssepin A.F. Statics and dynamics of excited states of oxygen-deficient centers in SiO₂ / A.F. Zatssepin // *Physics of the Solid State*. – 2010. – V. 52. – P. 1176 – 1187.
168. Yue Y. Hydroxyl E' center and stress-assisted proton generation in hydrogen-rich amorphous silica / Y. Yue, B. Zhou, F. Zhang, P. Li, Y. Song, X. Zuo // *Computational Materials Science*. – 2020. – V. 182. – № 1097602.
169. Zatssepin A.F. Formation of Ge and GeO_x nanoclusters in Ge⁺ implanted SiO₂/Si thin-film hetero structures under rapid thermal annealing / A.F. Zatssepin,

- D.A. Zatsepin, I.S. Zhidkov, E.Z. Kurmaev, H. J. Fitting, B. Schmidt, A.P. Mikhailovich, K. Lawniczak-Jablonska // *Applied Surface Science*. – 2015. – V. 349. – P. 780 – 784.
170. Lopes J. M. J. Correlation between structural evolution and photoluminescence of Sn nanoclusters in SiO₂ layers / J.M.J. Lopes, F. Kremer, P.F.P. Fichtner, F.C. Zawislak // *Nucl. Instrum. Methods*. – 2006. – V. 242. – P. 157 – 160.
171. Zatsepin A. F. Photoluminescence of implantation-induced defects in SiO₂:Pb⁺ glasses / A.F. Zatsepin, E.A. Buntov, V.S. Kortov, V.A. Pustovarov, N.V. Gavrilov // *J. Surf. Investig.* – 2014. – V. 8. – P. 540 – 544.
172. Trukhin A.N. Photoelectric response of localized states in silica glass / A.N. Trukhin // *J. Non-Cryst. Solids*. – 2019. – V. 511 – P. 161 – 165.
173. Kohketsu M. Photoluminescence centers in VAD SiO₂ glasses sintered under reducing or oxidizing atmospheres / M. Kohketsu, K. Awazu, H. Kawazoe, M. Yamane // *Jpn. J. Appl. Phys.* – 1989. – V. 28. – P. 615 – 621.
174. Kuzuu N. Excimer-laser-induced emission bands in fused Silica / N. Kuzuu, M. Murahara // *Phys. Rev. B*. – 1993. – V. 47. – P. 3083 – 3088.
175. Nishikawa H. Photoluminescence from defect centers in high-purity silica glasses observed under 7.9-eV excitation / H. Nishikawa, T. Shiroyama, R. Nakamura, Y. Ohki // *Phys. Rev. B*. – 1992. – V. 45. – P. 586 – 591.
176. Alessi A. Formation of optically active oxygen deficient centers in Ge-doped SiO₂ by γ - and β -ray irradiation / A. Alessi, S. Agnello, D.G. Sporea, C. Oproiu, B. Brichard, F.M. Gelardi // *J. Non-Cryst. Solids*. – 2010. – V. 356. – P. 275 – 280.
177. Sivaramaiah G. Electron paramagnetic resonance study of Silica grains: Implications on uranium and thorium mineralization / G. Sivaramaiah // *Optik*. – 2019. – V. 182. – P. 124 – 130.
178. Mashkovtsev R. I. EPR study of new E' centers in neutron-irradiated α -Silica / R. I. Mashkovtsev, Y. Pan // *Europhysics Letters*. – 2018. – V. 124. – № 54001.

179. Mashkovtsev R. I. EPR study of the E' defects in optical glasses and cristobalite / R. I. Mashkovtsev, A. I. Nepomnyashchikh, A. P. Zhaboedov, A. S. Paklin // *Europhysics Letters*. – 2021. – V. 133. – № 14003.
180. Yip K. L. Electronic structure of E' centers in SiO₂ / K.L. Yip, W.B. Fowler *Phys. Rev. B*. – 1975. – V. 11. – P. 2327 – 2338.
181. Alessi A. Properties and generation by irradiation of germanium point defects in Ge-Doped silica, in: R. Germano (Ed.), *Germanium: Properties, Production and Applications* / A. Alessi, S. Agnello, F.M. Gelardi. – Nova Science Publishers, 2012.
182. Trukhin A. Photosensitivity of silica glass with germanium studied by photoinduced of thermally stimulated luminescence with vacuum ultraviolet radiation / A. Trukhin, B. Poumellec // *J. Non-Cryst. Solids*. – 2003. – V. 324. – P. 21 – 28.
183. Wang J. Photoluminescence of Silica Made by Sol-gel Method / J. Wang, Xiuting Wang, Yu Guo, Yang Wang, Zeya Zhu // *IOP Conf. Ser.: Earth Environ. Sci.* – 2020. – V. 440. – № 22018.
184. Zatsepin A. F. Local atomic configurations, energy structure, and optical properties of implantation defects in Gd-doped silica glass: an XPS, PL, and DFT study / A.F. Zatsepin, D.A. Zatsepin, D.W. Boukhvalov, Y. Kuznetsova, V. Ya. Shur, A. Esin, N.V. Gavrilov // *J. Alloy. Compd.* – 2019. – V. 796. – P.77–85.
185. Zatsepin A. F. Specific features of photoluminescence of oxygen-deficient centers in irradiated silica glass / A. F. Zatsepin, V.S. Kortov, D. Yu. Biryukov, I.A. Weinstein // *Journal of Luminescence*. – 2007. – V. 122. – P. 152 – 154.
186. Trukhin A.N. Luminescence of localized states in oxidized and fluorinated silica glass / A.N. Trukhin // *J. Non-Cryst. Solids*. – 2019. – V. 521. – № 119525.
187. Agnello S. Competitive relaxation processes of oxygen deficient centers in silica / S. Agnello, R. Boscaino, M. Cannas, F. M. Gelardi, M. Leone, B. Boizot // *Phys. Rev. B*. – 2003. – V. 67. – № 033202.

188. Zatsepin A. Electronic Structure and Optical Absorption in Gd-Implanted Silica Glasses / A. Zatsepin, Y. Kuznetsova, D. Zatsepin, D. Boukhvalov, N. Gavrilov, M.S. I. Koubisy // *Physica Status Solidi (a) Applications and Materials Science*. – 2019. – V. 216. – № 1800522.
189. M.S. I. Koubisy Ion-beam induced quasi-dynamic continual disorder in Bi-implanted Horgan silica glass/ M.S. I. Koubisy, A.F. Zatsepin, D.Y. Biryukov, N.V. Gavrilov, D. A. Zatsepin, Shtang, T.V// *J. Non-Cryst. Solids*. – 2021. – V. 563. – № 120818.
190. Sulimov V. B. Photoinduced structural transformations in silica glass: the role of oxygen vacancies in the mechanism of formation of refractive-index gratings by UV irradiation of optical fibres / V B Sulimov, V O Sokolov, E M Dianov, B Pommellec // *Quantum Electronics*. – 1996. – V. 26. – P. 988 – 993.
191. Sun Sh. Optical absorption of Bi²⁺-ODC(II) active center in Bi-doped silica opticalfiber / Shihao Sun, Baonan Jia, Binbin Yan, Shanjun Li, Cong Gao, Jianjun Wang, Bin Yang, Pengfei Lu // *Journal of Luminescence*. – 2019. – V. 213. – P. 304 – 309.
192. Zatsepin A. F. Luminescence of modified centers of a nonbridging oxygen atom in alkali silicate and Silica glasses / A. F. Zatsepin, V. B. Guseva, A.F. Zatsepin // *Glass Physics and Chemistry*. – 2008. – V.34. – P. 934 – 941.
193. Vaccaro L. Photoluminescence of Si Nanocrystals Embedded in SiO₂ / L. Vaccaro, L. Spallino, A.F. Zatsepin, E.A. Buntov, A. Ershov, D.A. Grachev, M. Kannas, *Phys. Status Solidi (b)*. – 2015. – V. 252. – P. 600 – 606.